

Development and Application of Thermal
Desorption-Gas Chromatography-Orbitrap-
Mass Spectrometry for the Identification and
Determination of Organic Trace Substances in
Atmospheric Environmental Research and
Chemical Ecology

DISSERTATION

for attaining the Academic Degree of
'Doctor rerum naturalium' (Dr. rer. nat.)
in the doctoral subject Chemistry

at the Department of Chemistry
of the Johannes Gutenberg University, Mainz

submitted by

Daniela Kleinsimlinghaus

born in Mainz

JOHANNES GUTENBERG
UNIVERSITÄT MAINZ



Mainz, March 2024

Dean:

1st supervisor:

2nd supervisor:

Date of oral Examination: 17.05.2024

D77 - Dissertation of the Johannes Gutenberg University, Mainz

I hereby declare that I wrote the dissertation submitted without any unauthorized external assistance and used only sources acknowledged in the work. All textual passages which are appropriated verbatim or para-phrased from published and unpublished texts as well as all information obtained from oral sources are duly indicated and listed in accordance with bibliographical rules. In carrying out this research, I complied with the rules of standard scientific practice as formulated in the statutes of Johannes Gutenberg-University Mainz to insure standard scientific practice.

Mainz, March 2024

*"Happiness can be found, even in the darkest of times,
if one only remembers to turn on the light."*

Albus Dumbledore

Zusammenfassung

Das Verständnis der Chemie und des Verhaltens von Molekülen in Nanometer-Aerosolpartikeln, die in Laborexperimenten beobachtet wurden, kann helfen, die Eigenschaften von Nanometer-Aerosolpartikeln in der Atmosphäre und mögliche laufende Reaktionen vorherzusagen. Die Diels-Alder-Reaktion, eine gut untersuchte Reaktion in der organischen Chemie, wird hier als Modellsystem verwendet. Von dieser Reaktion ist bekannt, dass höherer Druck bindungsbildende Reaktionen fördert. Dies bietet die Möglichkeit, ein druckempfindliches chemisches Systemverhalten in nanometergroßen Aerosolpartikeln zu untersuchen. Das Dienophil und die Diene wurden für die Reaktion aufgrund ihrer Reaktivität, Flüchtigkeit und Nachweisbarkeit in der Aerosol- bzw. Gasphase ausgewählt. Die Beobachtung des Partikelwachstums war ein Indikator dafür, ob eine Reaktion stattgefunden hatte. Die Wachstumsfaktoren von monodispersen Aerosolpartikeln mit Durchmessern von 30, 60 und 90 nm wurden für zwei Reaktionssysteme bestimmt. Die experimentelle Bestimmung der Reaktionsgeschwindigkeit und der Reaktionsgeschwindigkeitskonstanten wurde durchgeführt, um den Einfluss des Drucks in Verbindung mit der Partikelgröße auf die Reaktionsgeschwindigkeit und die Reaktionsgeschwindigkeitskonstanten zu untersuchen und mit Literaturwerten zu vergleichen. Die Analyse erfolgte mittels Scanning Mobility Particle Sizer Systems (SMPS) und die Charakterisierung der Reaktionsprodukte mittels thermischer Desorption gekoppelt mit einem Gaschromatograph-Massenspektrometer-System (TD-GC-MS).

Die Kombination von (TD) und (GC), gekoppelt mit Massenspektrometrie (MS), bietet die Möglichkeit, eine Vielzahl verschiedener Analyten zu analysieren, insbesondere flüchtige organische Verbindungen (VOC). Das TD-Verfahren selbst wird als Injektionsverfahren eingestuft, bei dem der Analyt aus einem Adsorptionsrohr in den GC übertragen wird. Der TD-Injektor, der mit einem GC-MS-System gekoppelt ist, funktioniert nach einem einfachen Prinzip: Die auf einem Adsorptionsrohr gesammelten Analyten werden über einen längeren Zeitraum thermisch desorbiert und während der Desorption in einem Fokussierungsvolumen konzentriert. Dieses Fokussierungsvolumen, bei dem es sich um eine gekühlte Kapillare oder eine Adsorptionsfalle handeln kann, wird dann schnell aufgeheizt, um eine schmale Injektion von Analyten für die anschließende Chromatographie bereitzustellen. Kommerziell erhältliche TD-Systeme haben ein breites Anwendungsspektrum. Allerdings eigneten sich in der Vergangenheit diese Systeme nicht für die Analyse von sehr schwerflüchtigen Analyten und thermisch empfindlichen organischen Verbindungen. Um diese Einschränkungen zu überwinden, wurde von früheren Doktoranden in-house entwickelter TD-Injektor konzipiert. In dieser Arbeit wurde er an einigen Stellen weiterentwickelt und dann aus den gesammelten Erfahrungen ein neuer und vielseitiger TD-Injektor entwickelt und gebaut. Dieser wurde mit hochauflösender

Massenspektrometrie gekoppelt. Der TD Injektor bietet mehrere Vorteile, zum Beispiel den kürzest möglichen Injektionsweg für Analyten ohne Zwischenfokussierung auf Adsorbentien und ohne Verwendung von Ventilen oder Ventilkreisläufen. Außerdem können der TD-Injektor und das Verfahren leicht gewartet und modifiziert werden, um optimale Ergebnisse für die untersuchten Analyten zu erzielen. Wir haben die Funktionalität des entwickelten Systems getestet, indem wir einen halbflüchtigen organischen Analyten untersucht haben, der durch Reaktionen organischer Moleküle in nanometergroßen Aerosolen mittels heterogener Chemie gebildet wird.

Motiviert durch das Ziel des Einsatzes in der Spurenanalytik wurde TD-Injektor für Untersuchungen auf dem Gebiet der chemischen Ecology verwendet. Die Ungewissheit hinsichtlich der Kommunikation zwischen sozialen Insekten über die flüchtige Gasphase wurde eine nicht-invasive Methode entwickelt, um erste Erkenntnisse über diese Prozesse zwei verschiedener Ameisenarten zu gewinnen. Die Laborexperimente wurden unter atmosphärischen Bedingungen mit synthetischer Luft durchgeführt. Eine speziell entwickelte Glasvorrichtung wurde gebaut, um Matrixeffekte bei der Probenahme aus der Gasphase in Adsorptionsröhren zu vermeiden. Die Adsorptionsröhren wurden durch thermische Desorption in Verbindung mit einem hochauflösenden GC-Orbitrap-MS gemessen, was die Bestimmung von Summenformeln ermöglicht. Die Ameisen und ihre Brut wurden getrennt untersucht, um die emittierten Gasphasen zu vergleichen. Es wurde untersucht, ob es Unterschiede zwischen den Arten und zwischen den Emissionen von Ameisen und Brut gibt. Es wurde herausgefunden, dass Ameisen und Brut beider Arten eine Gasphase emittieren. Insbesondere die Substanzklasse der Perhydropyrene erscheint vielversprechend, um die Kommunikation zwischen Ameisen und ihrer Brut besser zu verstehen.

Abstract

Understanding the chemistry and behavior of molecules in nanometer aerosol particles observed in laboratory experiments can help predict the properties of nanometer aerosol particles in the atmosphere and possible ongoing reactions. The Diels-Alder reaction, a well-studied reaction in organic chemistry, is used here as a model system. It is known from this reaction that higher pressure promotes bond-forming reactions. This offers the possibility to study a pressure-sensitive chemical system behavior in nanometer-sized aerosol particles. The dienophile and dienes were selected for the reaction due to their reactivity, volatility and detectability in the aerosol and gas phase, respectively. The observation of particle growth was an indicator of whether a reaction had taken place. The growth factors of monodisperse aerosol particles with diameters of 30, 60 and 90 nm were determined for two reaction systems. Experimental determination of the reaction rate and reaction rate constants was performed to investigate the influence of pressure in combination with particle size on the reaction rate and reaction rate constants and to compare with literature values. The analysis was carried out using Scanning Mobility Particle Sizer Systems (SMPS) and the characterization of the reaction products by thermal desorption coupled with a gas chromatograph-mass spectrometer system (TD-GC-MS).

The combination of (TD) and (GC), coupled with mass spectrometry (MS), offers the possibility to analyze a variety of different analytes, especially volatile organic compounds (VOC). The TD method itself is classified as an injection method, where the analyte is transferred from an adsorption tube into the GC. The TD injector, which is coupled to a GC-MS system, works according to a simple principle: the analytes collected on an adsorption tube are thermally desorbed over a longer period of time and concentrated in a focusing volume during desorption. This focusing volume, which can be a cooled capillary or an adsorption trap, is then rapidly heated to provide a narrow injection of analytes for subsequent chromatography. Commercially available TD systems have a wide range of applications. However, in the past, these systems were not suitable for the analysis of very low volatile analytes and thermally sensitive organic compound. To overcome these limitations, former group members developed an in-house TD injector which has been further improved for this study. Based on the experience gained, a new and versatile TD injector was developed and built. Furthermore, it was coupled to high-resolution mass spectrometry. The versatile TD offers several advantages, including the shortest possible injection path for analytes without intermediate focusing on adsorbents and without the use of valves or valve circuits. In addition, the TD injector and process can be easily maintained and modified to achieve optimal results for the analytes under investigation. The functionality of the developed system was tested by investigating a semi-volatile organic analyte formed

through reactions of organic molecules in nanometer-sized aerosols using heterogeneous chemistry.

Motivated by the goal of using the TD-Injector in trace analysis, it has also been used for studies in the field of chemical ecology. A non-invasive method was developed to gain insights into the communication between social insects via the volatile gas phase. This method was used to address the uncertainty surrounding this process in two different ant species. The laboratory experiments were conducted using synthetic air under atmospheric conditions. To avoid matrix effects when sampling from the gas phase into adsorption tubes, a specially designed glass device was used. Thermal desorption was used to measure the adsorption tubes in conjunction with a high-resolution GC-Orbitrap-MS, allowing for the determination of sum formulas. The study investigated potential differences in gas emissions between ant species and between ant and brood emissions. Results showed that both ant species and their brood emit a gas phase. The substance class of perhydropyrenes appears to be particularly promising for gaining a better understanding of ant-brood communication.

Contents

Zusammenfassung	IX
Abstract	XI
1 Introduction	1
1.1 Atmospheric aerosol	4
1.2 New particle formation	5
1.3 Chemical reactions in nanometer aerosol particles and the gas phase	8
1.4 Diels-Alder reactions	9
1.5 Growth factor	11
1.6 Reaction rates	11
1.7 Volatile organic compounds	13
2 Analytical methods and instruments.....	17
2.1 Laboratory flow tube experiments	17
2.2 Glass device for sampling living insects	18
2.3 Sampling and chemical analysis	19
2.3.1 Thermal desorption as an injection technique.....	19
2.3.2 Gas chromatography	26
2.3.3 Mass spectrometry	27
2.4 Techniques for aerosol characterization	32
2.4.1 The measurement of particle concentrations	32
2.4.2 The measurement of aerosol particle size distributions	35
3 Thesis objectives and outline.....	39
4 Chemistry in nanometer aerosol particles: Flow tube experiments with Diels-Alder reactions as model system.....	41
4.1 Introduction	42
4.2 Theory	44
4.2.1 Growth of aerosol particles	44
4.2.2 Diels-Alder reactions.....	44
4.3 Experimental	45
4.3.1 Setup of the reaction system.....	45

4.3.2	Operation of the TD-GC-MS	47
4.3.3	Materials and chemicals.....	48
4.4	Results and discussion	48
4.4.1	Effective pressure inside nanometer-sized particles	49
4.4.2	Detection of the aerosol phase by mass spectrometry	50
4.4.3	Particle growth can be considered an indicator of an ongoing reaction..	50
4.4.4	Substance based theoretical growth rate predictions.....	53
4.4.5	Kinetics of the DA reaction in nanometer aerosol particles	54
4.5	Conclusions.....	57
5	Improvements and new developments on our in-house developed thermal desorption device	59
5.1	Introduction.....	59
5.2	The initial state	59
5.2.1	Hardware.....	60
5.2.2	Software	60
5.3	Implementation	60
5.3.1	Hardware.....	60
5.3.2	Software	63
5.4	Conclusions and outlook	64
6	A versatile thermal desorption system for the identification and quantification of trace organic analytes in the gas and particle phase	67
6.1	Introduction.....	68
6.2	Experimental.....	69
6.2.1	Sampling.....	69
6.2.2	Thermal desorption method	70
6.2.3	GC-Orbitrap-MS.....	70
6.2.4	Chemicals and materials	70
6.3	Results and discussion	71
6.3.1	Construction and process of the developed thermal desorption injector	71
6.3.2	Performance tests and application	75
6.4	Conclusions and outlook	77

7	Novel non-invasive method to investigate volatile trace emissions of ants and their brood with thermal desorption gas chromatography Orbitrap mass spectrometry.....	79
7.1	Introduction	80
7.2	Materials and methods	82
7.2.1	Experimental design	82
7.2.2	Analysis	83
7.3	Results and discussion.....	84
7.4	Conclusions	91
8	Summary and outlook	93
9	Appendix.....	95
9.1	In-house TD - previous state	95
9.2	In-house TD – implementation	97
9.3	Versatile TD	101
9.4	Supplements chapter 8	104
10	List of symbols and abbreviations	108
11	List of tables.....	111
12	List of figures.....	112
13	Bibliography.....	117
14	List of related publications and presentations.....	137
14.1	Oral presentations	137
14.2	Poster presentations	137
	Curriculum Vitae	139

1 Introduction

In recent years, the term 'aerosol' has become widely known due to the coronavirus pandemic. However, aerosol components are diverse (van der Valk & in 't Veen, 2021). Besides their special properties such as affecting the formation of clouds and precipitation (Curtius, 2006) atmospheric aerosols can act and interact like every other molecule in our environment. Research has shown that environmental pollution, specifically suspended particulate matter (PM), which includes aerosol and ultrafine particles classified as nanometer-sized particles, can have an impact on the human health, particularly on lung cells (Hallquist et al., 2009; Jang, Ghio, & Cao, 2006). Atmospheric particulate emissions are correlated with human health effects and epidemiological analyzes have shown that aerosols are drivers of both human morbidity and mortality. However, the health effects of specific components of particulate matter have not yet been well studied. The World Health Organization (WHO) has published a report on the health effects of aerosol particulate matter in 25 European Union countries. The report estimates that emissions and airborne pollution cause approximately 34 800 premature deaths per year and reduce life expectancy by 8.4 months (C. E. Kolb & Worsnop, 2012; World Health Org., 2006). The particles' large surface area provides the potential for surface reactions, such as radical reactions (Donaldson, Li, & MacNee, 1998). In addition to their effects on human health, aerosols have a significant impact on the Earth's climate system (T. Hoffmann, Zetzsch, & Rossi, 2007; Pöschl & Shiraiwa, 2015), due to their direct and indirect effect on the radiation budget (Curtius, 2006). The Copernicus newsletter, which is part of the European Union's Earth Observation Program, has released alarming temperature anomalies for October 2023. According to the report, 2023 is the warmest year on record, with the average global temperature reaching a warming of 1.5 °C. (Copernicus, 2023; Sanderson, 2023). This increase in temperature leads for example to higher sea levels. In addition, greenhouse gas emissions such as carbon dioxide, methane and nitrous oxide are significant contributors to climate change. While climate change is currently being researched by many scientists, basic research and the development of new techniques and methods for analysis are used to explore the world of invisible aerosols. One technique applies thermal desorption (TD) in conjunction with gas chromatography coupled to a mass spectrometer (GC-MS). This technique is known for monitoring lower boiling airborne volatile organic compounds (VOCs) as well as semi-volatile organic

compounds (SVOCs) (Duarte et al., 2022; Modey & Doskey, 2006; Vera, Villanueva, Wimmerová, & Tolis, 2022a). It is chosen for investigating aerosols due to its advantages of being fast, not complex, highly efficient with a low detection limit of analytes (Juillet, Dubois, Bintein, Dissard, & Bossée, 2014; Münz, 2010). The use of TD for injection finds application in air monitoring for, both industrial hygiene and in the workplace (Grote & Kennedy, 2002; Wu, Feng, Lo, Lin, & Lo, 2004). It is widely used for breath sampling. Various applications aim to identify biological processes (Drijfhout, Van Beek, Visser, & De Groot, 2000) or medical conditions (Filipiak et al., 2010; Sakai, Morita, Roh, Kim, & Kim, 2005; Śmiełowska et al., 2023) that produce specific indicative or patterns of VOCs. These applications include monitoring diabetes and stress, smoking, ambient outdoor and indoor air monitoring using passive and active methods (Woolfenden, 2010b, Gallego et al., 2011b; Smith et al., 2022; Raepfel et al., 2015). Further, industrial emissions to develop key test methods for industry (DIN EN 13649:2002-05, 2020). Furthermore, atmospheric research such as the topics on air pollution, climate, ozone layer are conducted (Hays et al., 2003; Yadav et al., 2013; Ding et al., 2009, Jiang et al., 2022; Berkemeier et al., 2016). Finally, gas exposure to soil, intrusion into buildings, and water odor should also be considered, soil gas (Woolfenden, 2010b), vapor intrusion into buildings (Woolfenden, 2010b, Roghani et al., 2018; Gallego et al., 2011a; Mcalary, 2014, Nieß et al., 2003).

Researchers have been studying the formation of aerosols, as well as the formation and growth of new particles for decades (Holmes, 2007; Kerminen et al., 2018; Raes et al., 2000; Vehkamäki & Riipinen, 2012). Currently, there is a discussion regarding the formation of highly oxidized molecules (HOMs) through gas-phase autoxidation, which requires extremely low-volatile organic compounds for nanometer particle growth (Ehn et al., 2014). Nanometer particles possess a unique chemical environment (Seinfeld & Pandis, 2006) and can influence chemical reactions in the newly formed condensed phase (Apsokardu & Johnston, 2018), acting as nanoreactors (Petrosko, Johnson, White, & Mirkin, 2016). In addition to pure gas-phase reactions, very low-volatility organic compounds can undergo heterogeneous oxidation reactions (Ervens, Turpin, & Weber, 2011; Nguyen et al., 2014; Pye et al., 2020), such as on the particle surface (Jang, Czoschke, Lee, & Kamens, 2002) or from organic salts (Barsanti, McMurry, & Smith, 2009; James N. Smith et al., 2010) through oligomerization reactions in the condensed phase (Wang et al., 2010; Zhang & Wexler, 2002). This study focuses on reactions that preferentially occur in particles in the nanometer size range. The reason for this is the need for matter to grow into size ranges where coagulation is no longer a factor, and instead bond-forming reactions take place (T. Hoffmann, 2018). In the size range of 10 to 100 nm, there is a significant gap between the initial formation of particle embryos and the growth of particles to sizes where their persistence is more guaranteed and cloud droplets can possibly form (T. Hoffmann, 2018). Therefore, there is great interest in particle size-dependent reactions (Böckmann, 2021; Riva et al., 2021). It is important

to consider the significant role that particles may play in the life cycle of atmospheric aerosols. (Curtius, 2006).

The particle is a nanoreactor, combining unique physical and chemical properties (Riva et al., 2021). This includes Laplace pressure, which is caused by the curvature of the surface (Y. Cheng, Su, Koop, Mikhailov, & Pöschl, 2015; M. Petters & Kasparoglu, 2020; Sarah S. Petters, 2022). In addition, the Kelvin effect, which means that the vapor pressure above a curved boundary surface is always higher than the same substance above a flat surface (Seinfeld & Pandis, 2006). The Diels-Alder reaction, a typical reaction in organic chemistry, is chosen as a model system to support these properties (García-Lacuna, Domínguez, & Pérez-Castells, 2020) for laboratory experiments. The developed setup consists of a modified tandem differential mobility analyzer (Joutsensaari, Vaattovaara, Vesterinen, Hämeri, & Laaksonen, 2001) and a flow tube. As the Diels-Alder reaction is a common occurring reaction in nature (Juhl & Tanner, 2009), the described experiments could contribute to the understanding of the fundamentals of biological aerosols. This study examines whether insects, specifically ants and their brood, emit a gas phase and thus may contribute to the formation of aerosols.

1.1 Atmospheric aerosol

An aerosol is a two-phase system consisting of a suspension of solid or liquid droplets, also known as particulate matter, in a gas (Hinds, 1999; Seinfeld & Pandis, 2006). Aerosols contain various types of particulate matter components, which originate from organic or inorganic sources and may be of natural, biogenic, or anthropogenic origin. Particles form e. g. from the soil, from combustion processes, photochemically, from salts of the ocean spray and from atmospheric clouds of water droplets or ice particles (Hallquist et al., 2009; Hinds, 1999). Aerosols are formed from the direct emission of particles or by the conversion of gases into particles in the atmosphere (Seinfeld & Pandis, 2006). Those that enter the atmosphere directly are called primary aerosols. If particles are formed solely in the atmosphere by chemical reactions of gas phase components, also known as gas-to-particle conversion, this is referred to as secondary aerosol (Hinds, 1999). The formation of atmospheric aerosol particles through new particle formation (NPF) is a major source (Spracklen et al., 2006; Yu et al., 2010) and was first described by Aitken in 1897 (M. Kulmala et al., 2004). This process will be described in the following chapter. The atmosphere contains a highly complex mixture of aerosols, with 20-50% (and up to 90% in forested areas like the Amazon) of the aerosol mass being black carbon (Kanakidou et al., 2005). Aerosols have a significant impact on the scattering and absorption of solar radiation (Hinds, 1999; John, 2011). This direct aerosol effect is caused by light scattering, which scatters sunlight back into space by fog or smoke, resulting in cooling of the earth (Pöschl, 2005). However, black carbon causes absorption of solar radiation, leading to a warming effect (Pöschl & Shiraiwa, 2015). Their contribution to cloud formation as CCN is called indirect influence (Seinfeld & Pandis, 2006). These CCNs are formed through condensation, which describes the sticking collision of a vapor on a condensed phase (M. Kulmala et al., 2004). When describing the properties of atmospheric aerosol particles, the particles size and shape must be considered (Hinds, 1999; Kulkarni, Baron, & Willeke, 2011; Riipinen et al., 2012). In general, the size of particles can range from a few nanometers for molecular clusters up to tens of micrometers for common particles such as dust (Seinfeld & Pandis, 2006). Laboratory experiments simulating atmospheric aerosols, be it through chamber experiments or flow reactors, provide valuable information for understanding (T. Hoffmann et al., 2007). Furthermore, modelling of atmospheric aerosols, such as gas-particle partitioning and water uptake under varying conditions, such as humidity, contributes to assessing health hazards. It also presents opportunities to utilize these effects.

1.2 New particle formation

In the atmosphere new particle formation (NPF) involves nucleation processes transform traces of condensable vapors into liquid or solid particles (Kolb and Worsnop, 2012) as introduced before. Nucleation in the molecular size range is defined as the clustering of molecules to reach a certain size of approximately 1 nm, at which point the resulting particles become thermodynamically stable (Markku Kulmala, 2003; Sellegri & Boulon, 2017). Figure 1.1 illustrates that nucleation. It can be induced by sulfuric acid and water, as well as by ammonia and HOMs (Curtius, 2006; Dunne et al., 2016). The oxidation of these primary gases results in the formation of substances with lower vapor pressures than the reactants. This can lead to condensation or the creation of new aerosol particles, a process known as gas-to-particle conversion (Dada et al., 2020; T. Hoffmann et al., 2007). After the formation of critical clusters so-called particle embryos, they can grow through the participation of low-volatile compounds to ultrafine aerosol particles (Curtius, 2006). By reaching certain size range cloud condensation nuclei (CCN) are formed. These nuclei can then grow into cloud droplets (Curtius, 2006). This work investigates the chemistry of particles in the marked size range of approx. 2 to 100 nm, which is shown to be size-dependent and growth-accelerating.

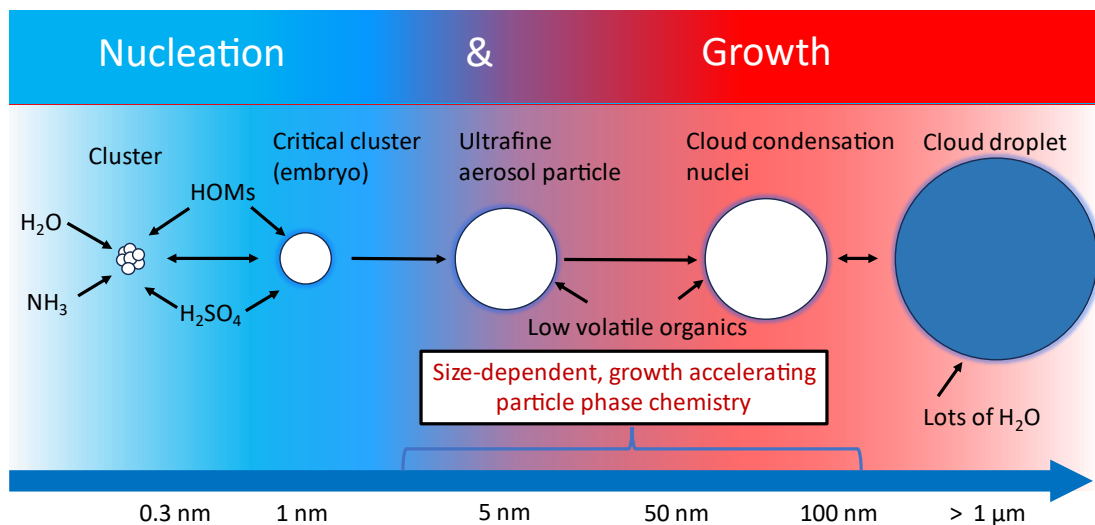


Figure 1.1 The illustration shows the nucleation and growth of the atmospheric nucleation of H_2SO_4 and H_2O . First, stable water clusters are formed, then low-volatile compounds can participate in the growth. When these reach a certain size, cloud condensation nuclei can evolve to form cloud droplets. In this work, the marked range of approx. 2 to 100 nm was investigated. Drawing adapted from Curtius, 2006.

The correlation between the dry diameter of particles and the CCN formed through hygroscopic growth can be used to forecast the CCN activity of mixed particles that contain surface-active materials (M. D. Petters & Kreidenweis, 2007). Supersaturation is

an important condition for nucleation (Holmes, 2007). This is the case when the partial pressure of the species is greater than the saturation vapor pressure over a flat surface of a liquid (Y.-S. Cheng, 2011). Organic molecules contribute to the growth of particles by influencing oligomerization reactions during the early stage of particle formation (Riipinen et al., 2012; Wang et al., 2010). These are heterogeneous reactions that involve species between the gas and particle phases. They occur at the interface between the aerosol particles and gas phase or within the particles (T. Hoffmann et al., 2007). To describe the thermodynamics of particles, some certain key aspects that differ from those of a flat interface must be considered (Seinfeld & Pandis, 2006).

The Kelvin-Effect describes the circumstance that the partial vapor pressure on a curved surfaces is higher than the vapor pressure of the same substance on a flat surface, which is called saturation vapor pressure p_s (Lewis, 2006; Seinfeld & Pandis, 2006). In the case of a strongly curved surface, there are fewer molecules near a molecule on the surface. This is due to the curvature of the surface. This reduces the attractive forces between the molecules on the surface and facilitates evaporation (Hinds, 1999). By maintaining mass equilibrium, meaning that the partial pressure of vapor surrounding the droplet is greater than the saturation vapor pressure p_s , evaporation is prevented (Hinds, 1999). The Kelvin ratio K_R describes the relationship for pure liquids between the saturation ratio S_R required for equilibrium, where no growth or evaporation takes place. The size of the droplet is determined by the Kelvin or Thomson-Gibbs equation (1.1) (Hinds, 1999).

$$S_R = K_R = \frac{p_d}{p_s} = \exp\left(\frac{4\gamma M}{\rho RT d^*}\right) \quad (1.1)$$

Here γ , M , and ρ represent the surface tension, molecular weight, and density of the droplet liquid, respectively. d^* describes the Kelvin diameter, which is defined as the diameter of a droplet that will neither grow nor evaporate when the partial pressure of vapor at the droplet surface is p_d (Hinds, 1999). The Kelvin equation is only applicable to pure liquids, as impurities and electric charges can affect vapor pressures, requiring modification of the equation (Hinds, 1999).

Another property of particles in a nanometer size range is the increasing internal pressure due to the surface tension called Laplace pressure (Butt, Graf, & Kappl, 2006). The pressure difference between the inside and outside of the particle can be calculated using the equation (1.2) of Young and Laplace (Sarah S. Petters, 2022).

$$\Delta p = \frac{2\gamma}{r_p} \quad (1.2)$$

Here, the symbol γ represents the surface tension and r_p represents the radius of the particle. The pressure of inside of aerosol droplets with a diameter of $1\ \mu\text{m}$ is comparable to the atmospheric pressure (de Gennes, Brochard-Wyart, & Quéré, 2004). However, as particle size decreases, the pressure difference increases. Figure 1.2 illustrates the relationship between the pressure difference across the particle surface and the particle diameter for different surface tensions. The surface tensions considered are water ($0.072\ \text{N m}^{-1}$), aqueous salts ($0.080\ \text{N m}^{-1}$) and organic ($0.030\ \text{N m}^{-1}$) (Sarah S. Petters, 2022).

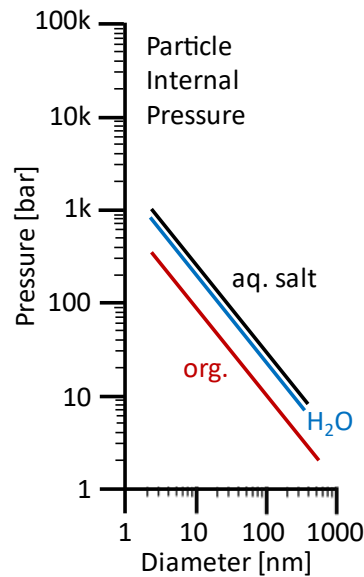


Figure 1.2 The surface tensions used were $0.080\ \text{N m}^{-1}$ for aqueous salts, $0.072\ \text{N m}^{-1}$ for water, and $0.030\ \text{N m}^{-1}$ for organic compounds. The graph, adapted from Sarah S. Petters, 2022, illustrates the relationship between particle internal pressure and diameters ranging from 3 to 500 nm.

1.3 Chemical reactions in nanometer aerosol particles and the gas phase

Chemical reactions occur within a specific volume, which is named according to the stage of the reaction. Figure 1.3 illustrates the relationships graphically. The volume of the reactants is defined by V_R . The volume of the transition state (V^\ddagger) denotes the volume of the transition state after completion of the reaction the volume of the products (V_P) refers to the volume of products. Furthermore, the changes in volume are referred to as activation volume (ΔV^\ddagger) and reaction volume (ΔV). The activation volume is defined as the difference in volume between the transition state and the reactants. The reaction volume is defined as the difference between the volume of the products and the volume of the reactants (Drljaca et al., 1998; R. Van Eldik, Asano, & Le Noble, 1989).

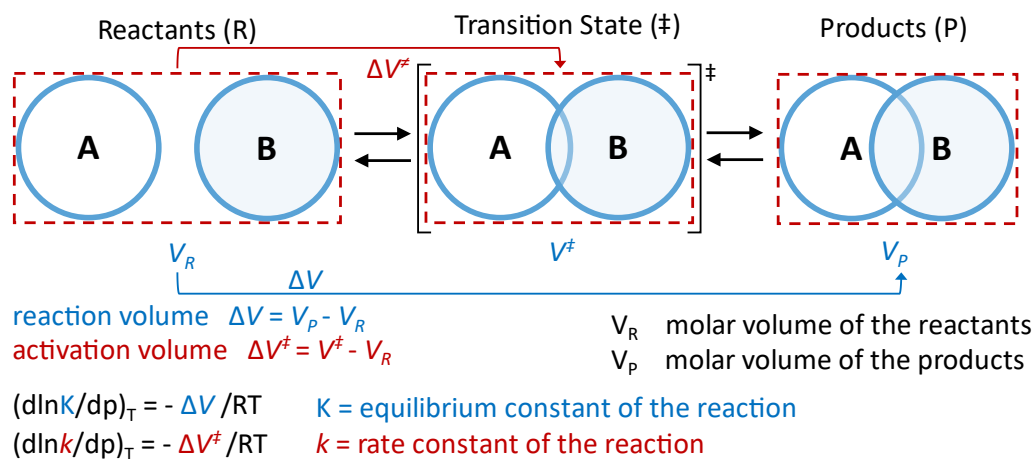


Figure 1.3 Volumes of reaction (ΔV) and activation (ΔV^\ddagger) adapted from Klärner and Wurche, (2000).

The activation volume is determined by measuring the impact of pressure on the reaction rate. Therefore, it is assumed that the entire response of the rate to the pressure is related to volume. This means that an increase in pressure can accelerate the rate of bond-forming reactions, such as oligomerizations, by causing a shrinkage as the reactants move towards the transition state. The opposite is also true. (Swiss & Firestone, 2000). In combination with the properties of nanometer-sized particles, the conditions are ideal for implementing size-dependent reactions (Sarah S. Petters, 2022; Riva et al., 2021).

1.4 Diels-Alder reactions

Diels-Alder reactions are well known in organic synthesis as [4+2]-cycloadditions between a conjugated diene and a dienophile. Otto Diels and Kurt Alder first introduced them in the 1920s (Diels & Alder, 1928, 1929b, 1929a). They are frequently a crucial step in the synthesis of natural products (García-Lacuna et al., 2020), as well as in industrial processes (Funel & Abele, 2013).

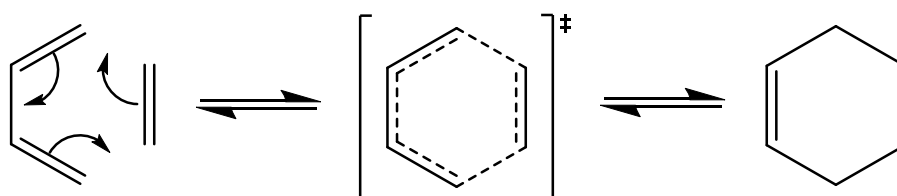


Figure 1.4 Schematic illustration of the Diels-Alder reaction. Modified from Clayden et al., 2012.

The simplest Diels-Alder reaction is the one between ethene and butadiene as displayed in Figure 1.4. A diene, here the ethene reacts with a dienophile, which is in this case an acceptor-substituted alkene. The reactants form a six-membered ring in a one-step reaction without any intermediates. Instead, there is a transition state in which all six π electrons are delocalized, resulting in an aromatic character (Clayden et al., 2012). This reaction is one of the most important stereoselective C-C bond-forming reactions in general (Brückner, 2002). The diagram in Figure 1.5 illustrates the frontier orbital theory, which explains that the normal Diels-Alder reaction is promoted due to the reduced energy gap between the lowest unoccupied molecular orbital (LUMO) of the dienophile and the highest occupied molecular orbital (HOMO) of the diene. Furthermore, the HOMOs of one reactant share the same symmetry as the LUMOs of the other reactant resulting in an overlap and the formation of a new σ bond. Thus, the LUMO of the electron-deficient dienophile overlaps with the HOMO of the diene in the transition state, as indicated by the blue dashed arrow in the illustration (Clayden et al., 2012). This orbital representation can be used to explain the molar volumes of the reactants, the transition state, and the products. The activation volume of the Diels-Alder reactions decreases at the transition state (Swiss & Firestone, 2000). The activation volume of the Diels-Alder reaction product exhibits a large negative reaction volume ($\Delta V < 0$) of -25 to -30 $\text{cm}^3 \text{mol}^{-1}$ indicating a preference for the kinetic endo diastereoisomeric product (Clayden et al., 2012; Grosch et al., 2004a). The carbonyl groups of the dienophile bond with the developing π -bond at the back of the diene, resulting in the observed interaction (Clayden et al., 2012). The Van der Waals distance is reduced from 3.6 Å to a C-C bond distance of 1.5 Å (Klärner & Wurche, 2000).

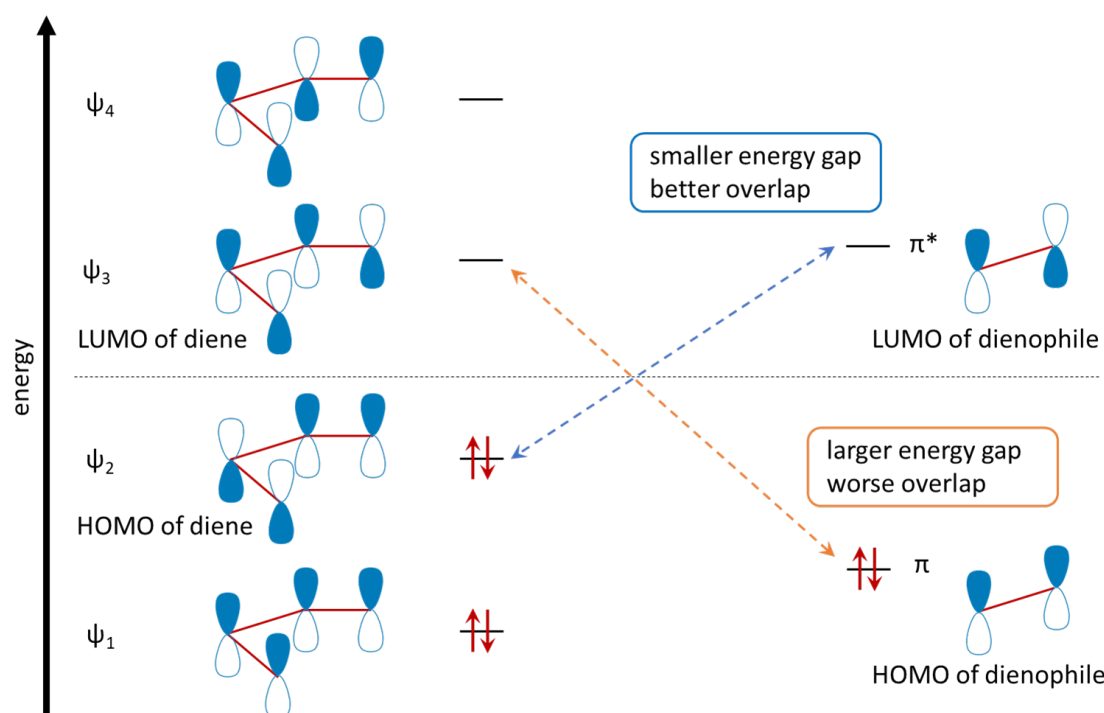


Figure 1.5 Drawing of the frontier orbital description of the Diels-Alder reaction adapted from Clayden et al., 2012. It illustrated the energy levels of the HOMOs and LUMOs of a diene and acceptor substituted dienophile.

In addition, solvents can affect the activation volume through changes in the solute-solvent and solvent-solvent interactions, such as dielectric constant and viscosity (Vladimir D. Kiselev et al., 2001). Cycloadditions are catalyzed by Lewis acids because they result in more negative activation volumes, caused by bonding between the acids and the dienophile (Drljaca et al., 1998). The Diels-Alder reaction can be accelerated by high-pressure, which is another factor of interest (Grosch et al., 2004a; Jenner, 1975). As shown in Figure 1.4, the transition state follows a concerted four-center mechanism involving a quasi-aromatic conjugated ring that is affected by both electron withdrawal and donation from substituents (McCabe & Eckert, 1974; Tu, Yin, Lin, & Bao, 2017).

Since the viscosity of organic solvents increases with the increase of pressure, diffusion control can be achieved. The increase in viscosity leads to a decrease in the number of collisions. Therefore, the process rate description should include the diffusion control (V. D. Kiselev, Kashaeva, Shihab, Potapova, & Iskhakova, 2004). As for organic liquids, the viscosity increases, while for viscous or solid particles, it decreases. This implies that the internal pressure is an important consideration for nanometer aerosol particles (Sarah S. Petters, 2022). Under these conditions, the Diels-Alder reaction equilibrium should shift towards the product side in nanometer aerosol particles.

1.5 Growth factor

Particle growth depends on the formation of compounds with low vapor pressure that can migrate into and remain within the particle (George & Abbatt, 2010; Seinfeld & Pandis, 2006). This process competes with coagulation of larger particles, resulting in a change in particle size that is described by the growth factor parameter. A tandem differential mobility analyzer can be used to measure using the growth factor (GF) of a particle size distribution. Chapter 4 provides a more detailed explanation of the analyzer's configuration. The measurement parameter is necessary to quantify the hygroscopicity of various particle. The GF is defined as the ratio of the particle diameter at a given humidity to the dry diameter. The process involves selecting dry particles using an initial differential mobility analyzer (DMA) followed by humidification. The size distribution is then measured using a second humidified differential mobility analyzer coupled with a condensation particle counter (Hämeri, Väkevä, Hansson, & Laaksonen, 2000; Schurman, Kim, Cheung, & Chan, 2017).

The purpose of this study was to determine the growth factor and verify whether a reaction had occurred in the particle. The growth factor was determined using the particle size distribution obtained with a Scanning Mobility Particle Sizer (SMPS), the operation of which is explained in chapter 2.4. To compare the two experiments, the geometric number mean of the size distribution was calculated, and the mean diameter of the grown particle was divided by that of the educt.

1.6 Reaction rates

To comprehend the kinetics of a reaction, one must study the reaction rate. (Becker, 2015; Clayden et al., 2012). The rate r of a chemical reaction, in this case the Diels-Alder reaction, is described by equation (1.3), according to Maskill, 2007.



The reaction outcome depends on the type and concentration of reactants A and B, as well as the stoichiometric coefficients v_a , v_b and v_c . In the case of the Diels-Alder reaction, these coefficients correspond to the diene or the dienophile. The reaction described is a second order reaction as reported by Meijer et al., 1998. The rate of the reaction can be determined using equation (1.4) provided by Maskill, 2006 that relates the reaction time t .

$$r \propto \left(\frac{-1}{v_a} \frac{d[A]_t}{dt} = \frac{-1}{v_b} \frac{d[B]_t}{dt} = \frac{+1}{v_c} \frac{d[C]_t}{dt} \right) \quad (1.4)$$

The rate of change of a reactant represented by $d[A]/dt$, is negative due to the decrease in concentration of [A] during the reaction. Conversely, the concentration of products [C] increases, resulting in a positive $d[C]/dt$ term. The second-order rate constants k for the formation can be calculated using the equation (1.5) adapted from Maskill, 2006.

$$-\frac{d[A]}{dt} = k[A]_t[B]_t \quad (1.5)$$

A rate enhancement factor rate k_p/k_0 is implemented as in equation (1.6) to adjust the reaction rates according to the applied pressure, as pressure influences the reaction rates (Eldik et al., 2002)

$$\frac{k_p}{k_0} = \exp \left[-\frac{\Delta V^\ddagger}{RT(p-1)} \right] \quad (1.6)$$

The reaction rate constant at high pressure, k_p , and the experimental reaction rate constant k_p of the reaction in the particle are related to the rate constant at the reference pressure k_0 at 1 bar. The negative volume of activation is described by ΔV^\ddagger , while p represents the high pressure, R is the universal gas constant ($8,314 \text{ J mol}^{-1} \text{ K}^{-1}$) and T the temperature, which, in this study, is 298.15 K.

1.7 Volatile organic compounds

Volatile organic compounds (VOCs) are organic compounds that have a high vapor pressure at room temperature, and they include all atmospheric organic trace gases except carbon dioxide and carbon monoxide (Seinfeld & Pandis, 2006). VOCs can be subdivided according to their vapor pressure. Organic compounds with a vapor pressure greater than 10 Pa at 25 °C and a boiling point of up to 260 °C at atmospheric pressure and 15 or fewer carbon atoms are considered as VOCs (Koppmann, 2007). The remaining organic compounds are named semi-volatile organic compounds (SVOCs) (Koppmann, 2007). Table 1.1 provides an overview according to Vera et al., 2022b of the classification of VOCs according to the WHO, based on their boiling point. Very volatile organic substances (VVOCs) have a boiling point between 0 and 50 °C, followed by VOCs with a boiling point of 50 to 240 °C. The boiling point range of 240 °C to 380 °C defines the SVOCs. The VVOCs and the VOCs are gaseous species. SVOCs can partition between the gas and the aerosol phase (Tomasi, Fuzzi, & Kokhanovsky, 2017).

Table 1.1 Classification of volatile organic compounds (VOCs) from the World Health Organization (WHO) adapted from Vera et al., 2022b.

Category Description	Acronym	Boiling point range [°C]
Very volatile (gaseous) organic compounds	VVOCs	<0 to 50
Volatile organic compounds	VOCs	50 to 240
Semi-volatile organic compounds	SVOCs	240 to 380
Organic compounds associated with particulate matter: Particle-bound organic compounds	POCs	>380

However, the definition of volatility in this context is vague, as noted by Koppmann, 2007. Volatility is typically described by the vapor pressure, which correlates with low boiling points (Abernathy, Berry, & Anderson, 2023). This property is determined by the functional groups of the molecule (Seinfeld & Pandis, 2006). The United States Environmental Protection Agency (EPA) specifies that substances with high vapor pressure and low water solubility are included (Abernathy et al., 2023). If a pure substance is in equilibrium with its vapor, its partial pressure in the gas phase is defined as the saturation vapor pressure (Seinfeld & Pandis, 2006). The Clausius-Clapeyron equation (1.7) gives the dependence of the saturation vapor pressure p_s on temperature (Seinfeld & Pandis, 2006).

$$\frac{dp_s}{dT} = \frac{\Delta H_v(T)M}{T(v_v - v_l)} \quad (1.7)$$

Where ΔH_v represents the latent heat for evaporation, M is the molecular weight, and v_v and v_l are the molar volumes of the vapor and liquid (Seinfeld & Pandis, 2006). A decrease in temperature results in a decrease in the saturation vapor pressure (Seinfeld & Pandis, 2006). The molecules of VOCs have a strong tendency to escape from the surface of their condensed phase (Abernathy et al., 2023) and remain in the gas phase, resulting in a high saturation vapor pressure. Organic substances with a low saturation vapor pressure are preferred for nucleation growth (Seinfeld & Pandis, 2006). VOCs in the atmosphere can originate from anthropogenic or biogenic sources. Many processes produce emissions of organic compounds including carbonyls, alcohols, alkanes, alkenes, and esters (Koppmann, 2007).

This work focuses on biogenic volatile organic compounds (BVOCs), which are VOCs of biological origin emitted from vegetation, living organisms, soil, and the oceans. BVOCs include various organic substance classes such as isoprenoids, alkanes, alkenes, alkynes, carbonyls, alcohols, esters, ethers, and acids (J Kesselmeier & Staudt, 1999). Vegetation, also known as plants, absorb carbon dioxide (CO_2) through photosynthesis and release it back into the atmosphere in the form of isoprene or terpenes, which are highly reduced (Fuentes et al., 2000; Guenther, 2002; Jürgen Kesselmeier et al., 2002). The emission of BVOCs depends on a range of factors, including the plant's age, health, and external conditions such as ambient temperature, location, and humidity. The exact composition and quantity of BVOCs emitted vary among different plant species (Guenther et al., 1995; J Kesselmeier & Staudt, 1999).

Both plants and animals emit organic substances, which are often used as signal transmitters in the air (Greene & Gordon, 2003; Krieger & Breer, 1999). For example, insects (Cremer, Sledge, & Heinze, 2002) and plants use elaborate chemical mimicry to ward off attackers (Kessler & Baldwin, 2001). The most emitted molecule is isoprene (C_5H_8), followed by other reactive biogenic substances which are mainly oxidized compounds and monoterpenes (Koppmann, 2007). Isoprene is a short-lived substance of plant and animal origin and a precursor for other BVOCs, such as alpha-pinene. It forms the basic unit of many natural compounds, including steroids and terpenes (Koppmann, 2007). Terpenes also include terpenoids, which, unlike terpenes, have functional groups or a slightly different carbon skeleton. Many terpenoids are of plant origin and can be obtained from their essential oils. Terpenoids have a broad range of functions, including playing a role in the growth and development of the plant (i.e. primary metabolism) and the essentiality of sterols (C_{30}) for membranes. Carotenoids (C_{40}) are photopigments. Some species contain secondary metabolites, such as monoterpenes (C_{10}), sesquiterpenes (C_{15}) and diterpenes (C_{20}), which were previously

considered waste products and do not play a role in the primary metabolism of the cell (Hartmann, 2007).

Social insects use BVOCs for communication. In 1967, von Frisch (1967) demonstrated that honeybees dance to inform their nest members about the location of resources, for which he was awarded the Nobel Prize in 1973. Communication occurs chemically through hormones and pheromones (Leonhardt, Menzel, Nehring, & Schmitt, 2016). Given that this study focuses on ants and their brood (Formicidae), the theoretical background will center on the BVOCs them.

The covering of the cuticles of all insects are covered by cuticular hydrocarbons (CHC), which serve as waterproofing agents and sex pheromones (Menzel, Blaimer, & Schmitt, 2017). Additionally, they can function as a chemical cue for recognizing mates and nestmates (Kather & Martin, 2015). The texture is semi-fluid and can be imagined as viscous wax layer as the hydrocarbons aggregate tightly, relying on Van-der-Waals forces (Menzel et al., 2017). The composition is mainly determined by genetic factors (van Zweden, Dreier, & d'Ettoire, 2009). CHCs can provide information about the group's status and the reproducibility (Menzel et al., 2017; Pamminer et al., 2014). They are exchanged through trophallaxis (passing liquid food from the mouth or anus of one animal to another) and allogrooming (physical contact such as cleaning (Boulay, Hefetz, Soroker, & Lenoir, 2000; V. Soroker et al., 1995; Victoria Soroker, Vienne, & Hefetz, 1995). Each colony has a unique scent when in contact with their nestmates (Boulay et al., 2000; V. Soroker, Vienne, Hefetz, & Nowbahari, 1994). Chemically, CHCs describe a complex profile with over 100 different substances that are difficult to identify. In detail, you get different molecules with the same molecular formula can be obtained by varying the number and position of the hydrocarbon atoms as well as whether they are saturated or unsaturated, branched, or linear (Menzel et al., 2017). This diversity of hydrocarbons may be due to the varying demands placed on the CHC layer (Wittke, Baumgart, & Menzel, 2022). On the one hand, it should be waterproof, which tends to favor more viscous hydrocarbons (Rourke & Gibbs, 1999). On the other hand, this property hinders the exchange of the CHC layer between the ant and the brood. Alkanes with methyl groups or branched molecules that aggregate less are more favorable (Menzel et al., 2019).

The common method used for the analysis of CHCs is the preparation of solvent extracts. This is done by soaking ants in different solvents and then extracting them or by washing the ant with a solvent and then collecting it. The solvent extracts obtained are analyzed using GC-MS (Beros, Foitzik, & Menzel, 2017; Guarda & Lutinski, 2020; Menzel et al., 2017). The method developed in this work is suitable for the analysis of volatile CHCs or components present in the gas phase of living ants or the brood that keeps them alive. Further details can be found in chapter 2.2 and 7.

2 Analytical methods and instruments

This chapter explains the basics of the new analytical methods developed in this work, which required the construction of new instruments.

2.1 Laboratory flow tube experiments

Flow tube reactors utilized to study the kinetics of aerosols. The aim is to investigate the complex growth kinetic processes of nanometer-sized particles. The particle size distributions at the inlet and outlet are typically measured over time to gain insights into these processes. However, in this study, only the outlet particle size distribution was measured. Wall losses were neglected in the subsequent data evaluation. Figure 2.1 shows that the flow tube is about 1600 mm long with a diameter of 100 mm, made of glass, and has a volume of 11.8 L. Both ends of the flow tube reactor converge cylindrically. The inlet has a 29/32 ground joint, and the outlet has a 14/16 ground joint. The flow tube reactor was connected to tubing olives and tubing using ground joints, allowing for easy and functional connection. The experiments were conducted under laminar flow at atmospheric pressure.

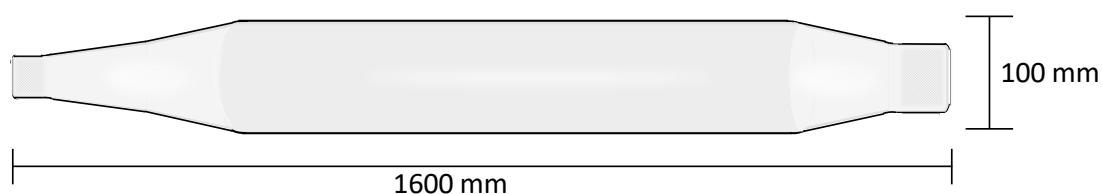


Figure 2.1 Drawing with dimensions of the build flow tube reactor used for the particle growth experiments.

2.2 Glass device for sampling living insects

This section provides technical details of the glass device developed for experiments on living insects, specifically ants and their brood. The glass appliance comprises two main parts. Figure 2.2 illustrates a schematic drawing and a photograph of the construction.

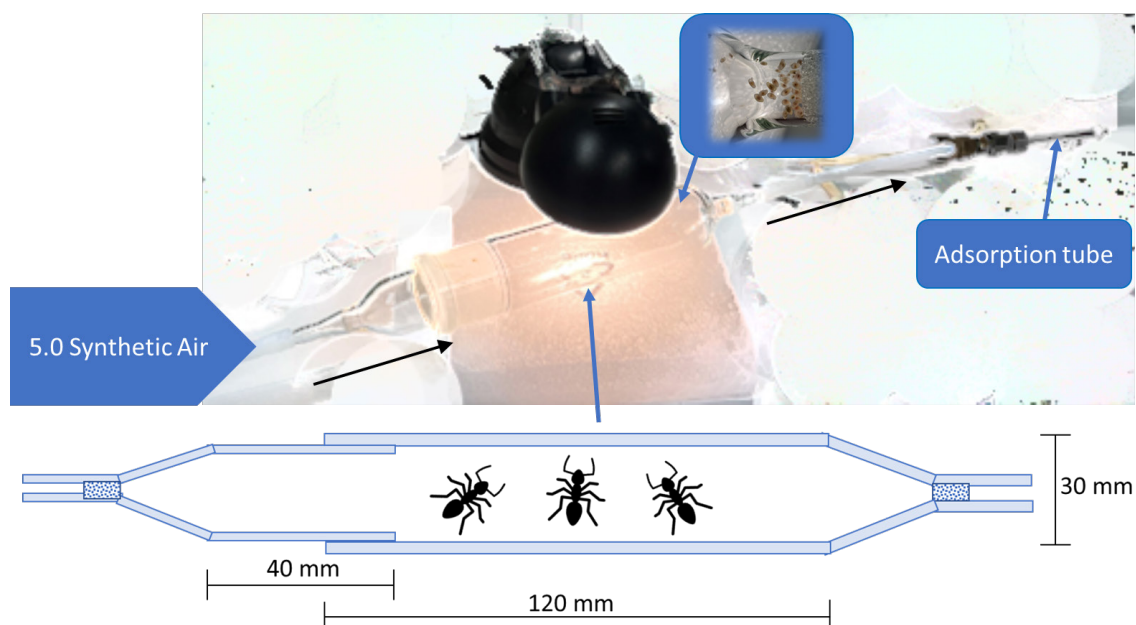


Figure 2.2 This is a non-invasive device designed for sampling the gas phase of ants and their brood. The author took the accompanying picture.

The left part features an olive with a core NS 29/32 and an inner frit with a porosity of 3 melted into it. Its diameter is approximately 30 mm. The right part consists of a 12 mm long glass tube with an olive at its right end, also featuring a frit with a porosity of 3 melted into it. Both parts have a cut that allows them to be inserted into each other. The purpose of the two inner frits is to prevent coarse foreign bodies from entering the glassware and to keep ants or brood from escaping. The glassware was entirely made from DURAN® borosilicate 3.3 by the glassblower. This type of glass is renowned for its excellent chemical resistance, high temperature resistance, and minimal thermal expansion. Additionally, glass allows for easy observation of the objects being examined.

2.3 Sampling and chemical analysis

2.3.1 Thermal desorption as an injection technique

TD is a versatile technique used to inject gases, volatile organic compounds, and aerosols. It is an extension of gas chromatography (GC), where the sample material or sorbent on which the analyte is adsorbed, is heated, and volatile substances are desorbed by introduction of an inert carrier gas. The desorbed material is then transferred into the GC column. By desorbing the analyte into a smaller volume of gas, as described in this chapter, the analyte can be enriched, improving sensitivity and detection limits. This technique was developed to overcome the limitations of standard GC injection techniques, such as liquid extraction or steam distillation, which require longer sample preparation, use more resources, and use more solvent, which has a negative impact on the environment. In addition, the TD injection method eliminates the risk of sample dilution. TD is typically combined with GC or GC coupled to an MS. Figure 2.3 illustrates the operating principle of this technique. The analytes collected on an adsorption tube are desorbed thermally over an extended period and concentrated in a focusing volume. This step is referred to as (1) primary (tube) desorption. The focusing volume, which can be a cooled capillary or adsorption trap, is then rapidly heated to provide a narrow injection of analytes for subsequent chromatography. This step is referred to as (2) secondary (trap) desorption.

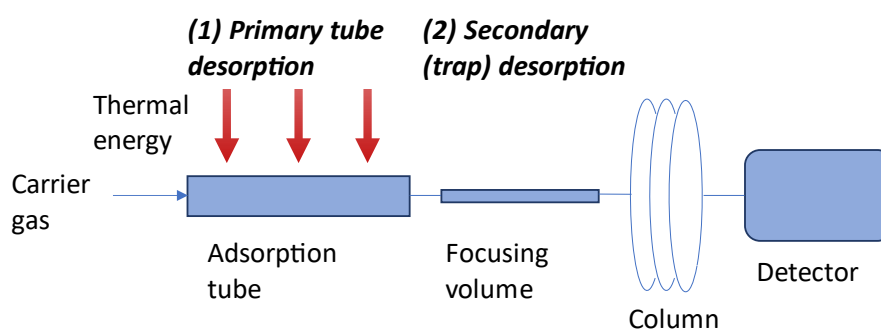


Figure 2.3 Operating Principle of TD injection coupled to a GC-MS adapted from Dettmer and Engewald, 2003.

The key parameters of a TD method are the sorbent choice (in the adsorption tube and cold trap), temperature, gas flow, and time of each step. Additionally, relevant factors include the material of internal screw connections and valves, as well as the presence of leaks.

There are several devices based on the same principle. This section presents three possibilities, focusing on gas flows, specifically the path of the sample. First, a commercial TD injector from Markes is described, followed by the TD injector built in-

house, which has been continuously developed by several generations of PhD students, starting with Prof Hoffmann. This chapter outlines the original version prior to conversion and the subsequent improvements made in this work. Further details on these improvements can be found in chapter 5. The gas flows follow the same path in both versions. Finally, the newly developed TD injector is introduced.

The TD injector UNITY-xr from Markes consists of a sample tube holder, a heated valve module, a heated transfer line attachment, a cold trap box, and a split filter or recollection tube, as shown in Figure 2.4. The injector's electronics, includes several electronic MFCs to adjust gas flows, are not visible in this image. Gas flow adjustment, method selection, and communication with the GC-MS are performed using the supplied software (Markes International Ltd., 2019b).

UNITY-xr Markes TD

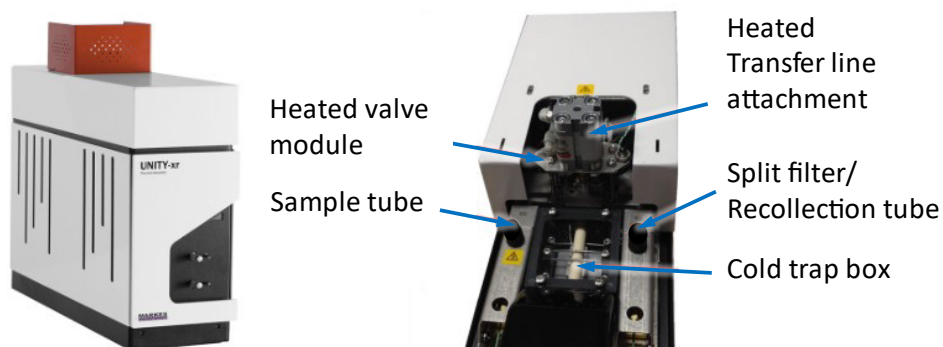


Figure 2.4 Outside and overview of the commercial TD injector UNITY-xr from Markes (Markes International Ltd., 2019b).

The UNITY-xr provides various options and additional features for the first and second desorption. Figure 2.5 illustrates a two-stage method. During the first desorption (1), the carrier gas is split to supply both the GC and the sample flow tube. The sample then enters the focusing trap, which is cooled customarily to -30°C by a Peltier element. This gas flow is referred to as trap flow. The sample flows from the sample flow tube to the focusing trap via a heated valve with a maximum temperature of 210°C . To prevent overloading of the focusing trap with solvent and water, an additional split flow is employed. This also allows for higher flows during the first desorption, which can be advantageous for the desorption of SVOCs. (Markes International Ltd., 2019a). The second desorption follows, where the carrier gas flows through the focusing trap from the opposite direction while being heated. The sample enters the GC column with the column flow through the heated valve. It is possible to apply a split flow at this point to reduce the sample concentration, which can improve peak shape and signal-to-noise

ratio, thereby enhancing the method's sensitivity (Markes international Ltd., 2013; Markes International Ltd., 2019a, 2019b).

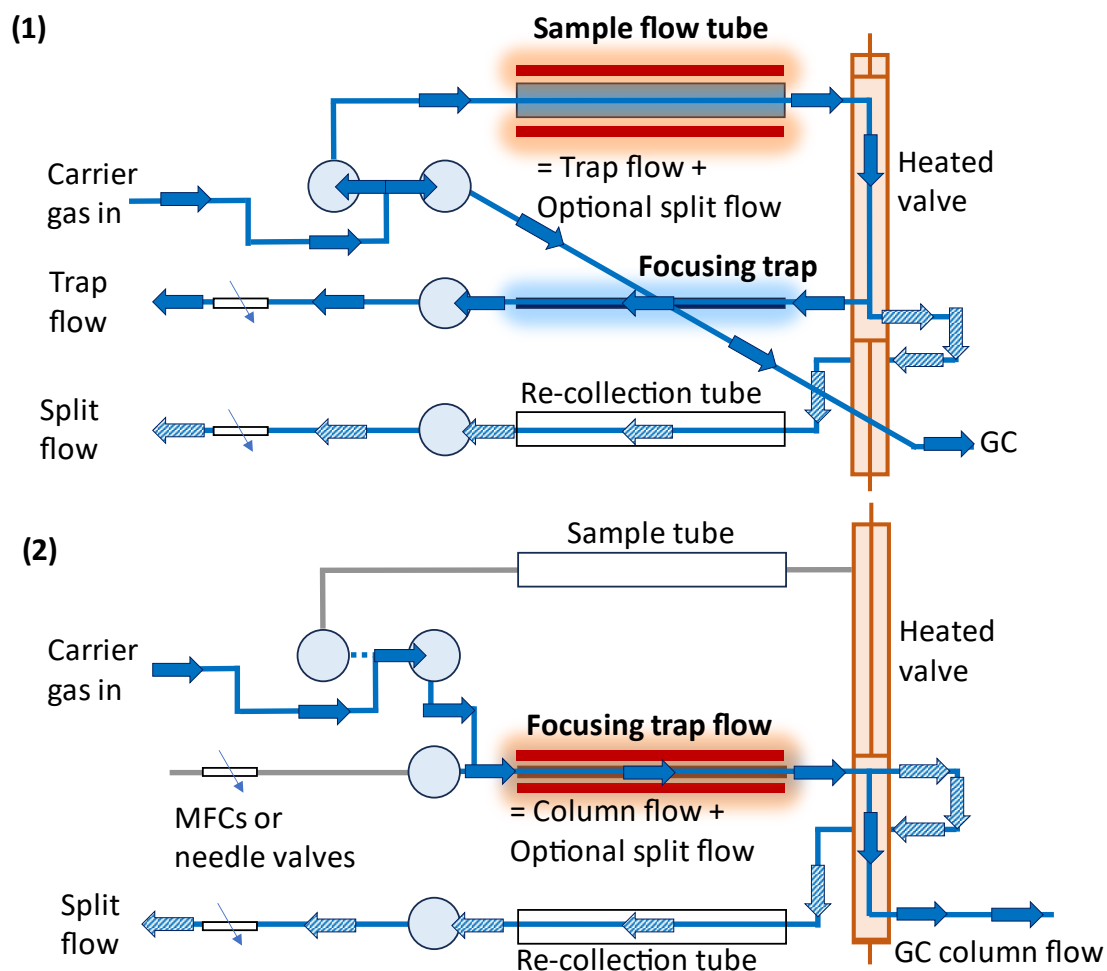


Figure 2.5 The drawing, adapted from (Markes international Ltd., 2013), shows the gas flows during (1) Primary (tube) desorption and (2) Secondary (trap) desorption through the injector to the GC.

The in-house TD injector was originally built by Prof. Hoffmann in 1992 and has been continuously developed and adapted to meet research needs (T. Hoffmann, 1992). Julia Münz made the first improvements, and in 2018, Simon Probst automated it. (Münz, 2010; Probst, 2018). Figure 2.6 illustrates the in-house TD injector, which comprises a TD oven, a focusing trap, a cooling device for the focusing trap, and a split after the focusing trap. The TD oven and focusing trap are vertically arranged directly above the GC. The motor of the TD oven, the valves for the corresponding gas flows, and the start signal to the GC are controlled by an Arduino Uno microprocessor. The appendix of this thesis contains a schematic of the in-house TD developed by Simon Probst. The Arduino is controlled using National Instruments' LabVIEW (Laboratory Virtual Instrumentation

Engineering Workbench) software, which is a graphical programming system that operates based on the data flow model (National Instruments, n.d.). This is comparable to the UNITY-xr TD, where the user has a front panel to start and monitor the TD. (Münz, 2010; Probst, 2018). This injector ensures that the carrier gas flows continuously through the system. To prevent any interruption in the helium flow through the entire system, an empty tube with connectors is screwed into the flow path at the TD oven. When measuring a sample, the focusing trap, which typically consists of a 0.5 mm metal capillary, is first cooled to -196°C using liquid nitrogen. The adsorption tube with the sample is then attached using two open-end wrenches. The GC-MS methods are written using Thermo Fisher's Xcalibur software (version 1.2) and are independent of the TD injector.

In-house build TD

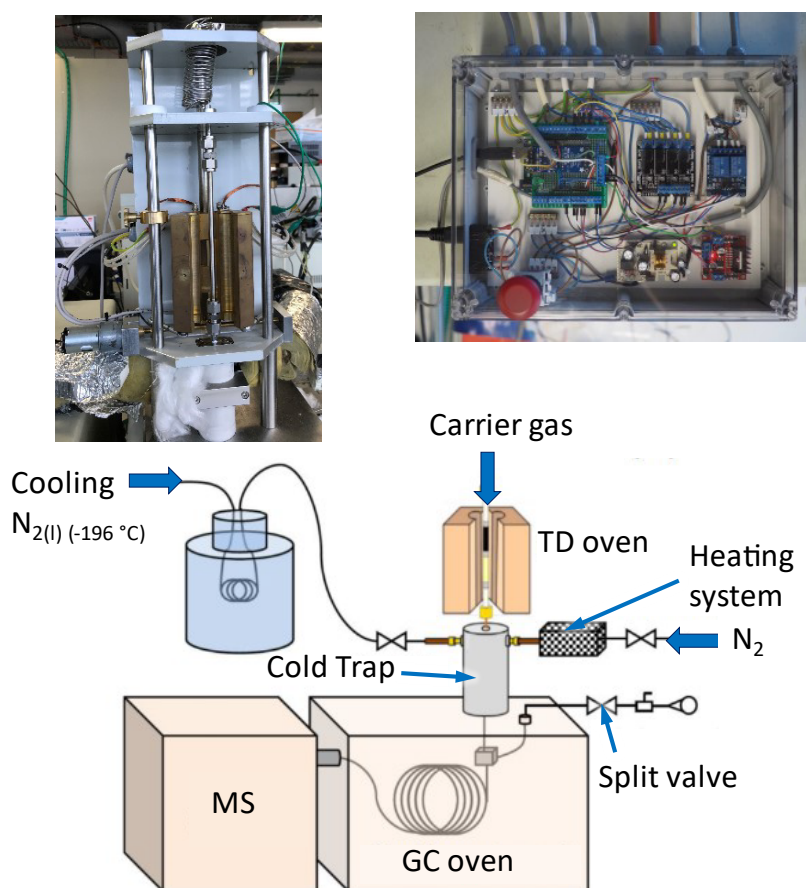


Figure 2.6 An image of the home-built TD injector and the Arduino controller with an illustration of the system components adapted from Münz, (2010) is displayed.

The TD process begins with the assistance of LabVIEW software. In the primary desorption stage, the split is open to ensure efficient desorption with increased gas flow as depicted in Figure 2.7. The TD oven is then closed off for measurement using a motor

and begins to heat up. Once the target temperature of a maximum of 250 °C is reached, it is maintained until the sample has fully entered the focusing trap. Secondary desorption is performed by rapidly heating the trap in the same direction as the primary desorption, along with the start of the GC-MS method. The temperature is maintained at a maximum of 230 °C to ensure complete entry of the analyte into the GC. The split is usually closed during the second desorption, unless the sample is too concentrated, in which case measurement with split is possible.

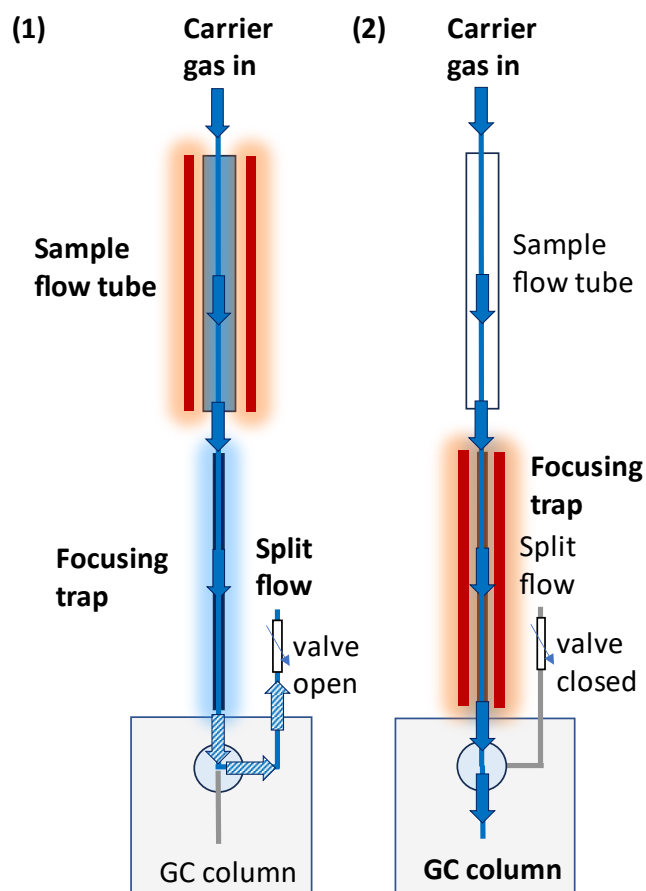


Figure 2.7 overview drawing of the system components and on the right the gas flows during (1) Primary (tube) desorption and (2) Secondary (trap) desorption through the injector to the GC.

The versatile TD injector developed and built in this thesis is based on our expertise with the in-house TD injector as well as the working group's recent experience with TD injectors. Figure 2.8 shows an image of the versatile injector and its position on the GC-Orbitrap-MS on the right. It was developed based on the in-house TD injector. Chapter 0 describes the development and its objective, while chapter 0 provides a detailed description of an application.

The TD injector is a versatile tool that comprises a TD oven, a focusing trap, a transfer line, a cooling device for the focusing trap, and a split after the focusing trap. It is worth noting that this injector does not use automation, meaning that the respective processes are controlled manually.

Versatile TD



Figure 2.8 The image on the left shows the Versatile TD injector, while the view on the right displays the entire system, including control systems and installation on the GC-MS.

Figure 2.9 shows the schematic arrangement of the components. Like the in-house TD, the carrier gas flow is interrupted for desorption, and the empty tube is replaced by the sampled adsorption tube. In the versatile TD, primary desorption occurs from bottom to top. The oven is manually closed and started, and the control unit of the heating rods in the oven displays the current temperature. A timer is utilized to pause until the designated temperature is attained and the allotted time has passed.

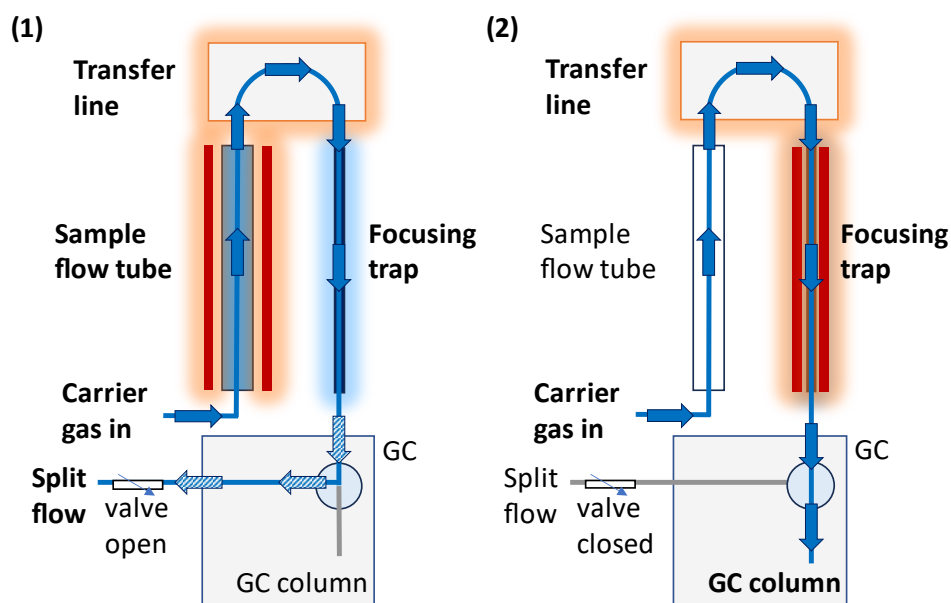


Figure 2.9 The drawing illustrates the system components, and the gas flows during (1) primary (tube) desorption and (2) secondary (trap) desorption through the injector to the GC.

The analytes pass through the transfer line, which is permanently heated to 250 °C, into the focusing trap, which is cooled with liquid nitrogen, in a silanized metal capillary. Here, the gas flow changes direction by 180 degrees and now runs from top to bottom. The split is also open in a standard method during primary desorption with this TD. After the set time has elapsed, the split is closed to begin the secondary (trap) desorption. The GC-MS method must be started on the GC at the same time. Then, the focusing trap is heated to a maximum of 250 °C using a hot air soldering station. Once the target temperature has been reached, it is maintained until all the analytes from the focusing trap have been transferred to the GC column.

One technique for thermal desorption involves sampling the analyte on an adsorption tube, as previously described. The choice of sorbents in the tube is crucial for efficient uptake during sampling and release of the analyte during TD, depending on the type of analytes. Investigations of analytes with different adsorption properties have led to the introduction of so-called multibed packages. The tubes are filled with various sorbent materials to minimize the uptake of analytes that are too strongly adsorbed and cannot be desorbed from the sorbent (B. Kolb, 1999). Inert coated stainless steel or glass tubes were utilized in this study. The stainless-steel tubes are modified through silanization to deactivate the metal surface. They are then filled with a universal sorbent purchased from Markes International Ltd. The term 'universal' refers to three sorbent materials

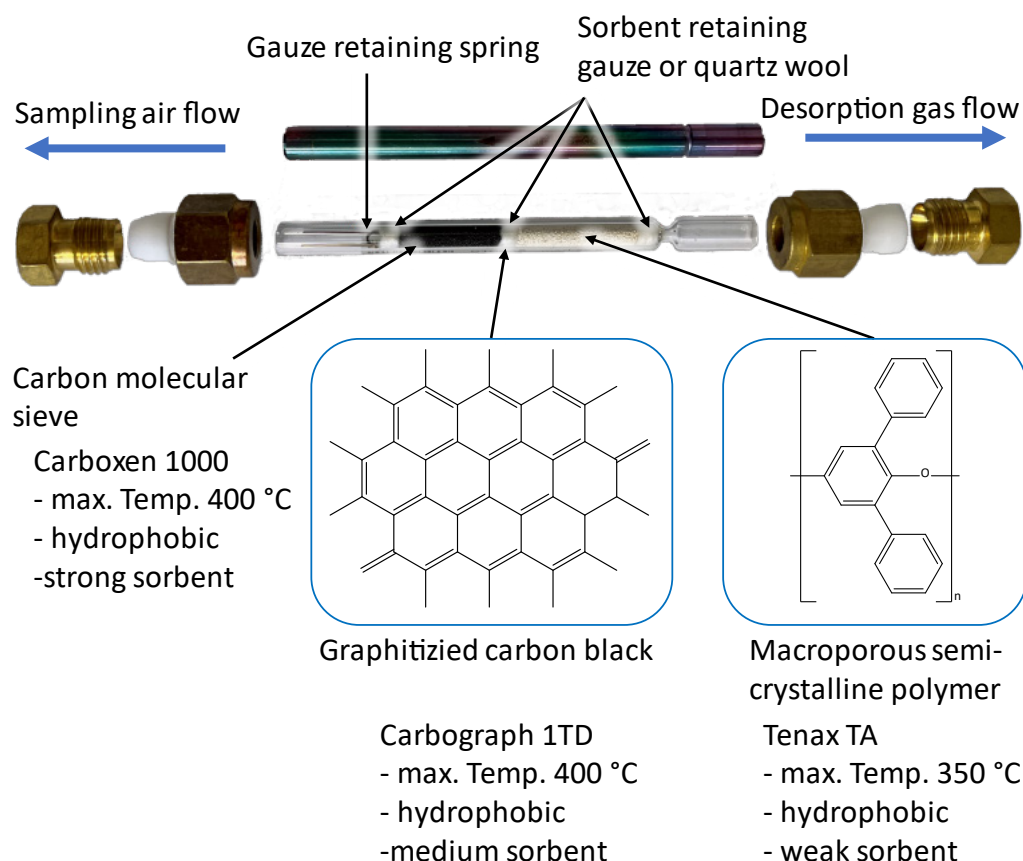


Figure 2.10 Own picture of an inert coated stainless steel and glass adsorption tube from Markes with selected Teflon ferrules and brass nuts and fittings and information about the sorbents Carboxen 1000, Carbograph 1TD and Tenax TA.

with different strengths that, when combined, cover a wide range of volatilities. Figure 2.10 displays the chemical structure of the three sorbents and their arrangement in the adsorption tube. The sample is first passed through a weak sorbent, a synthetic polymer Tenax TA (Poly-2,6-diphenyl-p-phenylenoxide), followed by a weak to medium sorbent, Carbograph 1 TD, a graphitized carbon black. Finally, a strong sorbent, Carboxen 1000, a carbon molecular sieve, is employed. These universal tubes are preferred due to their elevated temperature stability and are commonly chosen when the analytes in the sample are unknown (Even, Juritsch, & Richter, 2021). The tubes are sealed using Teflon ferrules with nuts and fittings, as shown in Figure 2.10.

2.3.2 Gas chromatography

After the injection of the analytes by TD or another technique they are separated by GC. This is a very common analytical separation technique based on the distribution of the substance to be separated between a stationary and a mobile phase. The stationary phase is often a column coated with a polymer film and the mobile phase is a gas. The separation of the analytes is based on their vapor pressure and polarity. For separation,

the temperature of the oven is increased with a certain gradient or temperature plates are used for separation. The GC is employed to separate substances that can be vaporized up to 400 °C without decomposition.

A gas chromatograph consists of the following components: an injection system, a carrier gas supply line, and an oven with a precise temperature program equipped with a separation column, which separates and transports the analytes from the injection system to the detection system. Depending on the analytes, the temperature rises from, for example, 50 °C to over 250 °C, separating the analytes due to their different vapor pressures and boiling points. As the analytes are transferred through the column by the mobile phase, they are repeatedly adsorbed and desorbed from the stationary phase. The higher the vapor pressure of the analyte, the shorter the adsorption time on the stationary phase, resulting in a shorter retention time. The polarity of the analyte can also play a role in the interaction with the stationary phase. Because of their inertness, helium, hydrogen, or nitrogen are used as carrier gases. The most used detection system today is a mass spectrometer, but a flame ionization detector or others are also possible (Harris, 2014).

2.3.3 Mass spectrometry

Mass spectrometry (MS) is a technique used to determine the mass of atoms, molecules, or fragments. To achieve this, the molecules are ionized, separated based on their mass-to-charge ratio (m/z ratio), and then detected both, qualitatively and quantitatively. A mass spectrometer typically consists of an injection unit, an ionization unit, one or more mass analyzers, a detector, and a vacuum system.

The analytes are transferred to the ionization source using either a direct injection method or a GC coupled to the MS. No-charged species are charged at this stage. The ions are then separated based on their mass-to-charge ratio in the mass analyzer. Finally, a second mass analyzer is in operation to further fragment and analyze selected ions. The fragmented ions are converted into electrical signals by the detector. The computer receives the electrical signal from the detector and controls the instrument while processing the data.

Ion sources produce ions primarily through gas-phase ion-molecule reactions, such as electron ejection, electron capture, protonation, deprotonation, and adduct formation, or by transferring charged species from a condensed phase to the gas phase (E. de Hoffmann & Stroobant, 2007).

This work exclusively used electron ionization, also known as electron impact, as the ionization source. This form of ionization is highly energetic and causes extensive fragmentation of the molecule. It is widely used in mass spectrometry, but is only

suitable for gas phase ionization, limiting its use to compounds that are sufficiently volatile and thermally stable.

Figure 2.11 illustrates the operational principle of this source. The main component of this system is a heated filament that emits electrons. By ionizing the electrons at i.e. 70 eV, they acquire a wavelength of 1.4 Å, which is similar to the length of a C-C bond.

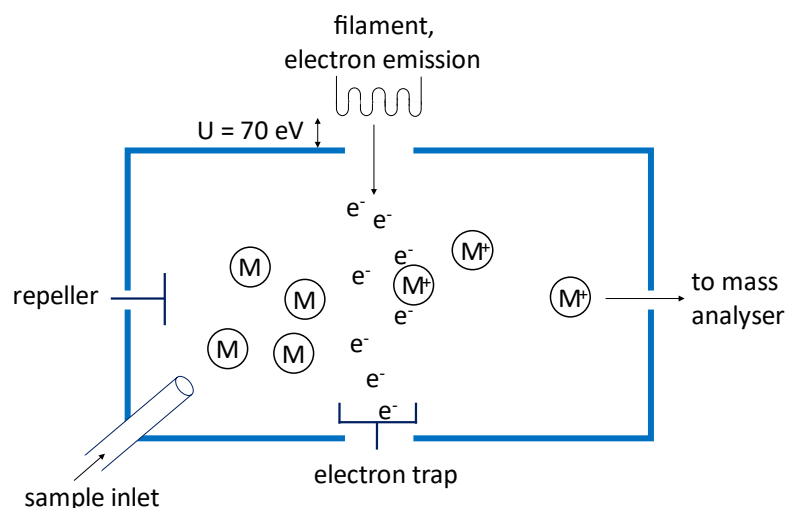


Figure 2.11 Schematic working principle of an electron ionization source (Hoffmann 2013).

The electrons collide with gaseous molecules of the injected sample to form positive ions with an odd electron number: $M + e^- \rightarrow M^{+\cdot} + 2e^-$. The resulting ionized radical cations exit the source and enter the mass analyser. Neutral fragments are removed by the vacuum before exiting the source. Electron ionization with an ionization energy of 70 eV is applied to preserve replicable fragments that can be compared with a database. Two different mass analyzers were used in this study and are described in detail. The ion trap analyzer with a nominal-mass resolution was employed, as well as the Orbitrap mass analyzer with a high resolution.

The Paul Ion Trap is a device composed of two opposing end electrodes (anode) surrounding a ring-shaped electrode (cathode), as shown in Figure 2.12. A three-dimensional high-frequency field is utilized to trap ions in two or three dimensions, enabling their 'storage'. (E. de Hoffmann & Stroobant, 2007). The use of helium as a damping gas reduces the kinetic energy of the ions, resulting in their concentration in the center of the trap. This enables higher resolution and prevents ion loss (E. de Hoffmann & Stroobant, 2007). The high-voltage field produces a time-varying potential and alternating focusing on the r and z directions. The Mathieu equations describe the associated frequencies and voltages, determining whether an ion can remain a stable trajectory in the ionic field. By applying a specific alternating voltage, the respective

orbit of the selected ion can be stabilized, while other ions with different m/z ratios collide with the wall of the ring electrode. This phenomenon is known as the mass-selective instability mode (Gross, 2013).

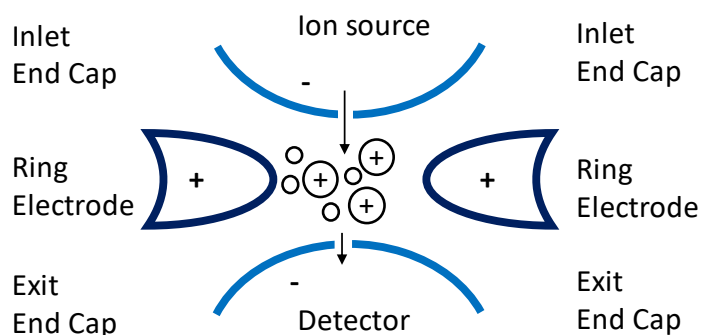


Figure 2.12 Scheme of a three-dimensional ion trap. Own drawing after (E. de Hoffmann & Stroobant, 2007).

The detector transforms the ion current, which is separated by m/z ratio, into an electrically measurable signal. It comprises a high-energy conversion dynode and an electron multiplier horn. The ions produced are initially converted to electrons by the dynode. The electrons are then transformed and accelerated to a multiplier dynode, where they knock out more electrons. This process is repeated to generate additional electrons, which are then collected on the electrode to create the detector signal (Gross, 2013; E. de Hoffmann & Stroobant, 2007).

The Orbitrap mass analyzer enables the acquisition of high-resolution mass spectra with a resolution of up to 60000 at an m/z ratio of 200 using a GC-Orbitrap-MS (Fisher Scientific, 2022). It achieves a mass accuracy of less than 3 ppm with external calibration and less than 1 ppm with internal calibration (Fisher Scientific, 2022). It covers a mass range of m/z ratio 30 to 3000. The Orbitrap mass analyzer, developed by (Scigelova & Makarov, 2006), is exclusively available from Thermo Fisher Inc. Together with the Fourier-transform ion cyclotron resonance (FTICR) mass spectrometer, it is based on the image current technique, which determines the mass-to-charge ratio by the oscillation frequency of the respective ions. The resulting transient signal is converted using Fourier transforms to generate a mass spectrum. However, it should be noted that the FTICR-MS is more expensive and has more space requirements than the Orbitrap mass analyzer (Hu et al., 2005). The design and ion path of the GC-Orbitrap Exploris mass analyzer used in this study is shown in Figure 2.13. The device produces analyte ions in the ion source through ionization by electron ionization (EI) under vacuum. The ions then pass through the Bent flatapole, which acts as an ion transmission device. The flatapole's bent shape prevents neutral particles from following the ion path (Fisher Scientific, 2022).

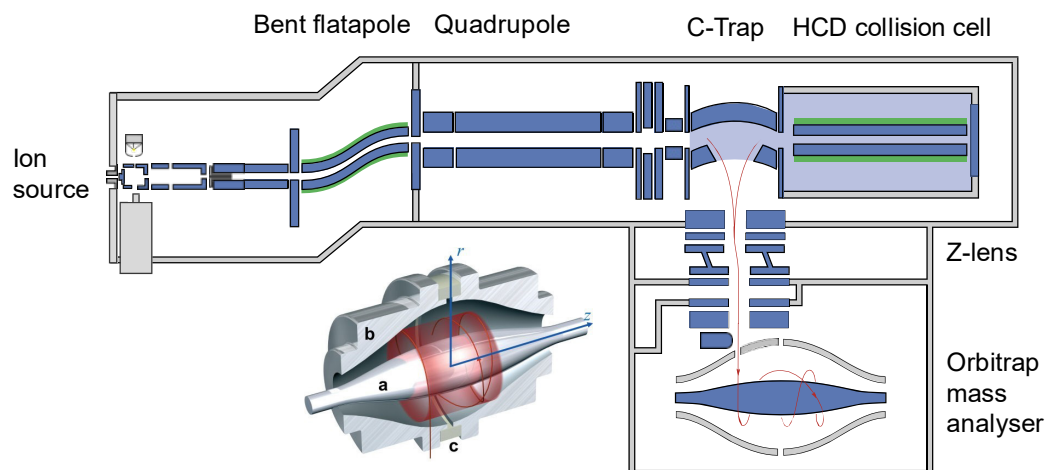


Figure 2.13 Scheme of the Orbitrap Exploris GC mass spectrometer ion path. Adapted from the operating manual of the instrument (Fisher Scientific, 2022). Schematic drawing of an Orbitrap analyzer (Scigelova & Makarov, 2006).

An RF voltage with a common mode DC offset is applied to ensure efficient ion transport and neutral particle separation. An axial DC gradient is added to the bent flatapole to facilitate rapid transport (Fisher Scientific, 2022). The ions are directed to the quadrupole mass analyzer where precursor ion selection takes place. The quadrupole rod functions as an ion transmission device, filtering the transmitted ions based on their m/z ratio through the application of RF and DC voltages. The ions subsequently enter the gas-filled curved linear trap (C-trap). The ions lose their kinetic energy by colliding with nitrogen, which acts as a trapping gas, and are then collected in the central section. Nitrogen also serves to cool the ions. This work does not include further fragmentation of selected mass-to-charge ratios for MS₂ experiments using a higher-energy collisional dissociation chamber (HCD), but it is possible. Following fragmentation, the ions are directed to the Orbitrap mass analyzer. The analyzer's central electrode has a spindle shape and is flanked by a pair of ring-shaped electrodes, as illustrated in Figure 2.13. The Orbitrap analyzer captures and confines ions by applying an electric field. The ions begin to oscillate around the inner electrode on stable trajectories, with the attraction of the inner electrode being in equilibrium with the opposing centrifugal force. Figure 2.13 illustrates the movement of ions along the z -axis. The movement is harmonic and independent of kinetic energy. The frequency ω , which can be precisely measured, is the only dependent variable and varies based on the m/z ratio.

$$\omega = \sqrt{\left(\frac{z}{m}\right)k} \quad (2.1)$$

Here, z represents the cylindrical coordinate and k represents an instrumental constant. The oscillating ions produce a broadband current, which is measured and converted by a Fourier Transformation to determine the individual frequencies and intensities resulting the mass spectrum (Fisher Scientific, 2022; Hu et al., 2005).

The mass resolution R is defined as the minimum difference between two m/z ratios that can be resolved. It is relevant to characterize different analytes of similar, isobaric compounds. The International Union of Pure and Applied Chemistry (IUPAC) recommends two definitions for this purpose. The first is the '10 % valley definition', which states that two singly charged ion signals of the same height in a mass spectrum with masses M and $(M-\Delta M)$ are separated by a valley that corresponds to 10 % of the height of the peaks at the lowest point. The second definition is based on the full width at half maximum (FWHM) and is an index of mass resolution (Hart-Smith & Blanksby, 2011). The equation for calculating R is:

$$R = \frac{M}{\Delta M} \quad (2.2)$$

2.4 Techniques for aerosol characterization

Various devices are required to measure the numerous properties of aerosols. The following two sections will explain the instruments used for this purpose and their operation. The concentration and size distribution of particles were measured to draw conclusions about the ongoing reaction and to provide a more detailed explanation of the substances' behavior. The aerosol particles were chemically characterized using TD-GC-MS. The instruments' working principle was explained in chapter 2.3. The results of the experiments will be discussed in chapter 4.4.

2.4.1 The measurement of particle concentrations

Particle concentration can be measured either offline or online. An offline method that is often used involves collecting aerosol particles on a suitable substrate, such as a filter. The concentration can be determined by weighing the filter and performing calculations (Kulkarni et al., 2011). However, this method is time-consuming and cannot be used to measure rapid changes in particle concentration. Furthermore, the particle concentrations obtained were averaged over the entire sampling period (Kulkarni et al., 2011). To mitigate these drawbacks, online methods can be used to measure aerosol particles. The improved time resolution of online methods enables the investigation of near real-time events that occur within a few seconds to a few minutes (Kulkarni et al., 2011).

One instrument used for online measurements is an optical particle counter (OPC). It measures the size and number concentration of the aerosol particles by means of light scattering on individual particles. The aerosol is exposed to a condensed light beam, which is then scattered by the particles. The scattered light is received by a photodetector and converted into an electrical pulse. The concentration of particles is determined by measuring the pulse counting speed and particle size based on the pulse height. Substituting the white illumination source with a coherent and monochromatic laser light presents numerous possibilities for applications. For example, it could facilitate the creation of a portable, battery-operated counter that employs a laser diode as the light source (Sorensen, Gebhart, O'Hern, & Rader, 2011).

Another well-established instrument that is more suitable for measuring the properties of smaller particles is the condensation particle counter (CPC). This instrument counts selected particles to measure the particle concentration of the aerosol. CPCs can detect ultrafine or nanoparticles with a diameter of less than 100 nm. Unlike using only an OPC, the particles are first enlarged by condensation. Optical scattering cannot detect particles in the nanometer range. To enable optical particle counting, the particles are enlarged through nucleus condensation. A CPC operates by passing the aerosol sample through a heated saturator enriched with either butanol or water. The aerosol is then cooled in the condenser, causing supersaturated vapor to condense on the particles,

which act as condensation nuclei. Finally, the enlarged particles are detected via optical light scattering. (Y.-S. Cheng, 2011).

There are three basic techniques for achieving the condensation or supersaturation process: adiabatic expansion, thermal diffusion and mixing of hot and cold airstreams. These techniques allow for a wide range of applications for a CPC, including investigating new particle formation, controlling indoor radon progeny or cleanrooms, and measuring the size of sub-micrometer aerosols. The first CPC was built by Aitken in 1888 and was an expansion-type CPC. Following him, particles with sizes between 0.02 and 0.2 μm are commonly known as 'Aitken nuclei'. He created a CPC to quantify the number of particles above 0.02 μm , which are not visible to the naked eye. The aerosol is first saturated with water vapor at room temperature and then cooled through either volume expansion or pressure relief to achieve supersaturation. This phenomenon occurs when the concentration of a solution surpasses its saturation vapor pressure, resulting in the formation of particles. These particles then grow, leading to the creation of droplets (Seinfeld & Pandis, 2006).

If the particles are larger than 1 μm , they can be counted using a magnifying glass. Nowadays, they are detected using photoelectrical means. This process is repeated in cycles, which means that this type of CPC cannot be combined with a diffusion battery or a differential mobility analyzer (DMA), which require a steady-state flow type of CPC (Kulkarni et al., 2011). The latter and the tandem operation will be explained in the next section.

Continuous flow CPCs, such as diffusion batteries and scanning mobility particle analyzers (SMPS), work by diffusing water vapor to the walls of the condenser more rapidly than the flow cools. This results in a depletion of water vapor. Different working fluids for thermal diffusion CPCs are established. For instance, when using alcohol such as n-butanol, the principle of conductive cooling is applied. Figure 2.14 illustrates the working principle of such CPCs.

Initially, the introduced aerosol stream passes through a heated isolated chamber, which saturates its gas phase with the fluid. In the second step, the aerosol is cooled in the condenser to 10 °C (Kulkarni et al., 2011). Finally, the particles are measured by means of light scattering. If the thermal diffusion CPC uses water as the working fluid, it works as a water-condensation particle counter (WCPC). Figure 2.15 shows the working principle of the WCPC. The system comprises three subsystems: the sensor, the microprocessor, and the signal-processing electronics. The sensor is the core of the system and consists of the conditioner, initiator, moderator, and optical detector. The conditioner, initiator, and moderator together form the growth tube, where aerosol particles flow through a wet-walled tube and grow to a detectable size. The aerosol

initially passes through the inlet into the conditioner area, where it is either cooled or heated depending on the set mode (cooled for 2 nm mode and heated for 7 nm mode).

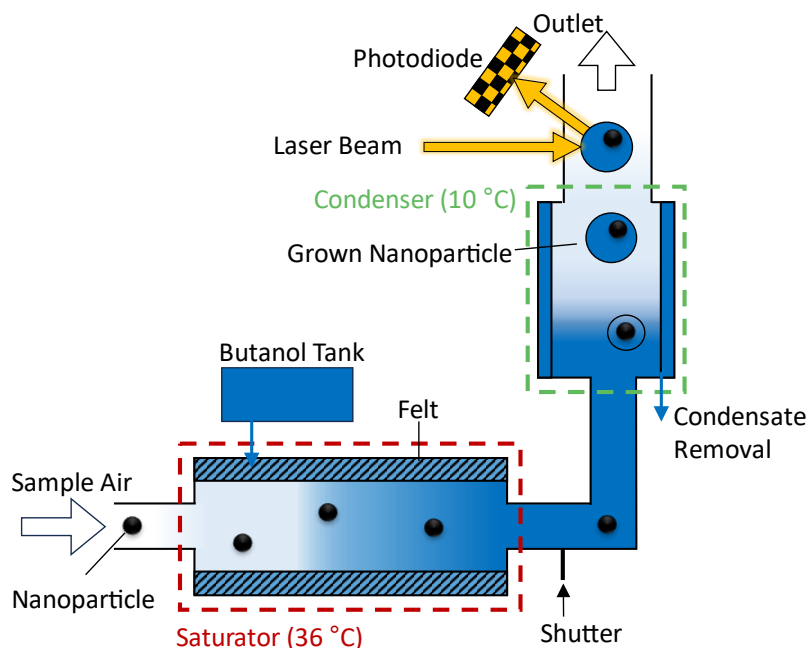


Figure 2.14 A CPC for butanol was drawn based on Spielvogel, 2009.

The aerosol flow is saturated with water and brought to a specific temperature and humidity before reaching the initiator. The initiator has heated walls where water is injected.

The water vapor resulting from this process diffuses into the colder aerosol flow, leading to supersaturation conditions that cause condensation onto the particles. This condensation continues in the cold-walled moderator until the particles become large enough to be detected optically. Condensed water is removed from the moderator through a porous wick, either by absorption or by a pump at the bottom of the wick. The optical detector is composed of a laser diode, a collimating lens, a cylindrical lens, collection lenses, and a photodiode. (TSI Incorporated, 2019).

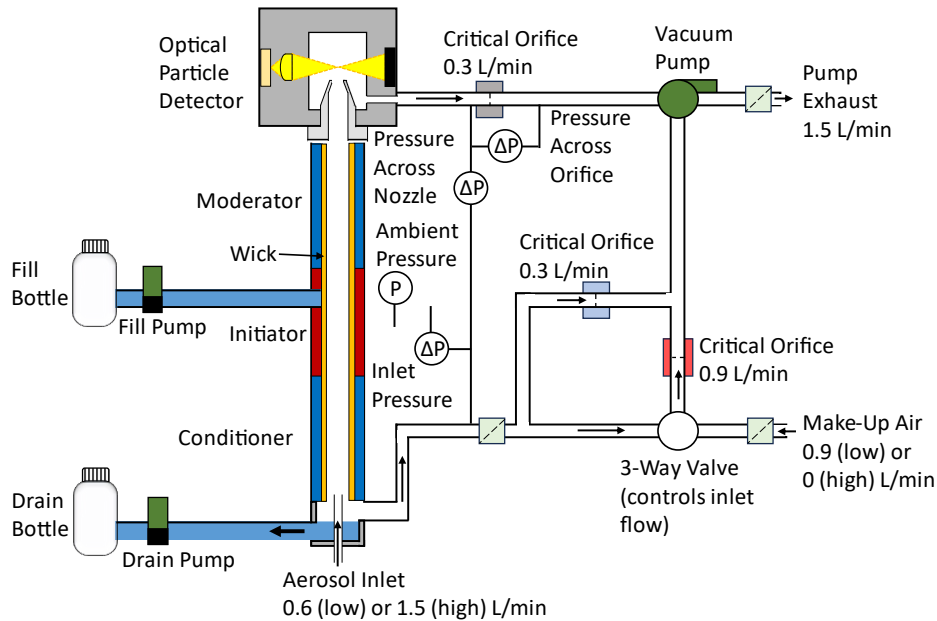


Figure 2.15 The WCPC used in this study is illustrated, adapted from the operation manual of the water-based condensation particle counter model 3789 (TSI Incorporated, 2019).

The third type of CPC involves mixing streams of different temperatures to achieve supersaturation, so-called mixing-type CPCs. In this case, both flows can be saturated aerosol flows. These CPCs consist of a saturator with a reservoir for the working fluid, a mixing chamber, and a subsequent detector. By using the initial temperatures and flow velocities of the two air streams, the temperature and vapor concentration can be determined. Compared to the second thermal diffusion type CPC, the mixing-type CPC responds faster and loses fewer aerosol particles by diffusion. This is because the aerosol does not have to pass through the saturator, resulting in a shorter distance of transport (Y.-S. Cheng, 2011; Kousaka, Niida, Okuyama, & Tanaka, 1982). Although several types of CPCs are constantly being developed, the main drawbacks of the currently available ones are their response time, minimum detection limit, and diffusion losses of small particles (Y.-S. Cheng, 2011).

2.4.2 The measurement of aerosol particle size distributions

The size or size distribution of aerosol particles is the most important property, in addition to their concentration. The differential mobility analyzer (DMA) is the standard instrument used to measure aerosol particles in the submicron size range. It was first introduced by Knutson and Whitby in 1975 to produce monodisperse submicrometre particles, which were then used to calibrate other instruments. The DMA classifies particles based on their electrical mobility, which is determined by their size and charge state. The voltage applied to the DMA determines the electrical mobility of the particles

that pass through it at a given time. Diverse designs of DMAs have been developed depending on the size range of the particles being investigated. For instance, Reischl and colleagues (Winklmayr, Reischl, Lindner, & Berner, 1991) developed the Vienna DMA, which is optimized for analyzing particles in the low-nanometer size range.

The Nano DMA was developed to investigate even smaller particles. Figure 2.16 shows a scheme of a Nano DMA and its flows used in this work. The Nano DMA is a modification of the Long or Vienna type DMA, optimized for particles less than 20 nm in size, and provides a size range from 2 to 150 nm. The polydisperse aerosol enters the DMA from the top and flows parallel to a laminar, particle-free gas stream called sheath air downwards to two cylindrical rods. A high voltage is applied to the inner electrode, creating an electric field that transports particles. Positive particles are transported to the inner electrode, negative particles to the outer electrode, and neutral particles to the sheath gas exit. To achieve a higher flow and minimize diffusion losses of nanometer-sized particles, a bypass flow can be used (Baron, Mazumder, Cheng, Peters, & Willeke, 2011; Flagan, 2011; Fuchs, 1963; Hinds, 1999; Sorensen et al., 2011; Wiedensohler, 1988).

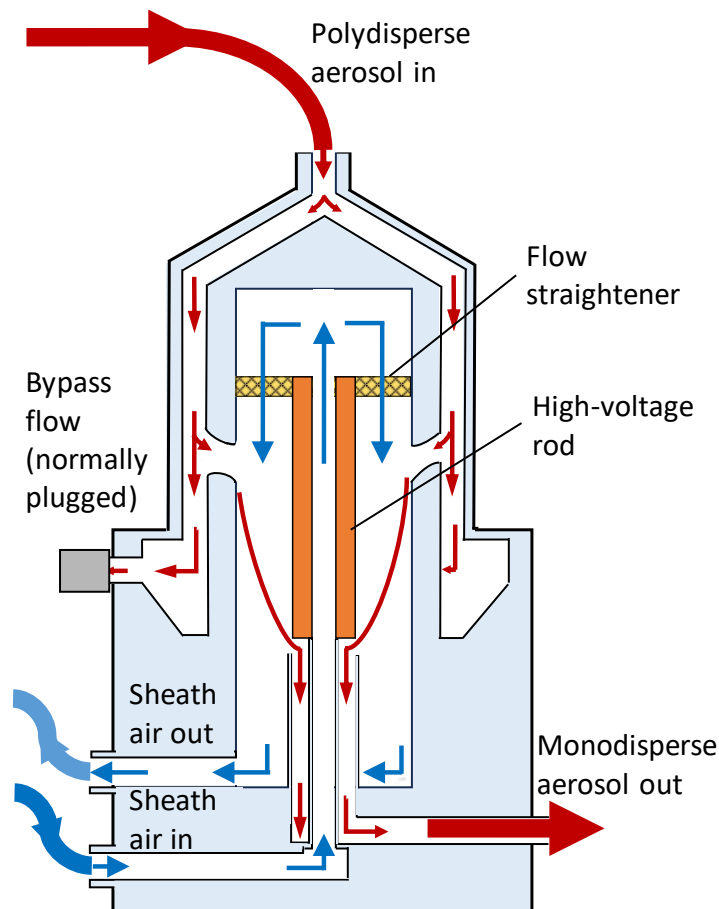


Figure 2.16 The illustration of the Nano DMA from TSI has been adapted from the operation and service manual of TSI (TSI Incorporated, 2016).

Additionally, a charger is connected in front of the DMA to achieve charge equilibrium on particles. The aerosol neutralizer or bipolar diffusion charger is applied to provide a known charge distribution on the aerosol entering the DMA by giving the particles either a positive, negative or zero charge. This occurs when the aerosol frequently collides with bipolar ions, resulting in a rapid equilibrium charge state (Wiedensohler, 1988).

The used TSI device uses a neutralizer based on a Kr^{85} source that emits beta rays. The source used in the GRIMM device contains Am^{241} , which emits alpha rays. Figure 2.17 illustrates the function of the alpha rays: they first ionize the air, which in turn charges the particles that then enter the DMA. On the right-hand side of Figure 2.17, the construction of the DMA and the inner coating of the source are shown.

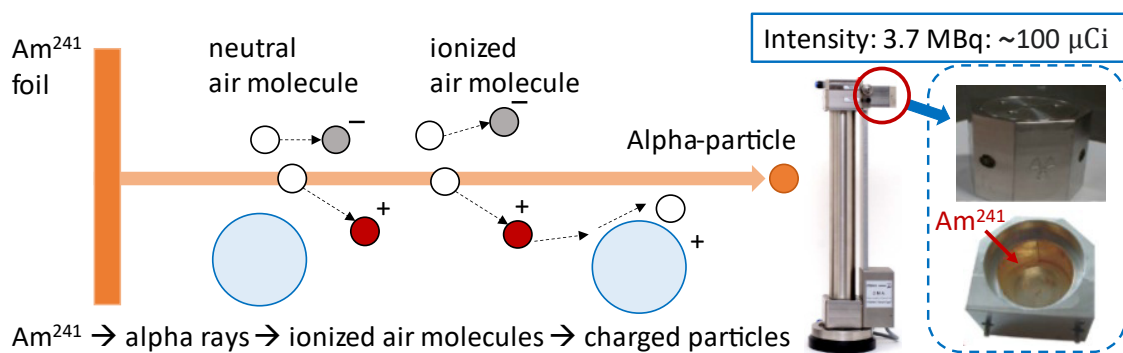


Figure 2.17 This is an exemplary working example of an aerosol neutralizer that is based on an Am^{241} source. The Am^{241} is an alpha emitter that ionizes the air molecules. The resulting positive charge changes the particles, allowing them to be classified electrostatically by the DMA. The source uses an intensity of 3.7 MBq, which is approximately 100 μCi . The picture and drawing have been adapted from Spielvogel, 2009.

The electrostatic classifier can be combined with a CPC to operate in SMPS mode, as illustrated in Figure 2.18 as a single instrument to produce a rather monodisperse aerosol conducting further experiments.

In this work the electrostatic classifier is combined with a CPC to a SMPS often called TDMA to investigate the basic properties and behavior of particles of a certain size.

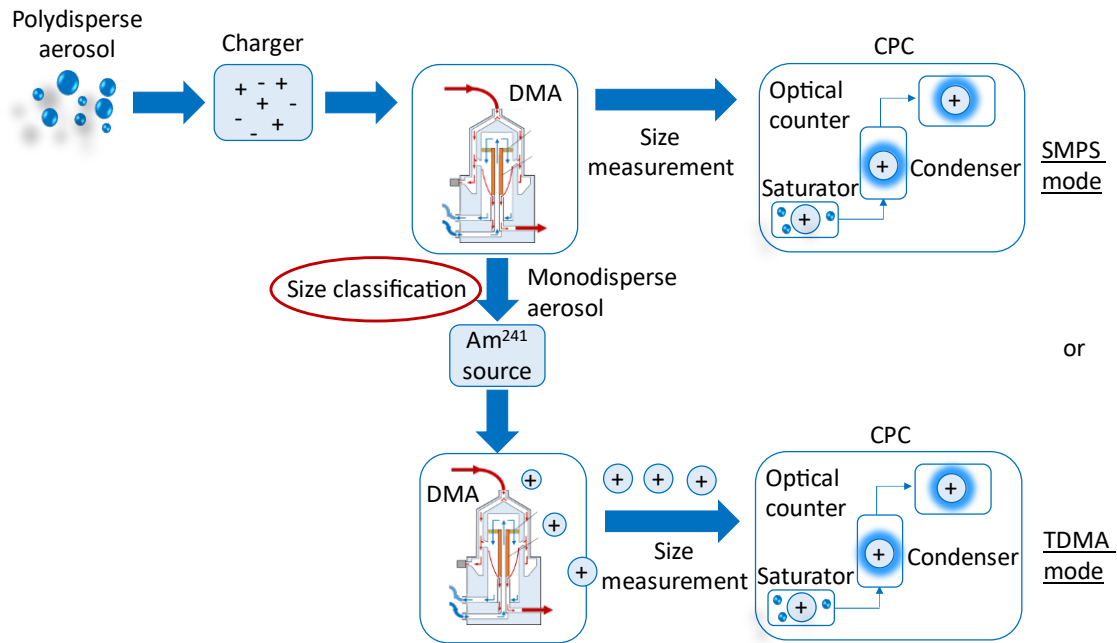


Figure 2.18 Schematic of the TDMA setup. The diagram was created based on TSI Incorporated, (2016) and Joutsensaari et al., (2001).

3 Thesis objectives and outline

The aim and basis of this work was to investigate chemical reactions, that are dependent of particle size and to detect them using TD-GC-MS. The first part focused on the question of whether nanometer-sized particles can function as nanoreactors for reactions within aerosol particles and examined the influence of particle size and pressure within the particle. The objective was to understand these processes by finding out how new aerosol particles form and grow. The purpose of this investigation is to examine the basics of aerosol formation to gain a better understanding of the atmosphere's composition and its impact on global climate change. Nanometer-sized aerosol particles grow through nucleation and accumulation of organic molecules, affecting cloud droplet formation. It has not yet been sufficiently researched how exactly this happens and what influences are involved. The physical and chemical properties of gas-aerosol particle reactions in laboratory experiments are the focus of this work. The first step was to create an experimental setup that generates a monodisperse organic aerosol with a size of less than 100 nm.

This aerosol should then react with a gas phase in a flow tube reactor that is specially designed for this purpose. The gas phase should consist of molecules that are capable of reacting with the aerosol. The changing size of the aerosol particles indicated that a reaction occurred. The Diels-Alder reaction, which is an organic reaction between a dienophile and a diene, was chosen as the model system. The selection criterion for choosing this reaction was its high reactivity, but also the fact that this reaction prefers to take place under high pressure. As Laplace's theory states, there is a higher internal pressure in smaller particles than in larger ones. In addition, bond-forming chemical reactions are favored by higher pressure, making them more important in nanometer-sized aerosol particles. Two different types of SMPS systems were used to select the particle size for the subsequent size-dependent analysis of the reaction with a focus on reaction kinetics. A TD-GC-MS method was developed for qualitative chemical analysis.

Semi-volatile compounds are formed during the Diels-Alder reaction. . The TD-GC-MS measurements, which were conducted using an in-house developed TD injector, only partially measured these compounds. This partial measurement was due to the temperature in the focusing trap being too low, resulting in carryovers. However, precise monitoring and control of the temperature was not possible. The objective of

the second part of this work was to enhance the in-house TD injector, which has undergone several generations of development by PhD students, to enable injection of semi-volatile compounds without carryover. A new heater for the focusing trap was developed and the software for controlling and monitoring the TD process was adapted by setting a higher temperature for the focusing trap. Rather than the issue of carryover, other problems with the in-house TD injector have now become prominent. High background signals resulting from contamination caused by the abrasion of screw connections have led to restrictions. The resulting frequent maintenance due to blockages in the injector often leads to prolonged leak detection. The system's complexity, with its wide variety of components, made leak detection more challenging. The question arose as to how to redesign the complex TD injector structure to deliver the most reliable and robust results possible, while also being easy to maintain. Additionally, the injection process should be designed with flexibility for future use.

A new TD injector with a versatile design has been developed and built. The TD injector features a desorption direction from bottom to top. It was built for manual operation and has a higher maximum temperature of the focusing trap. The TD injector has a curved and flexible structure with only two screw connections at leakage-prone points. The question was raised whether the versatile TD injector can inject a low concentration of gas phase into a GC-Orbitrap-MS with minimal background noise and at the target maximum temperature of the focusing trap. The aim of this study was to investigate the analysis of aerosol particles or gas traces in the atmosphere and to improve the identification and quantification of organic analytes with varying levels of volatility.

In the third part of this work, the application in chemical ecology was used to test whether the developed versatile TD injector fulfills the set goals in the development process. As an application for the built versatile TD, the research question was whether living ants and their brood emit a volatile gas phase. The background to this is the analysis of their chemical communication via their gas phase. Up to now, hexane extracts from ants have been used to investigate chemical communication. The disadvantage of this is that the ants are no longer alive during sampling, which means that the volatile substances in the gas phase cannot be analyzed. The question was how to sample the adsorption tube with the emitted gas phase of the living ants and their brood. A device made of glass was developed with the objective of minimizing external contamination when introducing the gas phase into the adsorption tube. After sampling, the analysis was carried out with the versatile TD injector. Once it was clear that molecules were being emitted, further experiments were carried out and analytes were identified and determined using a non-target screening approach.

4 Chemistry in nanometer aerosol particles: Flow tube experiments with Diels-Alder reactions as model system

This chapter is a reprint of the manuscript

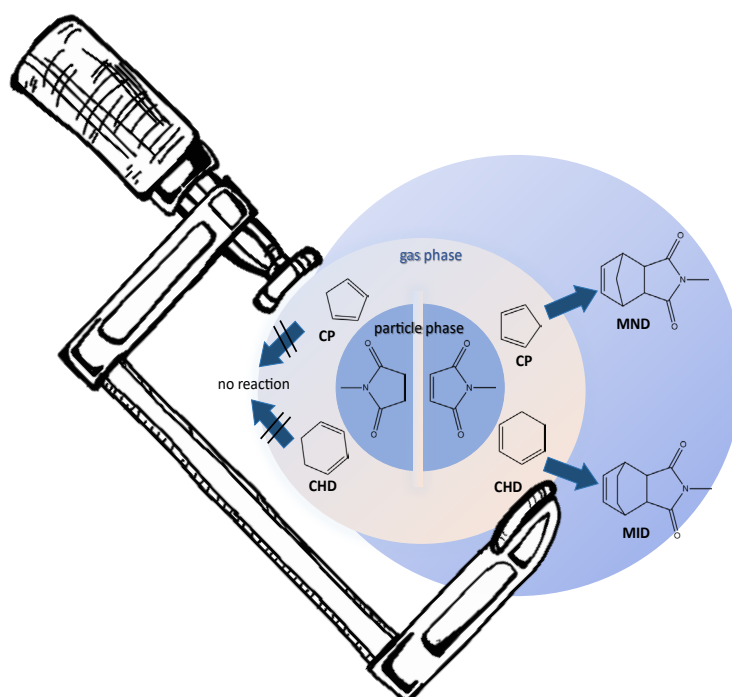
Chemistry in nanometer aerosol particles: Flow tube experiments with Diels-Alder reactions as model systems

Daniela Kleinsimlinghaus¹, Thorsten Hoffmann¹

¹Department of Chemistry, Johannes Gutenberg-University, Duesbergweg 10-14, Mainz, 55128, Germany

Correspondence to: T. Hoffmann (hoffmant@uni-mainz.de)

in preparation for Environmental Science: Atmospheres



Abstract Understanding the chemistry and behavior of molecules in nanometer aerosol particles observed in laboratory experiments can help to predict the properties of nanometer aerosol particles in the atmosphere and possible ongoing reactions. The Diels-Alder reaction, a well-studied reaction in organic chemistry used here as a model system. This reaction is known that higher pressure promotes bond-forming reactions. This offers the opportunity to study a pressure-sensitive chemical system behavior in nanometer-sized aerosol particles. The dienophile and dienes were selected for the reaction based on their reactivity, volatility, and detectability in the aerosol and gas phases, respectively. The observation of particle growth was indicative of whether a reaction had taken place. The growth factors of monodisperse aerosol particles with diameters of 30, 60, and 90 nm were determined for two reaction systems. The experimental determination of the reaction rate and reaction rate constants was carried out to investigate the influence of pressure, as related to particle size, on the reaction rate and reaction rate constants and compared with literature values. The analysis was conducted by Scanning Mobility Particle Sizer Systems (SMPS) and characterization of the reaction products was done via TD coupled to a gas chromatograph mass spectrometer system (TD-GC-MS).

Topics Aerosols, climate drivers, laboratory measurements, multiphase chemistry

Keywords Diels-Alder reactions, aerosol particles, pressure, climate change, growth, size-dependent, reaction rate constant

Environmental Significance The prediction of properties and behaviors of nanometer aerosol particles in the atmosphere based on laboratory experiments indicates a deeper understanding of aerosol formation and transformation processes in natural environments. Laboratory experiments investigating new particle formation in the nanometer range aim to develop fundamental knowledge. The growth of particles can be induced by reactions caused by the volatility, pressure, and chemical structure of the molecule. New particle formation affects the climate by influencing cloud condensation concentrations and can lead to haze formation, which has negative impacts on the environment and human health.

4.1 Introduction

To predict the atmospheric composition, understand global climate change and prevent health risks, knowledge about the formation of new particles and their growth is increasingly important. Particles which favor the condensation of water and grow cloud droplets under atmospheric conditions are named cloud condensation nuclei (CCN) (Rissman et al., 2007). The source for CCNs is known to be either new particle formation or nucleation (M. Kulmala et al., 2014). Early steps of particle formation and growth are

vapor uptake, either by phase transitions, chemical reactions, or molecular transport (Riipinen et al., 2012). If chemical reactions are involved, organic molecules are major contributors in this growth phase (Kirkby et al., 2016). They can either grow further through condensation or may be lost by coagulation with larger particles (Patoulias et al., 2015). Size-resolved composition measurements with mass spectrometers indicate that nitrogen-containing organic compounds are important players in the growth of nanoparticles in the size-range of 10 to 30 nm. (J. N. Smith et al., 2008). However, the particle embryos themselves offer a unique nanoscale chemical environment due their size dependent physical properties (Petrosko et al., 2016). To thermodynamically describe the environment of liquids with strongly curved interfaces such as aerosol nanoparticles, the Laplace pressure has to be considered. (Liu & Cao, 2016; Marcolli, 2020; Sarah S. Petters, 2022). The Young-Laplace equation describes the pressure difference between the inside and outside of a droplet resulting from intermolecular forces and the interfacial curvature of nanoparticles (Adamson & Gast, 1997; Laplace, 1829; Riva et al., 2021; Young, Peacock, & Leitch, 1855). Furthermore, the surface tension raises the vapor pressure over a curved interface. This so-called Kelvin effect is described by the Kelvin equation for pure liquids. The vapor pressure of a liquid arises from the energy necessary to separate a molecule from the attractive forces exerted by its neighbors and bring it to the gas phase. For nanometer sized particles, the vapor pressure increases with decreasing radius of the particle. The Köhler theory extends this effect to mixtures (Köhler, 1936), by combining the Kelvin effect and Raoult's law (Seinfeld & Pandis, 2006).

Riva et al. (2021), found that small particles in a nanometer size range have a higher internal pressure and suggested this as a characteristic condition on the effects on the growth of atmospheric aerosols. Furthermore, they stated that bond-forming chemical reactions are favored at higher pressures, gaining importance in the smallest particles. Therefore, particle size-dependent chemical reactions could play a crucial role in the life cycle of atmospheric aerosols. Diels-Alder (DA) reactions seem suitable as a chemical reaction system in aerosol nanometer particles. These reactions are known to be accelerated under high pressure due their large negative volume of activation (ΔV^\ddagger) through their transition state (Rudi van. Eldik & Klärner, 2002; Grosch et al., 2004b).

The goal of these laboratory flow tube experiments is to improve our understanding of the formation and growth of particles in the nanometer size range, focusing on the chemical reactions taking place. Particle growth is driven by organic molecules; growth reactions by addition of ubiquitous smaller organic molecular units, e.g., oligomerization, are a plausible mechanism, as nanometer particle embryos have special chemical and physical properties (Huang et al., 2022). Firstly, the increased internal pressure caused by surface tension called Laplace pressure increases with decreasing radius of the particle. Secondly, the increasing vapor pressure of the components in the

aerosol particle known as Kelvin effect. Both effects and the knowledge of the acceleration of bond-forming reactions due to negative reaction and activation volumes caused by shorter atomic distances of covalently bonded molecules (Riva et al., 2021) could potentially provide insights into the growth rate of newly formed particles and whether they can act as nanoreactors.

In this paper, we describe the construction of a flow tube reactor combined with a tandem differential mobility analyzer (TDMA) and present the first experimental results on DA reactions this system. This offers a pressure-sensitive chemical system that we explored with different suitable dienes and dienophiles. Dienophiles were introduced as the particle phase and dienes in the gas phase.

4.2 Theory

4.2.1 Growth of aerosol particles

In this section, we describe the theory of growth of the aerosol particles. Butt et al., 2006 described the property of an increased internal pressure for nanometer particles called Laplace Pressure. It is induced via surface tension. This offers the ability to perform pressure dependent reactions with particularly small (30 to 90 nm) sized aerosol nanometer particles.

4.2.2 Diels-Alder reactions

This reaction is a well-studied reaction in organic chemistry describing a [4+2] cycloaddition between a conjugated diene and a dienophile (Brückner, 2002a) as shown in Figure 4.1.

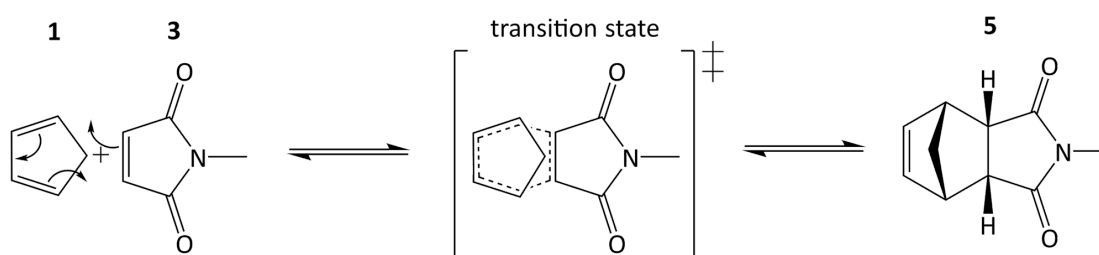


Figure 4.1 Reaction scheme of the Diels-Alder reaction with proposed transition state. The electron-rich diene cyclopentadiene **1** reacts in a concerted step with the electrophilic dienophile N-methylmaleimide **3** via a transition state to the product N-methyl-5-norbornene-2,3-dicarboximide **5**.

It is known that high pressure accelerates this bond forming reaction (Grosch et al., 2004b; Jenner, 1975). The activation volume of the DA-reaction product shows a relatively large negative reaction volume ΔV^\ddagger by favoring the kinetic endo

diastereoisomeric product (Clayden et al., 2012; Grosch et al., 2004a). The reason for this is a bonding interaction between the carbonyl groups of the dienophile and the developing π -bond at the back of the diene (Clayden et al., 2012).

The reactants displayed in Figure 4.2 were chosen based on various aspects, including the restraints of the experimental set-up. As one reactant needs to be in the gas phase, cyclopentadiene **1** and 1,3-cyclohexadiene **2** were chosen due their volatility and reactivity (Meyer & Hotz, 1973). The other reactant should be present in the aerosol phase and should react with the gas phase reactant as quickly as possible. However, the aerosol phase should not react with itself and should be reasonable stable. Therefore, N-methylmaleimide **3** was chosen because of its reactivity as a dienophile reported by Tang et al., (2012). In addition, the detectability of the reactants and the products with GC-MS is given. (Meijer et al., 1998; Tang et al., 2012).

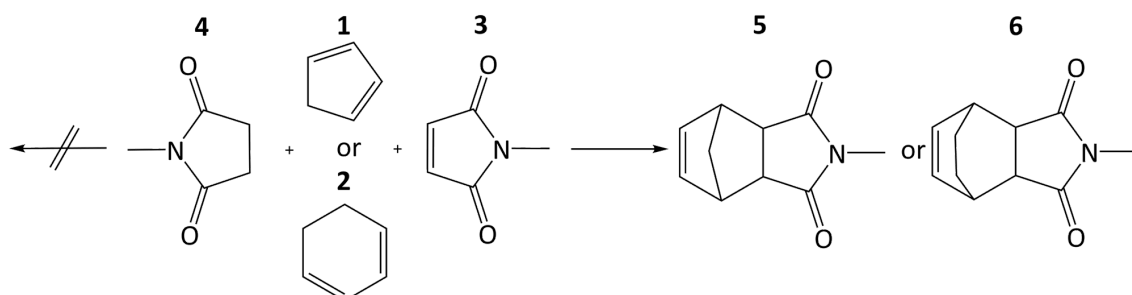


Figure 4.2 Diels-Alder-Reactions of used dienes cyclopentadiene **1**, 1,3-cyclohexadiene **2**, and dienophile N-methylmaleimide **3** with the nonreactive saturated educt N-methylsuccinimide **4** and the products N-methyl-5-norbornene-2,3-dicarboximide **5**, 3a,4,7,7a-tetrahydro-2-methyl-4,7-ethano-1H-isoindole-1,3(2H)-dione **6**.

4.3 Experimental

4.3.1 Setup of the reaction system

Figure 4.3 shows a schematic drawing of the experimental setup of the flow tube reaction system and the measurement system. The reaction of monodisperse aerosol particles with organic educts in the gas phase and measurement of particle size is similar to the organic tandem differential mobility analyzer (TDMA) of Joutsensaari et al. (2001). The major difference is that the size-classified aerosol is carried through a second educt instead of an organic solvent vapor followed by a flow tube reactor. In the experiments presented here the aerosol particles are produced by pumping educt solution (200 mg/L in methanol) to a pneumatic aerosol generator (TSI Model 3076 Constant Output Atomizer, TSI International Ltd.). It is then dried by an active charcoal denuder and guided to an electrostatic classifier (TSI 3082, TSI International Ltd.) to receive monodisperse aerosol particles with a certain size based on their electrical mobility. The

electrostatic classifier is equipped with a neutralizer (TSI 3088, TSI International Ltd.) and a nano-DMA (DMA-1, TSI International Ltd.).

An aerosol flow of 0.2 L min^{-1} was achieved using nitrogen as the aerosol gas medium. A sheath flow of 2 L min^{-1} was applied in the DMA-1 (aerosol – sheath flow ratio 1:10). The flows were controlled by the electrostatic classifier critical orifices. Primary aerosol particles with the diameter of either 30, 60 or 90 nm were produced and used in the experiments. In parallel, the other educt was brought into the gas phase. For that purpose, either a distillation or an evaporation of the educt was carried out. The gaseous educt was passed to the flow tube with a nitrogen flow of 0.015 L min^{-1} meeting the particle phase educt. Immediately after the flow tube a scanning mobility particle sizer neutralized the aerosol (AM-241, radioactive α -source, Grimm Aerosol Technik GmbH) and characterized particle number concentration and particle size. The DMA-2 (5.500 GRIMM „Vienna Type“, U-DMA) was operated with an aerosol and sheath flow of 0.3 L min^{-1} and 3 L min^{-1} (aerosol – sheath flow ratio 1:10). The aerosol inlet flow and sheath flow were determined by the Scanning Mobility Particle Sizer (SMPS) (Grimm Model 5.416, Grimm Aerosol Technik GmbH).

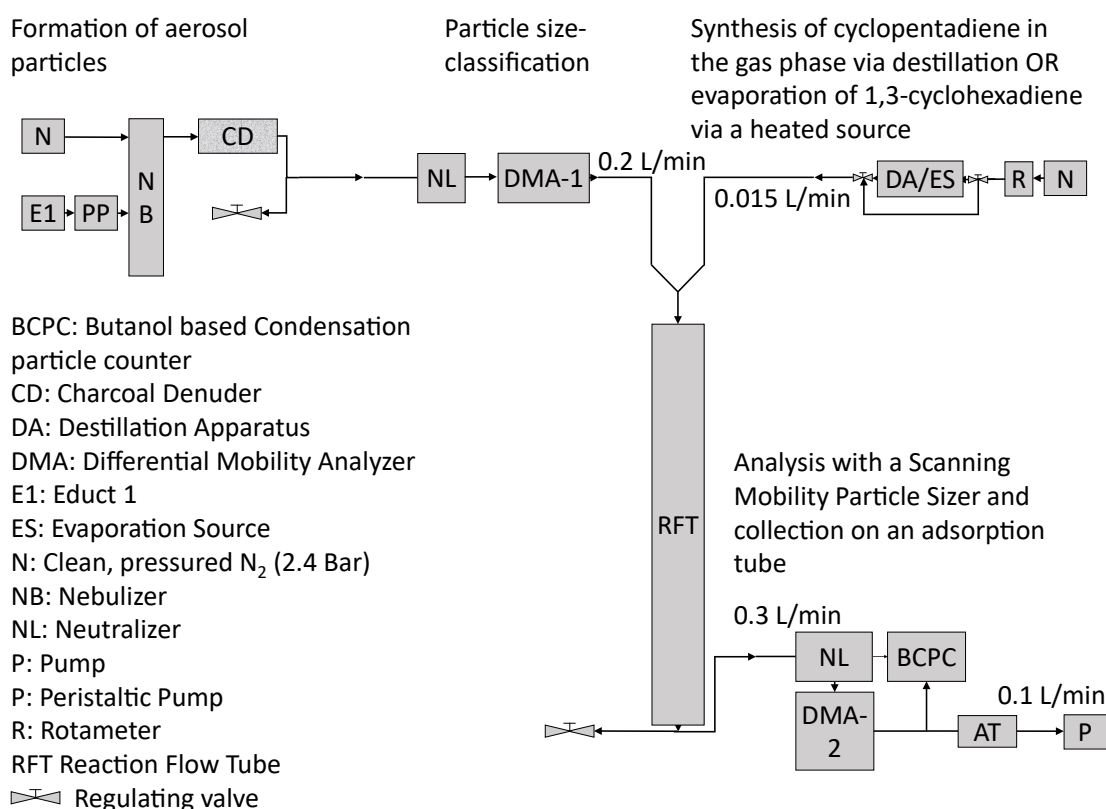


Figure 4.3 Schematic of experimental setup for flow tube reactions and measurement of particle size.

In order to produce monodisperse aerosol particles, ensure a constant source of molecules in the gas phase, supply an environment where they can react and provide a reliable and reproducible measurement system to observe this reaction a TDMA was chosen adapted from of Joutsensaari et al. To show the reliability of the set up several experiments were conducted. One advantage of this set-up is that the wall losses are negligible, as all calculations carried out are done with the measurements of the same SMPS system, which is the key factor of chosen this setup. Furthermore, there is no need to compare different SMPS systems.

To verify that a reaction has taken place the growth factors of the particles were determined. To calculate the growth factor, the experiment was first carried out without the addition of the educt in the gas phase measuring the particle size and then with the addition of the educt in the gas phase. The size of the aerosol particles measured in DMA-2 should be the size of the aerosol particles measured in DMA-1 if no reaction has taken place and increase if the reaction has taken place. The growth factor was calculated by evaluating the geometric number mean diameter of the size distribution of both experiments and divided product particle size through the educt particle size. Furthermore, the aerosol was collected on an adsorption tube for each step to be analyzed with a thermodesorption gas chromatograph-mass spectrometer (UNITY-xr, Markes International Ltd.).

4.3.2 Operation of the TD-GC-MS

The instrumentation consisted of a Markes TD injector (Unity-XR) coupled to an Thermo GC-MS (Trace GC 2000/PolarisQ) through a heated deactivated fused silica column (2 m length, 0.25 mm i.d.). The fused silica column is directly connected to a Rxi® 5MS column (Crossbond® 5 % diphenyl, 95% dimethyl-polysiloxane, 30 m × 0.25 mm i.d. × 0.25 µm film thickness, Restek Corp., PA, USA) via a press-fit fused silica connector (Restek). The carrier gas is controlled by a pneumatic gas controller (U-GAS01, Markes) set at 1 bar to measure in constant pressure mode.

The TD method consists of a two-step process: (1) Pre-desorption with a pre-purge of 3 min with a trap flow of 100 mLmin⁻¹ and desorption of sample at 280 °C for 15 min on a cooled trap at -30 °C at a trap flow of 50 mLmin⁻¹, (2) Trap Purge of 1 min with a flow of 20 mLmin⁻¹ and trap desorption at 320 °C for 5 min. The GC method started after a solvent delay of 2 min with a temperature of 50 °C, followed by a gradient of 25 °C min⁻¹ up to 180 °C held for 2 min, then 25 °C min⁻¹ up to 250 °C held for 3 min. A blank run of the same tube (same TD and GC-Method as for aerosol samples) was performed between samples to ensure the TD-GC-MS system was free of carryover from the previous measurement. Reconditioning of the tubes was achieved by heating for 15 min at 100 °C, 15 min at 200 °C, 15 min at 300 °C, 15 min at 330 °C. Data was acquired and processed using Xcalibur, version 4.1.31.9 (Thermo Fisher Scientific Inc.).

4.3.3 Materials and chemicals

Organic compounds were obtained from Sigma-Aldrich in the highest purity available as follows: N-methylmaleimide **3** (97%), N-methylsuccinimide **4** (99 %), dicyclopentadiene **1** (contains 0,05 % butyl hydroxytoluene as stabilizer), 1,3-cyclohexadiene **2** (contains 0,05 % butyl hydroxytoluene as stabilizer, 97 %), N-methyl-5-norbornene-2,3-dicarboximide **5**. Methanol (LC-MS grade, Thermo Fisher Scientific Inc.) was used as solvent. Products of DA reactions for qualitative evaluation and method development were synthesized after a green mechanochemical grinding approach of J. Agarwal et al. (Agarwal, Rani, & Peddinti, 2017). The dienophile was poured into a mortar and the diene was added (molar ratio 1:1). The mixture was mortared for approximately 3 minutes until a white solid was formed from the yellow solid. Inert-coated stainless steel sorbent tubes containing universal sorbents (Tenax TA, Carbograph 1TD, Carboxen 1000) were purchased from Markes International Ltd. and conditioned as recommended by Markes with a series of incremental temperature steps (100, 200, 300 and 330 °C for 15 min) prior to first use.

4.4 Results and discussion

An experimental setup with a flow tube reactor was developed to conduct chemical reactions in nanometer aerosol particles and to develop a model system. Diels-Alder reactions were as model reactions due to the suitable reaction conditions. Under normal conditions. In bulk, these reactions are accelerated with increased pressure. We hypothesize that conditions in nanometer aerosol particles are similar due to the increased internal pressure in nanometer aerosol particles. Nanometer aerosol particles containing dienophile N-methylmaleimide **3** or saturated educt N-methylsuccinimide **4** with sizes of 30, 60 or 90 nm were generated and guided through the flow tube reactor to react with cyclopentadiene **1** or 1,3-cyclohexadiene **2** in the gas phase. The educts were chosen based on their reactivity, volatility, and detectability. cyclopentadiene **1** and 1,3-cyclohexadiene **2** were chosen because they were expected to show different growth behavior based on their molecular structure and reaction rate. cyclopentadiene **1** is more reactive than the 1,3-cyclohexadiene **2**, therefore it was distilled in the reaction pathway and immediately introduced to the flow tube. The aerosol particles of the two different educts (N-methylmaleimide **3** and N-methylsuccinimide **4**) were investigated and compared regarding change in particle size and whether a reaction with the gas phase has taken place, which was analyzed via recorded mass spectra and verified via a bought (N-methyl-5-norbornene-2,3-dicarboximide **5**) or synthesized (3a,4,7,7a-tetrahydro-2-methyl-4,7-ethano-1H-isoindole-1,3(2H)-dione **6**) standard. Furthermore, the growth factors for the reactive dienophile and the nonreactive saturated educt N-methylsuccinimide **4** aerosol particles of three different starting diameters of aerosol particles were experimentally determined and compared to a

theoretical calculated growth factor. Furthermore, an experimental reaction rate constant was calculated for the investigated particle sizes. Then the reaction rate constants of the two reaction systems were compared with respect to the physical properties of cyclopentadiene **1** and 1,3-cyclohexadiene **2** but also the particle sizes. Finally, the determined reaction rate constants of the reactions taking place in the particle were compared with the reaction rate constants known from literature. Among other things, the influence of pressure was considered and discussed.

4.4.1 Effective pressure inside nanometer-sized particles

The Young-Laplace equation can be adapted to calculate the effective pressure inside nanometer sized particles by calculating the surface tension (γ) over an estimated curved liquid particle (Riva et al., 2021):

$$\Delta p = \frac{2\gamma}{r} \quad (4.1)$$

Here, r stands for the radius of the particle and Δp describes the pressure difference between the inside and the outside of the particle. Figure 4.4 illustrates the increase in Laplace pressure (Δp) particle size decreases. This is calculated from literature values for the surface tension of aqueous salts, including sodium chloride (Sarah Suda Petters & Petters, 2016; Su, Cheng, & Pöschl, 2020), water, organic compounds such as alpha pinene and oleic acid (Hritz, Raymond, & Dutcher, 2016; Korosi & Kováts, 1981; Sarah Suda Petters & Petters, 2016) and N-methylmaleimide **3** (ACD labs after Topping et al., 2007).

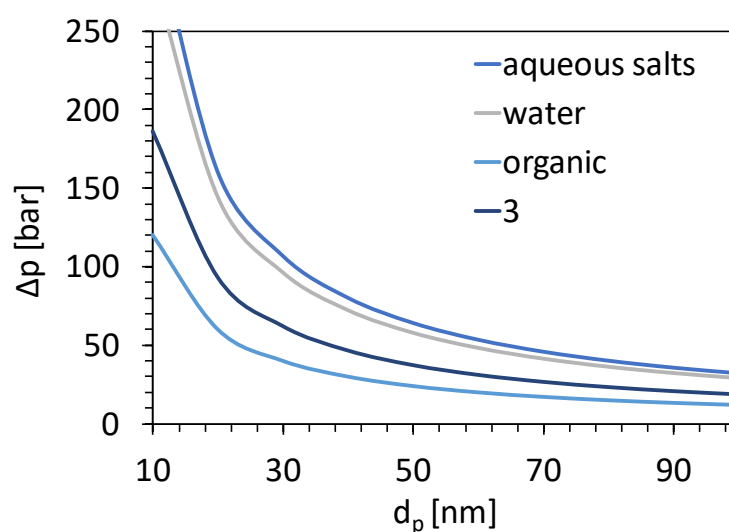


Figure 4.4 Calculated Laplace pressure at different particle diameter according Young-Laplace equation $\Delta p = 2\gamma/r$ assuming a liquid particle with the known surface tension γ for aqueous salts ($0.080 \text{ N}^{-3} \text{ m}^{-1}$), water ($0.072 \text{ N}^{-3} \text{ m}^{-1}$), organic ($0.030 \text{ N}^{-3} \text{ m}^{-1}$) and N-methylmaleimide **3** ($0.047 \text{ N}^{-3} \text{ m}^{-1}$) at 20 °C.

Based on these calculations, the use of N-methylmaleimide **3** is promising for the investigation of pressure-dependent reactions. This means that when smaller aerosol particles of N-methylmaleimide **3** are used, reactions preferentially take place or, in the case of an equilibrium reaction, the equilibrium is on the product side.

4.4.2 Detection of the aerosol phase by mass spectrometry

Mass spectrometry was used to learn more about the chemical composition of the aerosol. The aerosol was collected on an adsorption tube positioned behind the flow reactor. The adsorption tube filled with sorbent, which adsorbs the aerosol as completely as possible and thus enriches the sample. The sample is then transferred from the adsorption tube to a gas chromatograph by means of TD separated and analyzed in the mass spectrometer. An advantage of this method is the short sampling time and the elimination of sample preparation. Product formation is evidenced by analysis of the obtained mass spectra. Characterization is achieved by matching the m/z and retention times with those of the reference substances.

With the developed TD-GC-MS method, the reference standard of the product N-methyl-5-norbornene-2,3-dicarboximide **5** was separated into the endo and exo form. The stereoisomer of the reaction of N-methyl-5-norbornene-2,3-dicarboximide **5** in the particle could be verified as endo. This shows that, the kinetic product is preferentially formed during the reaction in nanometer sized particles. This supports our hypothesis that pressure influences the reaction (Seguchi, Sera, Otsuki, & Maruyama, 1975).

4.4.3 Particle growth can be considered an indicator of an ongoing reaction

The Figure 4.5 (a) and (b) show the measured particle size distributions recorded after the reaction flow tube for monodisperse 30 nm aerosol particles classified in front of the reaction flow tube. The addition of cyclopentadiene **1** to N-methylmaleimide **3** results in a shift of the curve's maximum (dotted blue vs blue) indicating a particle growth. The change in particle size is likely due to either a condensation process or a reaction between the particle and the gas phase. To exclude the possibility that condensation processes are the reason for the growth, we performed the same experiment with the unreactive saturated N-methylsuccinimide **4**. In this experiment no particle growth was observed upon introduction of cyclopentadiene **1** (dotted black vs. black line). These results were replicated in experiments using 1,3-cyclohexadiene **2** as the diene. As displayed in Figure 4.5 (b), particle growth was observed for the system

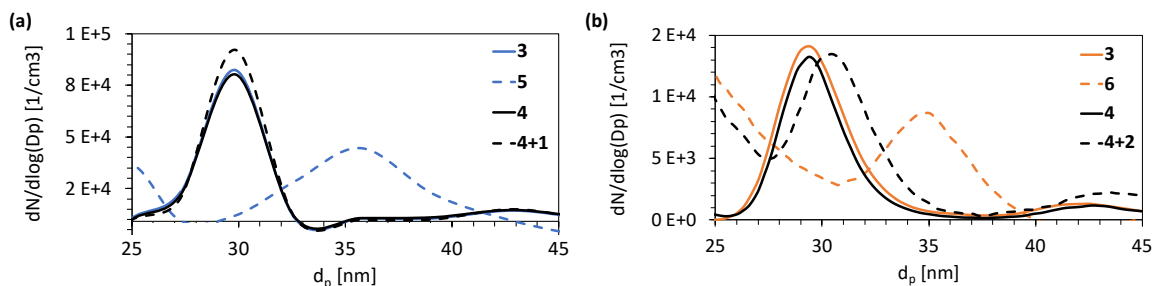


Figure 4.5 Measured particle size number concentration distribution aerosol particles initially classified at a diameter of 30 nm without and with the addition of the diene in the gas phase of **(a)** dienophile (blue curve) and after the reaction with cyclopentadiene **1** (blue dotted curve) compared to the saturated N-methylsuccinimide **4** (black curve) and with the addition of cyclopentadiene **1** (black dotted curve) and **(b)** of dienophile N-methylmaleimide **3** (orange curve) and after the reaction with 1,3-cyclohexadiene **2** (orange dotted curve) compared to the saturated N-methylsuccinimide **4** (black curve) and with the addition of 1,3-cyclohexadiene **2** (black dotted curve).

with N-methylmaleimide **3** (dotted orange line vs orange line) but not for the system with the saturated N-methylsuccinimide **4** (dotted black line vs black line).

If the particle size number concentration per cm³ after addition of a diene exceed that of the educt aerosol side reaction, side reactions or condensation processes are likely to have taken place, leading to new particle formation or growth. Growth factors of the four different reaction systems were determined experimentally for three different starting particle diameters (30, 60 and 90 nm). The results are illustrated in Figure 4.6. Experimental growth factors were calculated by division of the maximum of the particle size distribution of the reacted resp. saturated educt and the gas phase through the maximum of generated educt aerosol particle size distribution. The error bar indicates the variation between the measurements. Growth occurs above the value marked by the black line, which represents growth factor 1.

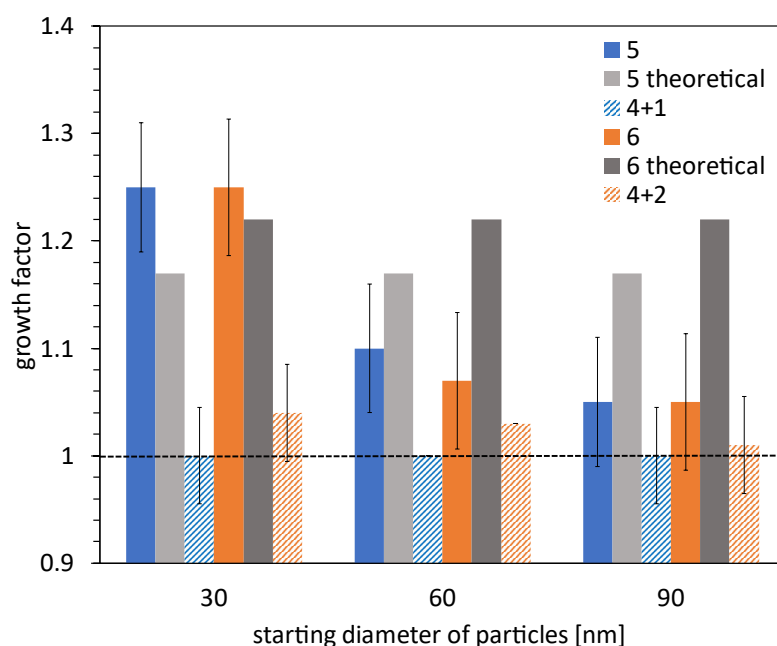


Figure 4.6 Experimental particle growth factors (particle diameter change) for the investigated reaction system with the starting diameter of particles of 30, 60 and 90 nm of N-methylmaleimide **3** and N-methylsuccinimide **4**. In addition, the theoretical growth factors for the reactions to N-methyl-5-norbornene-2,3-dicarboximide **5** and 3a,4,7,7a-tetrahydro-2-methyl-4,7-ethano-1H-isoindole-1,3(2H)-dione **6** are shown.

A size dependence was found for all three particle sizes. The reaction systems involving the dienophilic N-methylmaleimide **3** are the ones where a reaction occurs. No reaction occurs with N-methylsuccinimide **4**. This is confirmed by the growth factor. The particles with a starting diameter of 30 nm achieved the highest growth factor of 1.25 for the reaction to N-methyl-5-norbornene-2,3-dicarboximide **5** and to 3a,4,7,7a-tetrahydro-2-methyl-4,7-ethano-1H-isoindole-1,3(2H)-dione **6**. A growth factor of 1.00 was obtained for the reaction of N-methylsuccinimide **4** with cyclopentadiene, and 1.04 for the reaction with 1,3-cyclohexadiene **2**. These results suggest that no reaction occurred.

Meanwhile, particles with a starting diameter of 60 nm achieved a growth factor of 1.10 for the reaction to N-methyl-5-norbornene-2,3-dicarboximide **5** and 1.07 for the reaction to 3a,4,7,7a-tetrahydro-2-methyl-4,7-ethano-1H-isoindole-1,3(2H)-dione **6**. A growth factor of 1.00 was obtained for the reaction with N-methylsuccinimide **4** and cyclopentadiene **1**, and 1.04 for the reaction with 1,3-cyclohexadiene **2**. These results indicate no reactions occurred. Particles with the starting diameter of 90 nm exhibited almost no growth, with a growth factor of only 1.05 for both reactions. A growth factor of 1.00 was obtained for the reaction with N-methylsuccinimide **4** and cyclopentadiene

1, and 1.01 for the reaction with 1,3-cyclohexadiene **2**. These results indicate no reactions occurred. We assume that due to the larger surface-to-volume-ratio of the smaller 30 nm particles, it is more likely that the educt molecule in the gas phase will encounter an educt molecule of the aerosol particle. Therefore, the reaction is more likely to take place in smaller particles. In addition, the higher pressure in smaller particles may favor a more complete reaction, shifting the equilibrium of the reaction to the product side.

4.4.4 Substance based theoretical growth rate predictions

The experimentally determined growth factors were compared to calculated theoretical growth factors displayed in Table 4.1.

Table 4.1 Theoretical growth factors were calculated for the educt and product aerosols of 30 nm particles, assuming an ideal spherical shape. The calculations were based on molecular weight, density, mass per particle, molar mass per particle, molecules per particle, radius, and volume of the particle.

Molec.	M [g/mol]	ρ [g/cm ³] ^a		m [g/part.]	n [mol/part.]	Molec. [1/ part.]	d _p [nm]	r _p [nm]	V [cm ³ /part.]	GF _{theo}
3	111.1	1.29	±0.06	1.82 E-14	1.64 E-16	9.89E+04	30	15	1.41 E-17	1.00
5	177.2	1.29	±0.06	2.91 E-14	1.64 E-16	9.89E+04	35.0	17.5	2.25 E-17	1.17
6	191.2	1.24	±0.06	3.14 E-14	1.64 E-16	9.89E+04	36.5	18.2	2.54 E-17	1.22

^a Calculated using Advanced Chemistry Development (ACD/Labs) Software V11.02 (© 1994-2023 ACD/Labs).

The theoretical growth factors were calculated based on the assumption that the particle is spherical. The number of molecules of aerosol reactant per particle was calculated using the density of the bulk and the Avogadro constant. It was assumed that each educt reacts equivalently. The volume increase of the single molecule was then used to calculate the growth factor of the aerosol with the gas phase. This theoretical growth factor is independent of the starting diameter of the aerosol. Thus, a theoretical growth factor of 1.17 was calculated for the reaction N-methyl-5-norbornene-2,3-dicarboximide **5** and a theoretical growth factor of 1.22 for the reaction of 3a,4,7,7a-tetrahydro-2-methyl-4,7-ethano-1H-isoindole-1,3(2H)-dione **6**.

The theoretical growth factor can be utilized to estimate how high the actual growth can be at most. The theoretical growth factor could be higher due to the lower reactivity of the particles compared to the experimental growth factor. A larger experimental growth factors might be caused by an excess of the reactant in the gas phase. The analysis by mass spectrometry confirmed that there was an excess of gas phase educt besides the Diels-Alder product. Since the analysis also showed the by-product of the dimerization of cyclopentadiene **1**, it could not be excluded that this influences the growth factors. Measurements of the reaction system using the saturated educt N-methylsuccinimide **4**

showed growth factors of up to 1.04. This shows the maximal influence on the growth of particles by condensation processes and formation of by-products in total.

4.4.5 Kinetics of the DA reaction in nanometer aerosol particles

The reaction rate constants of the DA reaction in the particle were investigated by the flow tube experiments. The aim was to compare the obtained reaction rate constants of the particle reaction with reaction rate constants of DA reactions under elevated pressure and laboratory reaction conditions. Using particle size distributions obtained at different reaction times and flow rates' used reaction rate constants for the chosen DA reaction were calculated. The opening of the valve for the addition of the reactant gas (cyclopentadiene **1** or 1,3-cyclohexadiene **2**, respectively), was assumed as the starting point of the reaction. After opening the valve, a growth of the particles could be observed. The reaction is considered to have reached its end point when the maximum growth factor is achieved, indicating the reaction to the product. The time difference of the recorded particle size distributions between the reactant and the product was used for the calculations. In addition, the particle size distribution was used to calculate the concentration of the aerosol reactant N-methylmaleimide **3** in the flow tube and the yield of product N-methyl-5-norbornene-2,3-dicarboximide **5** or 3a,4,7,7a-tetrahydro-2-methyl-4,7-ethano-1H-isoindole-1,3(2H)-dione **6**. It was assumed that the reactants were completely converted to the product. In addition, any flow differences and associated fluctuations in the particle number concentration were corrected. The DA reaction is a second order reaction (Meijer et al., 1998) as described in Maskill, 2007:



Where v_a , v_b and v_c are the stoichiometric coefficients (assumed to be 1 in this study). A represents the educt N-methylmaleimide **3**, B is either diene cyclopentadiene **1** or 1,3-cyclohexadiene **2** and C the product. The rates of the reactions r were determined with the reaction time t using chemical reaction rate kinetics (Maskill, 2006):

$$r \propto \left(\frac{-1}{v_a} \frac{d[A]_t}{dt} = \frac{-1}{v_b} \frac{d[B]_t}{dt} = \frac{+1}{v_c} \frac{d[C]_t}{dt} \right) \quad (4.3)$$

The differential term for a reactant, e.g., $d[A]/dt$ is negative caused by the decrease in concentration $[A]$ during the reaction. Whereas the product's concentration $[C]$ increases resulting in the positive $d[C]/dt$ term. The second-order rate constants k of the formation of N-methyl-5-norbornene-2,3-dicarboximide **5** and 3a,4,7,7a-tetrahydro-2-

methyl-4,7-ethano-1H-isoindole-1,3(2H)-dione **6** were calculated from the following relationship adapted from Maskill, (2006):

$$-\frac{d[A]}{dt} = k[A]_t[B]_t \quad (4.4)$$

Figure 4.7 shows the reaction rate constants that have been derived for the three particle sizes investigated. They decrease towards larger particles, meaning the reaction becomes slower. This could be due to a pressure induced acceleration of the reaction in the smallest particles. However, it remains imperative to acknowledge the potential influence of surface characteristics and the particle's overall condition. We postulate that smaller particles, specifically those with dimensions of approximately 30 nanometers, may exhibit properties akin to a liquid or glassy state (amorphous solid), while larger particles, approximately 90 nanometers in size, are likely to demonstrate a more pronounced semi-solid-state behavior.

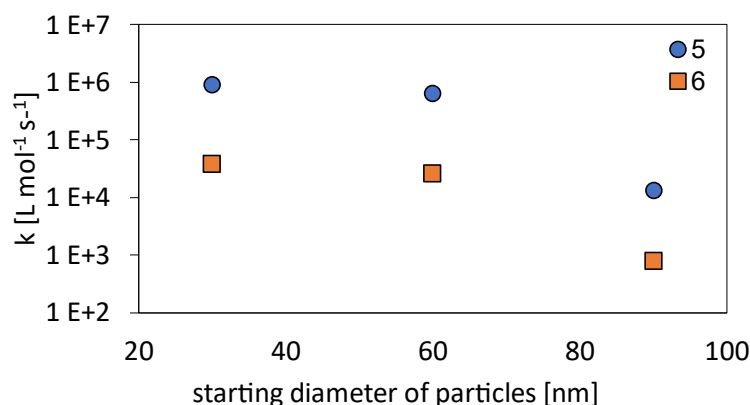


Figure 4.7 Experimental reaction rate constants of the investigated reactions N-methyl-5-norbornene-2,3-dicarboximide **5** (blue circle) and 3a,4,7,7a-tetrahydro-2-methyl-4,7-ethano-1H-isoindole-1,3(2H)-dione **6** (orange square) with the starting diameter of particles of 30, 60 and 90 nm. Experimental reaction rate constants were calculated by using equation (4.3) and (4.4).

To compare the reaction rates of investigated particle-gas phase DA reactions with DA reactions under normal conditions a rate enhancement factor $k(p)/k(1 \text{ bar})$ was calculated according to Eldik et al., 2002:

$$\frac{k(p)}{k(1 \text{ bar})} = \exp \left[-\frac{\Delta V^\ddagger}{RT(p-1)} \right] \quad (4.5)$$

Where k_p is the reaction rate constant at high pressure respectively the experimentally obtained reaction rate constant k of the reaction in the particle and k_0 is the rate constant at the reference pressure of 1 bar. ΔV^\ddagger describes the negative volume of activation, R the universal gas constant ($8.314 \text{ J mol}^{-1} \text{ K}^{-1}$) and T the temperature which is at 298.15 K in this study.

Figure 4.8 shows the rate enhancement factors for the experimentally obtained nanometer sized particle reactions and the normal DA-reaction in a vessel under increased pressure conditions.

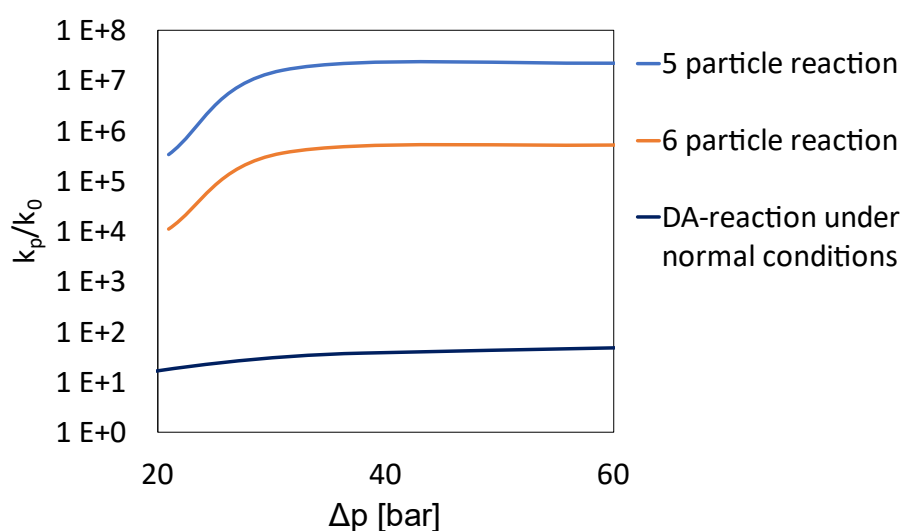


Figure 4.8 Relationship between reaction rate enhancement factor and pressure under particle reaction conditions of investigated reactions with N-methyl-5-norbornene-2,3-dicarboximide **5** (blue) and 3a,4,7,7a-tetrahydro-2-methyl-4,7-ethano-1H-isoindole-1,3(2H)-dione **6** (orange) as products and normal reaction conditions for DA reactions (black).

The rate enhancement factors for the specific DA reactions in nanometer-sized particles are up to eight orders of magnitude higher than those for larger particles. This results in faster reaction to N-methyl-5-norbornene-2,3-dicarboximide **5** ($k_{lit}(\mathbf{3+1}) = 0.0395 \text{ L mol}^{-1} \text{ s}^{-1}$ (Tang et al., 2012)) as well as to 3a,4,7,7a-tetrahydro-2-methyl-4,7-ethano-1H-isoindole-1,3(2H)-dione **6** ($k_{lit}(\mathbf{3+2}) = 0.0702 \text{ L mol}^{-1} \text{ s}^{-1}$ (Tang et al., 2012)). This result relates to Laplace's pressure in nanometer-sized aerosol particles under standard room temperature and pressure conditions. These calculations demonstrate that pressure is a crucial factor in accelerating reactions in small particles. Additionally, other factors related to the matrix of a nanometer-sized particle must be taken into consideration. These factors include the particle's viscosity, surface properties, specific reaction or

reactants, and state. The state of the particle is particularly important for reactivity, as demonstrated by Shiraiwa et al., (2013).

4.5 Conclusions

A novel model system to conduct size-dependent reactions in nanometer aerosol particles as an optimal reaction environment was developed via an experimental setup generating Diels-Alder products in aerosol particles in nanometer size range. The monodisperse aerosol particles of dienophile N-methylmaleimide **3** with initial diameters of 30, 60 and 90 nm grow to larger particles by reaction with cyclopentadiene **1** and 1,3-cyclohexadiene **2**. The growth factor for smaller particles is higher than for larger particles. Monodisperse aerosol particles of saturated educt N-methylsuccinimide **4** - the same molecule without the necessary bound for the Diels-Alder reaction - of the same three starting particle sizes as dienophile did not react with cyclopentadiene **1** and 1,3-cyclohexadiene **2** no significant particle growth occurred. Furthermore, they indicate that the reaction is accelerated in smaller particles. Furthermore, we experimentally determined the reaction rate and the corresponding reaction rate constant for all three particle sizes investigated. A comparison with literature values of DA reactions under normal laboratory conditions and increased pressure revealed that the DA reaction in the particle is up to eight orders of magnitude faster than in bulk. These data are relevant in many questions dealing with the reactions in nanometer aerosol particles. Especially the understanding of the chemical and physical background of these reactions. These results approved the developed experimental setup and procedure to investigate more reactions in aerosol nanometer particles. Research on these reactions will continue to advance our understanding of their impact on climatic effects caused by aerosol particles.

Acknowledgements. This work was supported by the German Research Foundation (DFG) under project number 416710328. .

5 Improvements and new developments on our in-house developed thermal desorption device

This chapter describes the changes to the in-house TD injector, advantages and disadvantages of the injector and the outlook for the newly developed versatile TD injector.

5.1 Introduction

In 2010, Julia Münz created an improved version of Thorsten Hoffmann's TD injector, following his example from 1992 (Münz, 2010; Hoffmann, 1992). In 2018, Simon Probst modified the software and hardware of the injector, replacing the programmable logic controller with an Arduino uno for control (Probst, 2018).

This section describes the initial state last adapted by Simon Probst, focusing on the modified parts. Chapter 2.3.1 provides a detailed description of the gas flow in this in-house TD, which remained unchanged during the conversion. The TD process also remained the same.

The motivation for the conversion is based on the working group's recent experience, with the main goal being the enhancement of the electronics' comprehensibility and structure. To achieve this, the LabVIEW program and Arduino code were adapted at the programming level in the course of a bachelor thesis (Daniel Schmidt and I cooperated). The goal was to ensure smooth program execution and prevent crashes. Additionally, the work aimed to document the program code and record parameter changes during injection. This improved traceability of the injection process and facilitated problem-solving during measurement. The aim was to optimize the heating of the focusing trap using both software and hardware, as well as enabling an increase in the maximum temperature from 210 °C to 230 °C. The focus was on minimizing hysteresis, which involves minimizing temperature fluctuations of the focusing trap and achieving the maximum temperature quickly.

5.2 The initial state

The initial status, as last modified by Simon Probst, is described here (Münz, 2010; Probst, 2018). The focus is on the control using Arduino hardware and software, the heating of the focusing trap and the programming using LabVIEW.

5.2.1 Hardware

The initial-state in-house TD injector's heater was based on a converted soldering iron (230 W) that was controlled by a solid-state relay via the Arduino. A brass tube was present in the soldering iron, through which compressed air was channeled. The brass tube absorbs the heat and conducts it to the focusing trap, heating it. The solenoid valve switches the gas flow on or off to regulate the temperature in the focusing trap.

5.2.2 Software

The control electronics for the initial-state in-house TD injector were based on LabVIEW 2015 software and an Arduino. LabVIEW controlled the software-side, while the Arduino controlled the actuators and reads the sensors. The appendix contains a circuit diagram of the control electronics and the program code of the Arduino UNO.

5.3 Implementation

5.3.1 Hardware

Two different injector heaters were used to improve the injection of the analyte from the cooled focusing trap onto the GC column. The aim was to reach the maximum temperature of 230 °C as quickly as possible and extend the use of the injector to less volatile substances by increasing the maximum temperature from 210 °C to 230 °C.

Initially, a heater from the company HS-Heizelemente is used, which consists of a stainless-steel tube containing a nickel wire. Figure 5.1 shows a drawing of the heating element. The compressed air flows through the tube into the focusing trap. A thermocouple tip is installed in the heating element to monitor the temperature. The heating element uses a power of 800 W, which is about three times higher than that of the soldering iron. The temperature sensor for the injector heater provides the advantage of better regulation, preventing overheating that can occur with soldering irons. This enables more reproducible and reliable measurements. Experiments revealed that the heating element cannot heat the compressed air quickly enough as it passes through the pipe to replace the previous injector heater. As a result, the focusing trap did not reach the target temperature of 230 °C. Due to the high output, control via Arduino was deemed unsafe after a professional check by the in-house electrician.

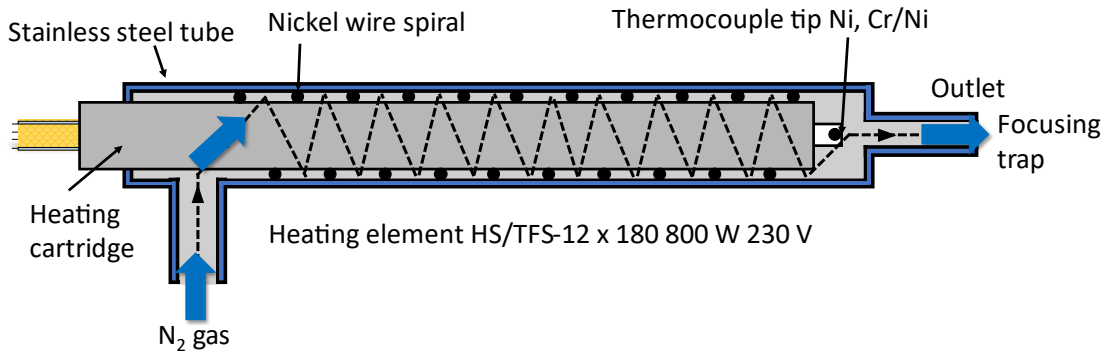


Figure 5.1 Scheme of the heater cartridge adapted from HS-Heizelemente.

Simon Probst's on/off control method had the disadvantages of fluctuation and inaccuracy, made it unsuitable for high power heaters like the one used here. The imprecise control could cause overheating and, in the worst case, a fire. To achieve more precise control, a proportional controller should be used to adjust the heater's output. This method operates by defining a temperature range. If the temperature falls outside of this range, on/off control is implemented, and the heater is turned on and off. If the temperature falls within the range, the output is adjusted to maintain a constant temperature.

A potentiometer was installed to implement pulse width modulation (PWM) control of the heating. Figure 5.2 displays the wiring, built-in parts, and the PWM control. An electrical relay was installed in the Arduino control environment for this unit.

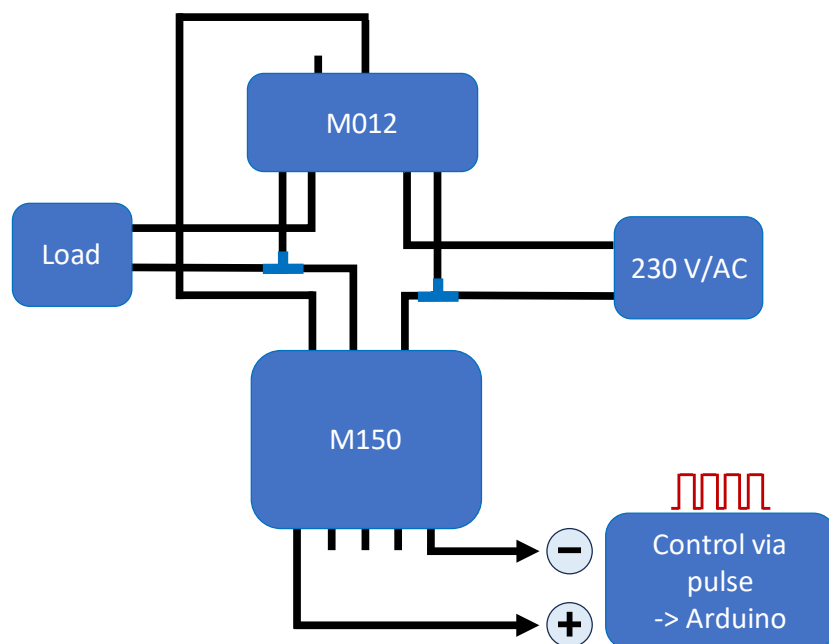


Figure 5.2 Wiring of the KEMO M012 and the KEMO M150 for controlling the injector heating using pulse width modulation. Adapted from the KEMO M150 manual (Kemo Electronic GmbH)

The KEMO M150 module was utilized to regulate the power controller, specifically the KEMO M012, through DC voltage or impulse width control via a microcomputer or PC. Control via a control pulse was executed through the Arduino. The KEMO M150 was connected in place of the potentiometer and operates through galvanic control circuit isolation via optocouplers, whereby control was achieved by altering the pulse width (10 to 90 % PWM). The optocoupler was controlled through the various control voltages inside the module. The output of the coupler was connected to a power controller module (M012), which linearly controls the potentiometer input.

However, during the practical application of the PWM, it was discovered that the temperature sensor integrated into the injector heater was not functional, and an external sensor had to be installed. As a result, the precise temperature could not be determined. Multiple measurements indicated that the temperature recorded by the external temperature sensor was 1.6 times higher than the intended temperature. To ensure that the Teflon does not melt, a safety circuit was installed to prevent the temperature of the focusing trap from exceeding 250 °C. Once the temperature reaches 230 °C, a solenoid valve was activated to switch the nitrogen supply to the injector heater on or off, which in turn heated the focusing trap.

Based on the experience with the heater from HS-Heizelemente, an injector heater was developed in-house in collaboration with the workshop of the Department of Chemistry. Figure 5.3 displays a drawing of the injector heater. It comprises a solid brass block wrapped in ¼ inch copper pipe, through which the gas flow is channeled. The brass block is preheated to a specific temperature before the actual injection. The task is accomplished using a heating cartridge with a power of 230 W, which requires some time. The temperature is regulated by an Arduino, which reads the PT 100 sensor.

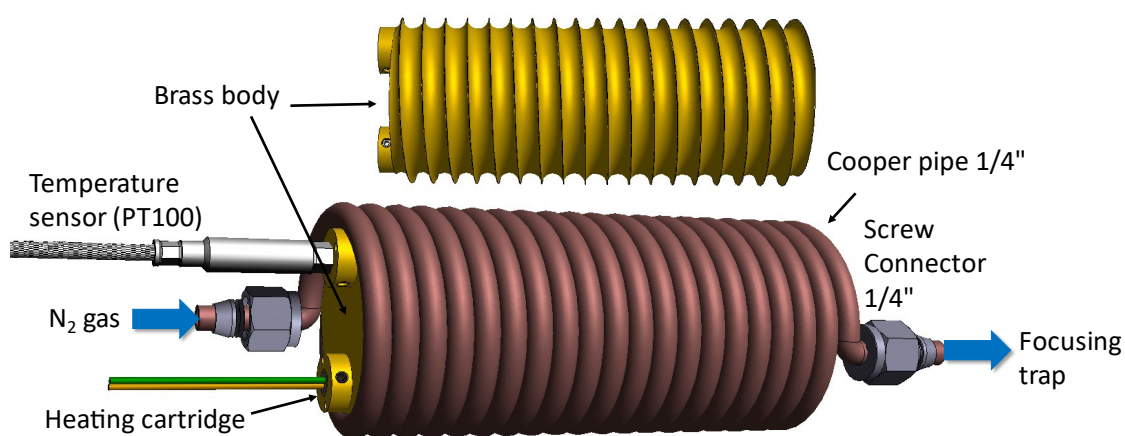


Figure 5.3 Self designed injector heater for heating the focusing trap. Drawing adapted from JGU's precision engineering workshop.

The self-built injector has the advantage of not requiring PWM control. Control via the on-off gas control has proven to be more robust and less susceptible to faults. This is due to interference signals from the PWM, which can influence the Arduino or control software, leading to program termination. Furthermore, the reduced power of the injector decreases the chances of overheating. Additionally, the internal temperature sensor ensures the safety of the heating system by functioning without the need for PWM.

5.3.2 Software

The LabVIEW software is utilized to control the TD, which in turn controls the Arduino and the GC. Additionally, the Arduino reads the temperature sensors and provides feedback to LabVIEW.

To implement the PWM of the injector heater, a dynamic approach with feedback from the temperature sensor was chosen. Previously, the injector heater was controlled using empirically determined values and on-off control. The temperature sensor did not work with the PWM, so the temperature sensor in the focusing trap was used as a reference. According to 6.3.2 several measurements indicated that the measured injector temperature should be approximately 1.6 times the desired temperature of the cold trap. This implies that the temperature of the injector heater should be around 370 °C to heat the cold trap to 230 °C. The LabVIEW implementation was based on the TD oven implementation. The PWM was initially set to 0.5, equivalent to a power of 400 W or 50 %. Once the temperature sensor in the focusing trap detects that 85 % of the target temperature has been reached, the PWM is controlled by the equation 6.1, which was derived from a combination of empirical measurements and physical formulae by Daniel Schmidt (Schmidt, 2021).

$$pwm = \frac{\sigma \cdot 0.01m^2 \cdot (273.15K + T_{target})^4}{0.38s \cdot 800W} \quad (5.1)$$

Where pwm is the pulse width modulation value, σ is the Stefan-Boltzmann constant, $0.01 m^2$ is the area of the injector heater, $273 K$ is the initial temperature in Kelvin and $800 W$ is the power of the injector heater. The average duration of an iteration of the consumer, which depends on the communication with the Arduino, was determined to be 0.38 . A section of the implementation in LabVIEW is shown in Figure 5.4. The target temperature entered by the user is displayed under 'Injector target temperature IN'. The value for the PWM was determined by tracing the lines and using a flow chart.

If the temperature exceeds the target temperature T_{target} , the control switched to the down-regulation state, and the PWM was set to 0. To prevent exceeding the target

temperature, a LabVIEW sub-program was written to regulate the injector's heating slightly earlier. This enabled achieving a deviation of only 5 °C. An illustration of the modified user interface, including the display of the injector heating, can be found in the appendix. Due to the influence on the PWM hardware described in chapter 5.3.1, the PWM for the second heater was set to 1, which corresponds to an output of 100 % and disabled it. If another heater is installed, this function could be reactivated. Additionally, the temperature sensor of the injector heater was implemented in the Arduino's program code. The code has also been supplemented.

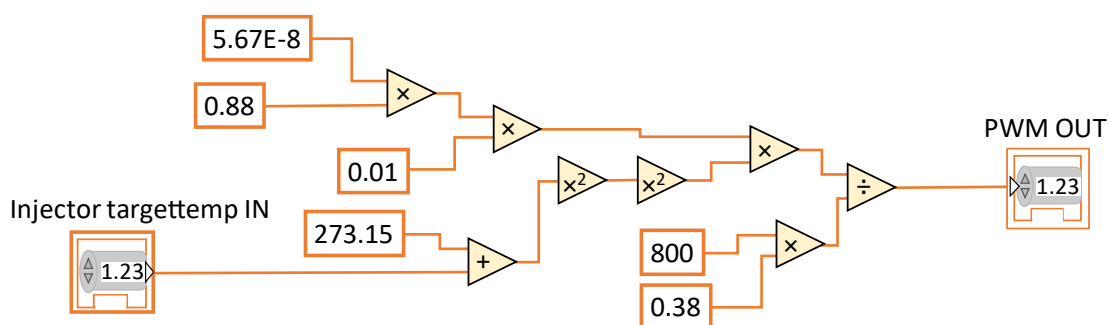


Figure 5.4 These are LabVIEW implementations of equation 5.1 adapted from Schmidt, (2021).

5.4 Conclusions and outlook

The further development of the in-house TD injector successfully increased the injector temperature from 210 to 230 °C. Designing the injector heating for safety is not a trivial task, as both performance and temperature reproducibility must be ensured. The improvements made to the system have enabled optimization. However, PWM cannot be applied due to an unresolved error signal. A not assignable frequency emitted by the PWM interferes with the temperature sensor and the control electronics, causing them to crash. To make this technology usable, a solution is required. The second heater, which is based on a pre-heated brass block wrapped in copper wires that transfer heat to the nitrogen gas, is suitable as an injector heater. This heater takes longer to reach its operating temperature, but it does not need to reach as high a temperature as the old heater. Additionally, with its on-off control, it is an easy system to understand. The in-house TD injector has been developed to work reliably and successfully injects low volatile compounds without any carryover, enabling reliable measurement. In summary, the injector's design ensures reliable and accurate results. However, working with the in-house TD injector also revealed potential improvements. Familiarizing oneself with the control electronics of the Arduino is time-consuming, despite having a circuit diagram available. Additionally, gaining insight into the LabVIEW program proved

particularly challenging. Firstly, the software, which requires a license, has to be obtained and installed with all the necessary packages. Secondly, understanding the code is not straightforward and requires some technical knowledge. A potential future alternative for a TD injector would be manual control, which would provide greater flexibility for the TD method. Additionally, no specialized software would be required, and training new students would be simplified. The design of the TD injector is prone to leaks, particularly between the focusing trap and the TD oven. Additionally, the direction of desorption results in metal abrasion and Teflon ferrule residues entering the TD gas flow path during screwing. These issues cause measurement delays and have previously necessitated time-consuming leak tests. To address these issues, one proposed solution is to alter the desorption direction by 90° or 180°, as suggested by Simon Probst (Probst, 2018). This would necessitate break-proof and flexible capillary and screw connections. Another issue that frequently arises with highly water-containing samples is capillary freezing, which obstructs carrier gas flow. This issue could potentially be resolved by using a capillary with a larger internal diameter or by not inserting the GC column as deeply into the capillary of the focusing trap. Table 5.1 provides a summary of the initial state, implementations, and outlook.

Table 5.1 Overview of the initial state, implementations and outlook of the thermal desorption injector.

Initial state	Implementations	Outlook
- Soldering iron (230°W)	- Self-designed injector heater (230 W, 2nd version)	- Commercial hot air soldering station (320 W)
- Trap max. temp. 210 °C	- Trap max. temp. 230 °C	- Trap max. temp. 250 °C
- vertical direction of gas flow	- vertical direction of gas flow	- Gas flow direction 1. desorption from bottom to top, then horizontal flow through transfer line and change of gas flow from top to bottom. 2. desorption from top to bottom
- On/Off control of heating cartridge of focusing trap (no safety shutdown)	- PWM and on/off control of focusing trap (safety shutdown)	- Manual control of heating cartridge of focusing trap (no safety shutdown)
- Automatic TD process and start	- Automatic TD process and start	- Manual TD process and start
- Use of software	- Use of software	- Only Arduino monitor for temp. sensor

6 A versatile thermal desorption system for the identification and quantification of trace organic analytes in the gas and particle phase

This chapter is a reprint of the manuscript

A versatile thermal desorption system for the identification and quantification of trace organic analytes in the gas and particle phase

Daniela Kleinsimlinghaus¹, Lukas Brill¹, Andreas Stenglein¹, Florian Menzel², Thorsten Hoffmann¹

¹Department of Chemistry, Johannes Gutenberg-University, Duesbergweg 10-14, Mainz, 55128, Germany

²Institute of Organismic and Molecular Evolution, Johannes Gutenberg-University, Hanns-Dieter-Hüsch-Weg 15, Mainz, 55128, Germany

Correspondence to: T. Hoffmann (hoffmant@uni-mainz.de)

in preparation for Atmospheric Measurement Techniques (AMT)



Abstract The combination of thermal desorption (TD) and gas chromatography (GC) coupled with mass spectrometry (MS) offers the possibility to analyze a variety of different analytes, especially volatile organic compounds (VOCs). The TD process itself is classified as an injection method involving the transfer of the analyte from an adsorption tube into the GC. The TD injector coupled to a GC-MS system operates on a simple principle: analytes collected on an adsorption tube are thermally desorbed over an extended period and concentrated in a focusing volume during desorption. This focusing volume, which can be a cooled capillary or adsorption trap, is then rapidly heated to provide a narrow injection of analytes for subsequent chromatography.

Commercially available TD systems have an extended range of applications. However, these systems may not be suitable for analyzing very low-volatility analytes and thermally sensitive organic compounds. To address these limitations, we have developed an improved and versatile TD injector, which we have coupled with high-resolution mass spectrometry. The advanced TD offers several advantages, including the shortest possible injection path for analytes without intermediate focusing on adsorbents and no use of valves or valve circuits. Additionally, the TD injector and process can be easily maintained and modified to achieve optimal results for the analytes under study. We tested the functionality of the developed system by investigating a semi-volatile organic analyte, formed by reactions of organic molecules in nanometer-sized aerosols via heterogeneous chemistry.

Keywords Trace analysis, thermal desorption, volatile, GC-MS, gas chromatography, high resolution mass spectrometry

6.1 Introduction

The adsorptive enrichment of volatile organic compounds (VOCs) in combination with thermodesorption (TD) and gas chromatography (GC), usually coupled with mass spectrometry (MS), has been successfully applied for years in a wide variety of analytical chemistry fields (Olkowska et al., 2017; Wong et al., 2012). TD is a technique that does not require time-consuming sample preparation, unlike liquid injection techniques. This speeds up and simplifies the analysis process (Woolfenden, 2010a). This method offers several advantages, including a wide volatility range of the analytes and low detection limits (Elorduy, Elcoroaristizabal, Durana, García, & Alonso, 2016; Flores & Mertoglu, 2020; van Drooge, Nikolova, & Ballesta, 2009). The combination of GC-MS enables the investigation of complex substance mixtures, such as BVOC emissions from plants or insects, which are component-rich natural substance systems. The technique is also implemented in the fields of food (Xu et al., 2021; Sales et al., 2019; Moyano et al., 2019), odor (Vallecillos, Borrull, & Pocurull, 2015; Westphal et al., 2022), and clinical diagnosis (Dospinescu, Tiele, & Covington, 2020; Li, Peng, & Duan, 2013).

The method for transferring analytes from adsorption tubes to the GC is straightforward. The analytes, which have been thermally desorbed over a set period of time, are concentrated in a focusing volume during desorption.

Subsequently, the focusing volume, which can be either a cooled capillary or an adsorption trap, is heated rapidly to enable a sufficiently narrow injection for the subsequent chromatography. To enable widespread use in routine laboratories, commercial TD instruments usually integrate additional components such as valves, valve circuits, focusing traps with special sorbents, and sample recovery components. These components create the instrumental prerequisites necessary for a wide variety of applications. Although, these additional components extend the range of application, such as the accessibility of different concentration ranges or the omission of liquid nitrogen for cooling, they can complicate the analysis of analytically challenging components, particularly those with low volatility or thermal sensitivity. For such compounds, the shortest possible injection paths, without intermediate focusing on adsorbents, are advantageous.

The development of the versatile TD injector was motivated by the need to cover a wide range of possible applications in organic trace analysis and the different methods required depending on the analyte. The TD should be adapted as specifically as possible to the sample and avoiding the influence of foreign substances or clogging of the system. Furthermore, the objective of the task is to ensure that the TD is cost-efficient, robust, and transparent, with simple operation and independent maintenance by the user in a university environment. The goal is to have inexpensive spare parts and complete monitoring of the process without any hidden software processes. Additionally, the system should be easy to modify and expand, allowing for automation with free software without any issues. Coupling a high-resolution Orbitrap GC-MS system enables precise and loss-free non-targeted analysis with a high detection limit. The need of valves, connectors or leaks should be avoided to prevent the loss of highly volatile compounds. Additionally, active surfaces and temperature fluctuations in the gas flow system at crucial points should be avoided. The system should cover the simultaneous analysis of both highly volatile and low volatile substances, eliminating dilution effects and ensuring high detection sensitivity. In summary, the aim of this study was to demonstrate the construction, the simple operation and coupling to a GC-Orbitrap-MS, and the initial testing and application in organic trace analysis of a versatile TD injector in a university environment.

6.2 Experimental

6.2.1 Sampling

A tube made of glass, metal, or another suitable material filled with sorbent can be utilized to adsorb sample or analyte. The tube must have 1/4-inch connectors with

ferrules at both ends for installation in the TD. For sampling, either a 100 mL min⁻¹ flow of nitrogen gas containing the sample was actively fed into the adsorption tube, or solutions were added to the tube using a gas-tight syringe and a volume of 1 µL of a specific concentration immediately prior to measurement.

6.2.2 Thermal desorption method

As the general TD process is described in chapter 6.3.1, the specific temperatures, waiting times and flow rates of the experiments carried out are described here.

First desorption

The desorption oven is heated with a split flow of 50 mL min⁻¹ to 250 °C, while the transfer line has a constant temperature of 250 °C and cryogenic trap has a temperature below -80 °C. Once the set temperature is reached it is hold for 10 min at 250 °C.

Second desorption

By completion of the first desorption the split is closed, and the GC-MS sequence is started. Simultaneously the focusing trap is quickly heated to 200 °C and held for 10 min.

A blank run of the same tube (same TD and GC-Method as for the analyte samples) was performed between samples to ensure TD-GC-MS system was free of carryover from the previous measurement.

6.2.3 GC-Orbitrap-MS

The developed TD injector is coupled to a Thermo Scientific™ Exploris™ GC Orbitrap™ GC-MS by inserting the GC column into the metal capillary of the TD. The connections were tightened via a T-piece (Vici Valco Tee, 1/16", .50 mm) fitting split. The helium carrier gas is controlled by a pneumatic gas controller and set at 1.5 bar to measure in constant pressure mode. The GC method started with a temperature of 40 °C holding for 10 min, followed by a gradient of 10°Cmin⁻¹ up to 220 °C held for 3 min. A blank run of the same tube (same TD and GC-Method as for ant samples) was performed between samples to ensure TD-GC-MS system was free of carryover from the previous measurement. The MS was calibrated daily and checked for leaks. The samples were analyzed using electron ionization at 70 eV in positive mode, with a scan range of 50 to 600 m/z (resolution: 60000). The temperature of the ion source and the auxiliary unit between the GC and MS was maintained at 250°C.

6.2.4 Chemicals and materials

Organic compounds were obtained from Sigma-Aldrich in the highest purity available as follows: N-methylmaleimide (97%), N-methylsuccinimide (99 %), dicyclopentadiene (contains 0,05 % butylhydroxytoluene as stabilizer), 1,3-cyclohexadiene (contains

0,05 % butylhydroxytoluene as stabilizer, 97 %), N-methyl-5-norbornene-2,3-dicarboximide (N-MND). Methanol (LC-MS grade) was used as solvent.

The solutions were brought on the tube via spiking of 1 μL with a gas-tight syringe of a certain concentration immediately before the measurement.

Inert coated stainless steel sorbent tubes with a universal sorbent (Tenax TA, Carboxen 1TD, Carboxen 1000) were purchased from Markes International Ltd. and conditioned as recommended by Markes with a series of incremental temperature steps (100, 200, 300 and 330 $^{\circ}\text{C}$ for 15 min) prior to first-time use.

6.3 Results and discussion

6.3.1 Construction and process of the developed thermal desorption injector

Construction

Figure 6.1 shows the developed TD injector with the three main parts, the desorption oven, the transfer line and the focusing trap. The injector is mounted to the GC-detector inlet with two screws and can easily be unmounted. Helium 5.0 is used as the carrier gas. It is independent from the electronic pressure control (EPC) system of the GC due to the pneumatic manometer installed in front. The manometer controls the flow of the carrier gas using a constant pressure. The individual parts and their functions are briefly explained below.

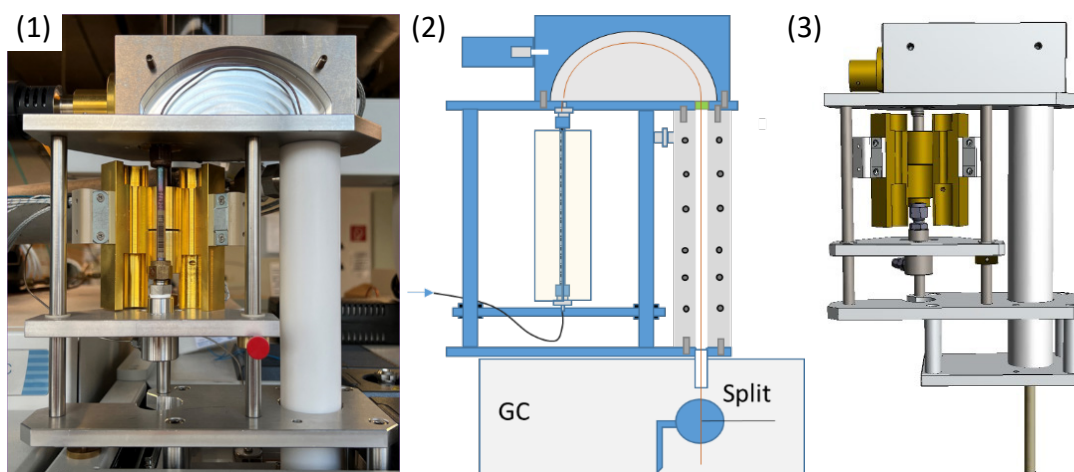


Figure 6.1 (1) Overview of the developed TD injector. (2) Flow path scheme of the analyte through the GC. (3) Technical drawing of the TD injector.

The desorption oven is comprised of two brass blocks connected by a rod at the back, with recesses for the pipe. The oven can be opened and closed safely using two PEEK handles. The adjustable height of the screw fittings and the use of standardized Swagelok fittings make it possible to investigate different length of adsorption tubes. The tubes are heated with a heating cartridge of 50 W, 230 V controlled by a

proportional-integral-differential temperature controller (ENDA ET2011 PID). A PT-100 Sensor gives the temperature feedback. The temperatures can be varied from room temperature to a maximum of 250 °C (Measuring accuracy ± 0.5 (scaling range) ± 1 digit). The analytes will be desorbed from the adsorbents of the tube by helium gas and conducted via the heated transfer line to the cooled capillary.

The transfer line consists of a heated block with a front plate in which a coated metal capillary (1/16" o. d., 0.6 mm i. d., CVD coating SilcoNert 2000 (Sulfinert) from Silcotek GmbH i.d.) leads to the cryogenic trap (further called focusing trap) and through the split as one piece. The metal capillary is mounted by a 1/16" fitting via a 1/16" – 1/4" silanised metal connector (both from Swagelok®, and CVD coating SilcoNert 2000 (Sulfinert) from Silcotek GmbH i.d.) to the adsorption tube and via a 1/16" valco fitting with a 1/16" 0.5 mm internal diameter vespel ferrule to a T-piece (Vici Valco Tee, 1/16", .50 mm). This design prevents helium leakage due to pressure from the screw connections when servicing the td injector. The transfer line block is easily opened using wing nuts. This makes it easy to check and replace the capillary and to access the capillary fittings to repair any leaks.

The focusing trap consist of a Teflon (Polytetrafluoroethylene, PTFE) tube with an 0.5 cm internal diameter. It can be cooled down to about -196 °C and heated up to +250 °C in a few seconds for the thermal injection. For that, cooled nitrogen or heated air is passed through a hole at the top of the trap. The cooling is achieved by a flow of nitrogen through liquid nitrogen. The temperature is manually controlled via a valve by the flow of nitrogen through the Teflon tube. The large 0.508 mm inner diameter of the metal capillary prevents ice blockages caused by residual water. It is important that the GC column is not pushed further into the metal capillary than just before the start of the focusing trap, otherwise the capillary may freeze. The metal capillary is inert due to silanization and does not contain sorbents, allowing for rapid and complete desorption of analytes from the adsorption tube into the focusing trap and then into the GC. The advantage of thermal desorption without changing the flow direction is that the gas flow into the focusing trap does not need to be controlled by valves. This prevents residues from accumulating in the focusing trap, valves or connections. Additionally, the large temperature change does not decompose any sorbents, which limits the choice of analytes. Therefore, this type of focusing is particularly robust. If sorbents are required to improve focus in the focusing trap or to remove solvents or contaminants, the metal capillary can be replaced at two Swagelok connections. The unique curved shape of the metal capillary and the screw connection in front of the transfer line and on the split ensures that there is no pressure on the capillary, which can lead to breakage of both the capillary and the GC column. A glass capillary can also be installed in this way. The fast thermal injection of the analyte through the GC is reached by a hot air soldering

station mounted on top of the transfer line. Hot air is pumped through the Teflon tube with the aid of a diaphragm pump to heat the capillary inside. The flow of air and the temperature on the hot air soldering station is set, with an external control unit (Digital SMD rework station- 320 W C-KOM ZD-939L). The temperature inside the Teflon tube is monitored by an PT 100 (PT100-4-GE) sensor placed in the middle of the tube read out by an Arduino uno microcontroller. The parameters temperature and time are essential to receive optimal results for the focusing step and following thermal injection and enhance trace analysis.

However, to achieve an optimum of desorption flow and to prevent carryover of analyte the use of a split flow during desorption is necessary. As written above the split consists of a stainless steel Valco T-piece valve. The split flow is increased by opening a valve at the end of a 1/16" i.d. stainless capillary. The split flow is adjusted via a needle valve and monitored with a rotameter. It is determined by a volume flow calibrator (Gilibrator 2, Sensidyne).

As mentioned before the silanized inert metal column is mounted to the T-piece fitting split. The GC column is inserted into this metal capillary to different depths depending on the analyte to be examined and is fixed with a column screw and matching vespel ferrule. This means that there is no contact with active parts of the split and dead volume is reduced.

The versatile TD injector is manually operated, making it suitable for applications of university research, without requiring complex programming skills. While constant monitoring is possible, some degree of automated control over the add-on parts is necessary. The following section explains their use and expandability.

The TD oven's heating process is controlled by a PID temperature controller to ensure reproducible desorption. Once the target temperature is reached, the PID controller minimizes temperature fluctuations. The transfer line maintains a constant temperature throughout the entire process.

The hot air gun is connected to a soldering station, where the temperature and air supply can be regulated. The temperature in the focusing trap can be measured using the PT 100 sensor. The sensor is connected to an Adafruit Max 3865, which is in turn connected to an Arduino Uno. The code used for this setup can be found in the appendix of this work.

Process

Figure 6.2 shows a schematic drawing of the versatile TD injector.

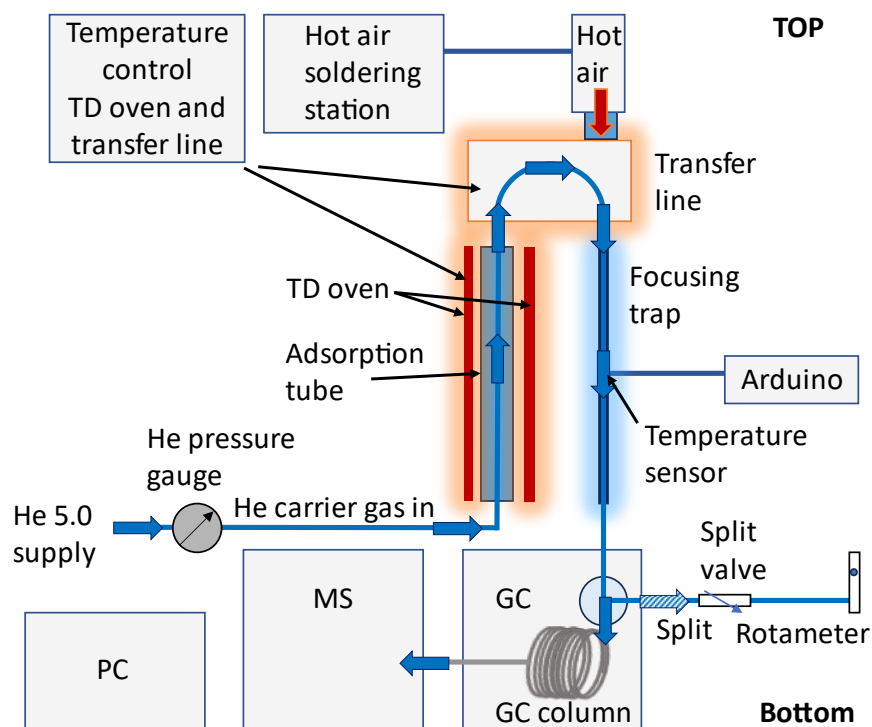


Figure 6.2 Schematic drawing of the TD injector focusing on the gas flow.

The procedure for carrying out a measurement using the thermodesorption unit and subsequent GC-MS measurement can be divided into three steps. First, a preparatory step takes place. The transfer line is heated to the desired temperature. In addition, the storage container for liquid nitrogen is filled up and the cold trap is cooled to the desired temperature. Finally, the GC-MS sequence is written, and the TD is selected and started as the injection system. The measurement is then started initiated by manually starting it on the GC. The target temperatures and heating durations for the desorption oven and for the cold trap are set. Once the target temperature of the transfer line and the cold trap is reached, the second step begins, the desorption of the tube respectively the pre-concentration of the analyte. For this, the tube is first screwed into the device at the top and then at the bottom. The flow of helium and any leaks are monitored by a rotameter located behind the split. The desorption oven is closed and heated to the target temperature. When the target temperature is reached, the timer is started. During the desorption process, the split is open, and the cryogenic trap is cooled. After the time for the desorption process has elapsed, the step of injecting the analytes into the GC starts. First, the split is closed. Then the GC-MS measurement is started. This is followed by switching off the liquid nitrogen for the cold trap and heating to the

previously set target temperature using a heating air dryer. Once this is reached, the timer for the injection process starts and the temperature is maintained. After the time has elapsed, the heating air dryer is switched off and the injection process is completed.

6.3.2 Performance tests and application

The performance of the versatile TD injector was evaluated based on low, middle, and high volatile compounds. To exclude misinterpretation of substances and to clearly allocate them, a blank measurement was carried out before and after each measurement.

One of the most decisive factors for successful desorption is the rapid heating of the cold trap after desorption of the adsorption tube and the simultaneous start of the GC-MS run. This starting point and the heating curve of the cold trap should be as reproducible as possible to ensure comparability of the measurements. Changing this starting point leads to a shift in the retention time of the volatile compounds, i.e. substances that are measured at the beginning of the measurement. For non-volatile or semi-volatile substances, the final temperature of the cold trap is crucial for complete desorption and reproducible measurements. Figure 6.3 displays a heating period of the cold trap during injection to the GC-MS. For this injection the target temperature of the cold trap was 175 °C starting from about -100 °C. Successful desorption from the focusing trap was achieved due to the rapid temperature increase at the start and reaching the target temperature within 2 minutes. In addition, the focusing trap is not heated above the target temperature, which could potentially destroy sensitive analytes or the trap itself.

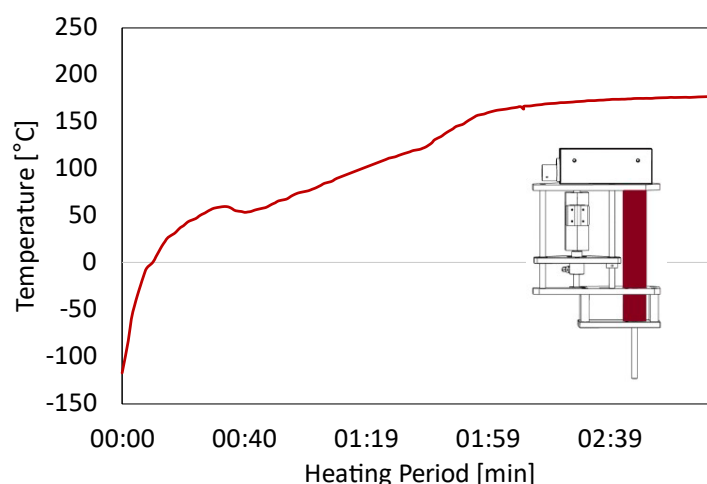


Figure 6.3 Graph of increase of temperature during the heating period of the cold trap to inject the focused sample to the GC-MS.

To check for carryover and complete desorption of the tube 1 ppm of N-methyl-5-norbornene-2,3-dicarboximide (N-MND) was desorbed from the tube. This substance can be classified as a semi volatile compound which tends to adsorb onto the walls of tubing and valves of the gas flow in the TD injector. As displayed in Figure 6.4 the analyte can be identified. It shows the extracted ion chromatogram of the most abundant fragment of the molecule with the m/z of 112. A second tube desorption measurement checking for carryover shows no analyte.

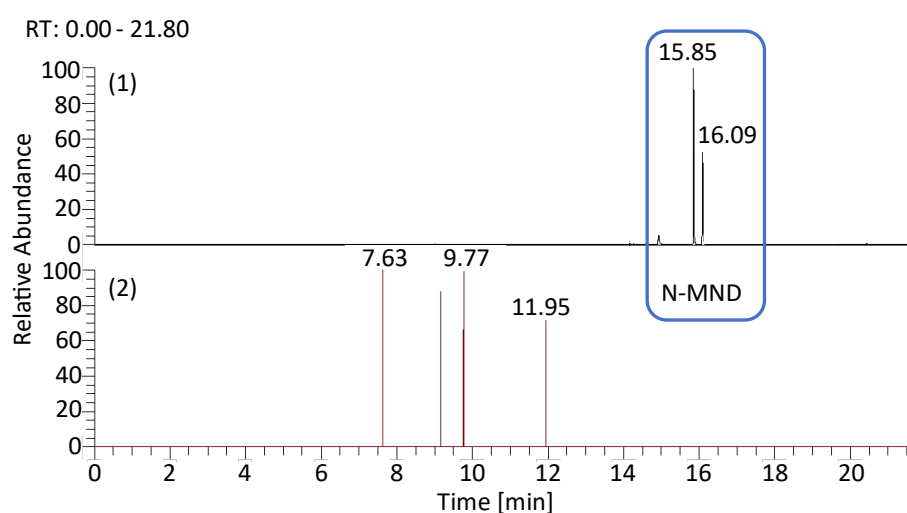


Figure 6.4 Extracted ion chromatogram (EIC) of the 1 ppm Standard N-MND solution spiked on an adsorption tube to check for complete desorption and carryover of semi-volatiles. (1) shows the EIC of the first measurement and (2) shows the EIC of the second measurement directly after the first measurement.

This implies to a complete desorption of the analyte and residue-free injection into the gas chromatograph. In the chromatogram, two peaks can be assigned to the substance N-MND. This is since the substance is present in the standard as a stereo isomer.

Figure 6.5 shows three chromatograms from three different measurements. All three measurements have a peak at RT 0.85 to 0.93 min. This is caused by the same substance in all three measurements. The deviation of the retention time by 0.08 min shows how reproducible the versatile TD injector works. It should be noted here that these measurements were carried out without automation, i.e. as described under 6.3.1.

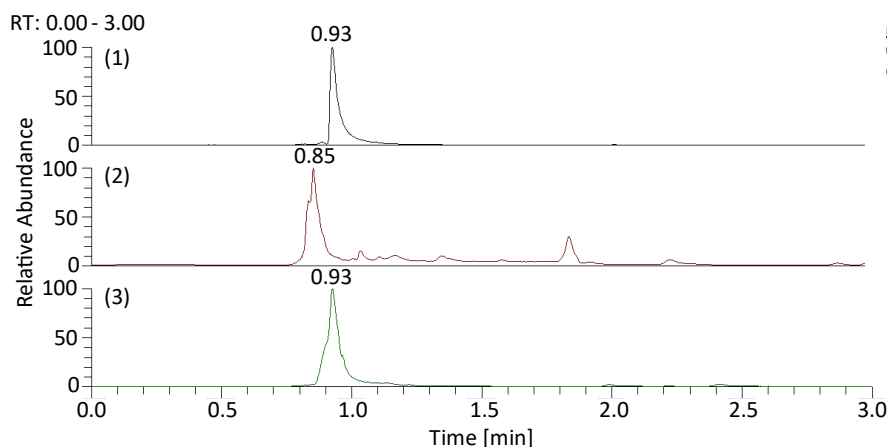


Figure 6.5 Chromatograms from three different measurements demonstrating the reproducibility of retention time shifts.

Automation with simultaneous detailed temperature monitoring of the injection step from the cold trap would probably lead to even better reproducibility at this point. However, this was not necessary for the measurements shown here.

6.4 Conclusions and outlook

In summary, the developed TD injector demonstrates a robust construction and an efficient process for preconcentration and injection of analytes into a gas chromatograph. The modular design of the desorption oven, transfer line and focusing trap allows for easy assembly and disassembly, facilitating maintenance and versatility in experimental setups. The integration of temperature control mechanisms, such as heating temperature control units with PIDs and cryogenic cooling, ensures precise control of desorption and injection conditions, essential for achieving reproducible results. The performance of the system has been evaluated through tests, including analysis of volatile and semi-volatile compounds. The results showed successful desorption, minimal carryover, and reproducible retention times, demonstrating the reliability of the injector for analytical applications. While automation could further improve reproducibility, the demonstrated manual operation already gives satisfactory results. Overall, the developed TD injector represents a promising tool for improving the analysis of trace compounds in diverse sample matrices.

7 Novel non-invasive method to investigate volatile trace emissions of ants and their brood with thermal desorption gas chromatography Orbitrap mass spectrometry

This chapter is a reprint of the manuscript

Novel non-invasive method to investigate volatile trace emissions of ants and their brood with thermal desorption gas chromatography Orbitrap mass spectrometry

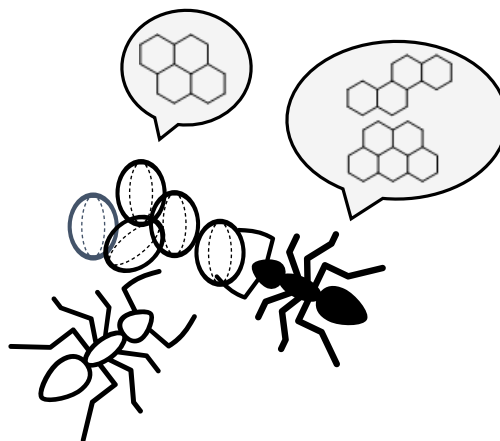
Daniela Kleinsimlinghaus¹, Florian Menzel², Thorsten Hoffmann¹

¹Department of Chemistry, Johannes Gutenberg University, Duesbergweg 10-14, Mainz, 55128, Germany

² Institute of Organismic and Molecular Evolution, Faculty of Biology, Johannes Gutenberg University, Hanns-Dieter-Hüsich-Weg 15, Mainz, 55128, Germany

Correspondence to: T. Hoffmann (hoffmant@uni-mainz.de)

in preparation for Methods in Ecology and Evolution



Abstract Motivated by the potential for trace analysis and uncertainty regarding communication among social insects via volatile gas phase, we have developed a non-invasive method to gain initial insights into these processes in *Temnothorax nylanderi* and *Temnothorax longispinosus* species. Laboratory experiments were carried out under ambient atmospheric conditions using synthetic air. A specially developed glass device was built to avoid matrix effects while sampling the gas phase in adsorption tubes. The adsorption tubes were measured by thermal desorption coupled with a high-resolution GC-Orbitrap-MS, which allows the determination of sum formulas. The ants and their brood were investigated separately to compare the emitted gas phases. We investigated whether there are differences between species and between emissions of ants and brood. We found that ants and brood of both species emit a gas phase. Especially the substance class of perhydropyrenes looks very promising to better understand the communication between ants and their brood.

Keywords chemical communication, trace analysis, TD-GC-Orbitrap-MS, volatile organic compounds, Nestmate recognition, *Temnothorax nylanderi*, *Temnothorax longispinosus*, Formicidae, Brood recognition

7.1 Introduction

Social insects have fascinated humankind for a long time. The biomass of ground-dwelling ants was estimated by Schultheiss et al., (2022) to be over 3×10^{15} individuals and the number of ants on the whole earth to be almost 20×10^{15} individuals. The is equivalent to a biomass of about 12 megatons of dry carbon (Bar-On, Phillips, & Milo, 2018; Schultheiss et al., 2022). Their efficient organization requires sophisticated and intense communication among all colony members (Howard & Blomquist, 2005; Leonhardt et al., 2016). Cuticular hydrocarbons (CHCs) play a major role in social interactions between workers (Greene & Gordon, 2003; Pamminger, Foitzik, Kaufmann, Schützler, & Menzel, 2014b) or between the queen and the workers (van Oystayen, Oliveira et al. 2014). They are embedded in the cuticular lipid layer of all insects and have been extensively studied over the last 30 years (Kather & Martin, 2015). They are measured as so-called CHC profiles and determine the chemical footprint of insects (Kather & Martin, 2015). Among other substances, cuticular hydrocarbons (CHCs) such as alkanes and, alkenes, with different chain lengths were identified as the most important chemical communication signal between ants and other social insects (Menzel et al., 2017). CHCs also protect the ants from desiccation due to their waterproofing effect and serve as sex pheromones (Jallon, 1984; Thomas & Simmons, 2008; Beros et al., 2017). Additionally, they can act as a chemical cue for recognizing mates and nestmates (Kather & Martin, 2015). The texture is semi-fluid and can be imagined as viscous wax layer as the hydrocarbons aggregate tightly, relying on Van-der-Waals forces (Menzel et al., 2017). The composition is mainly determined by genetic

factors (van Zweden et al., 2009). CHCs can provide information about the group's status and membership, task and the reproducibility (Menzel et al., 2017; Pamminger et al., 2014b). They are exchanged through trophallaxis (passing liquid food from the mouth or anus of one animal to another) and allogrooming (physical contact such as cleaning (Boulay et al., 2000; V. Soroker et al., 1995; Victoria Soroker et al., 1995). Each colony has a unique scent when in contact with their nestmates (Boulay et al., 2000; V. Soroker et al., 1994). Chemically, CHCs describe a complex profile with over 100 different substances that are difficult to identify. In detail, you get different molecules with the same molecular formula can be obtained by varying the number and position of the hydrocarbon atoms as well as whether they are saturated or unsaturated, branched, or linear (Menzel et al., 2017). This diversity of hydrocarbons may be due to the varying demands placed on the CHC layer (Wittke et al., 2022). On the one hand, it should be waterproof, which tends to favor more viscous hydrocarbons (Rourke & Gibbs, 1999). However, this property hinders the exchange of the CHC layer between the ant and the brood. Alkanes with methyl groups or branched molecules that aggregate less are more favorable. Further chemical signals involve alarm pheromones, such as 2-Tridecanone having a defensive function (Wyatt, 2014). Others are trail pheromones (David Morgan, 2009). Multiple species may use the same chemicals, such as Z,E- α -farnesene and 2,5-Dimethyl-3-ethylpyrazine, as the basis for their trail pheromones. However, these are often combined with hydrocarbons that are specific to each colony (Adams, Wells, Yanoviak, Frost, & Fox, 2020; David Morgan, 2009). In addition, several terpenes and terpene esters have been found in extracts of ant glands (Howard & Blomquist, 2005; Ruther, Sieben, & Schricker, 2002). However, communication between larvae and nurse workers, which care them, is still poorly understood. While there seems to be signaling based on little-volatile cuticular hydrocarbons (Dunn, Hodapp, Menzel, & Kohlmeier, 2024), it is still unclear whether larvae-worker communication using volatile compounds also plays a role. Research in this field has been hampered by presumably tiny substance quantities and the methodological difficulties to detect and identify such compounds.

Previous studies have shown that they use chemicals for communication (Attygalle & Morgan, 1984; Menzel et al., 2017; Traniello & Hölldobler, 1984). In the past, pheromone trails have been investigated and behavioral studies have been carried out (David Morgan, 2009; Glaser & Grüter, 2018; Traniello, 1989). The method currently used for the analysis of CHCs is the preparation of solvent extracts. This is done by soaking ants in different solvents and then extracting them or by washing the ant with a solvent and then collecting it. The solvent extracts obtained are analyzed using GC-MS (Beros et al., 2017; Guarda & Lutinski, 2020; Menzel et al., 2017).

The method developed in this study is suitable for analyzing the volatile gas phase of living ants as well as from their brood. By examining the living insect by transferring it into a constructed glass device setting, we aim to gain an authentic insight of how a

chemical profile of their volatile gas phase looks like. Collecting solvent such as hexane extracts from the ants or brood does allow for the detection of volatile compounds of approximately C-11 and longer chains (Dunn et al., 2024). Additionally, it is to be achieved to differentiate between substances on the surface of the ants and those in the gas phase, making it possible to clearly identify them as communication signals. The comparison of two different species will show whether there are differences in the type and quantity of molecules emitted. The aim is also to find out whether the brood also has a chemical signature, for example to express signals of hunger or other needs. Furthermore, by examining ants and brood separately, a comparison in their communication signals is to be detected. Methodologically, the aim is to record the volatile gas phase with minimal background signals. The collected samples are analyzed using direct sampling via a TD injector which is specially developed for trace analysis and coupled to a high resolution Orbitrap GC-MS enabling a non-target screening approach. The aim of this study is to develop a TD-GC-MS method that allows the measurement traces of gas phase concentrations of volatiles as well as semi-volatiles and to exclude background signals. To the best of our knowledge, this is the first non-invasive study of the volatile gas phase of ants and their brood.

7.2 Materials and methods

7.2.1 Experimental design

Setup

The design of the sampling design was chosen based on two goals: To create an environment that contains as few stressors as possible and that also contains as few contaminants as possible that could falsify the measurement. Figure 8.1 shows a schematic illustration of the glass device developed. It consists of two glass tubes that have pushed one another. Part **A** consists of a core with straight olive, NS 29/32 with a standard ground joint and a length of 40 mm. The glass part **B** consists of a reducer with olive NS 29/32 with a standard ground joint of the length 120 mm. Tapered at the outer ends are glass frits. These prevents ants or brood from getting out of the glass device. Both sides have a connection for hoses to connect the air on one side and the adsorption tube on the other.

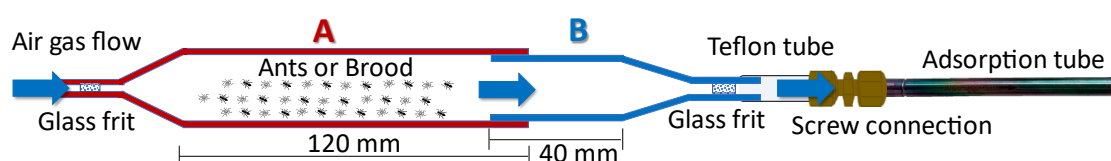


Figure 7.1 Developed glass device for the investigation of the emitted gas phase of ants and brood.

Sampling

Two species of ants were used, both belonging to the Formicoxenini tribe (Formicidae: Myrmicinae). *Temnothorax nylanderii* (*T. nyl.*) colonies were collected in the Gonsenheim forest near Mainz (Germany). *Temnothorax longispinosus* (*T. lon.*) colonies were collected at Huyck preserve, NY, USA. All colonies were kept in plaster nests and provided with water, dead *Drosophila* flies, and honey ad libitum.

To prepare the measurement, the adsorption tube was conditioned by mounting it in the TD injector described in chapter 0. The adsorption tube inside the oven of the injector was heated to 250 °C for 30 min with an open split under a helium flow of 50 mL min⁻¹ directly before the experiment. The developed glass device was thoroughly cleaned with distilled water and subsequently with acetone. It was then dried overnight in a drying oven at 150 °C.

For measurements, the device was set up as described in the Setup section yet initially without an adsorption tube. Synthetic air was passed through the device for 30 min at a flow rate of 100 mL min⁻¹ for conditioning. The device was heated using a 20 W halogen lamp with warm white 2800 Kelvin and 255 lumen output, reaching a temperature of approximately 40 °C. This will ensure that the ants are active and moving, increasing the likelihood of communication between them. Additionally, it will result in the emission of more substances, which can be detected. In the meantime, the adsorption tube was installed in the TD injector. The TD oven, the transfer line, and the GC oven were heated to 250 °C and the focusing trap was heated to 230 °C and held for 30 min to remove any impurities in the system. After cooling to room temperature, a GC blank was measured. Next, the adsorption tube was measured to serve as a background blank. Afterwards, the adsorption tube was connected to the device and sampled for 1 hour at 100 mL min⁻¹ flow and analyzed immediately afterwards. While the TD-GC-MS measured the device blank, forty ants or 40 pieces of the brood were carefully placed in the device with featherweight tweezers. The adsorption tube was attached directly to the device after the blank measurement and sampled for 1 h at a flow rate of 100 mL min⁻¹. The sample was then measured directly using TD-GC-MS. To ensure that complete desorption had taken place, the adsorption tube was immediately desorbed and measured a second time.

7.2.2 Analysis

Thermal Desorption Method

As the general TD process is described above, only the specific temperatures, waiting times and flow rates of the experiments carried out are described here.

First Desorption

The desorption oven was heated with a split flow of 50 mL min⁻¹ to 250 °C, while the transfer line had a constant temperature of 250 °C and the cryogenic trap had a

temperature below -80 °C. Once the set temperature was reached it was held for 10 min.

Second Desorption

Once the first desorption is finished the split is closed and the GC-MS sequence is started. Simultaneously, the cryogenic trap is heated to 250°C (approx. 3 min) and held at that temperature for 10 minutes.

A blank run of the used adsorption tube using the same method was performed between samples to ensure the TD-GC-MS system was free of carryover.

GC-Orbitrap-MS

The TD injector is coupled to a Thermo Scientific Exploris GC Orbitrap GC-MS™ by inserting the MEGA-DEX DMT β column (Dimethyl-*tert*-butyldimethylsilyl-β-cyclodextrin 25 m × 0.25 mm i.d. × 0.15 μm film thickness, MEGA S.r.l., Legnano, Italy) into the metal capillary of the TD. The connections were tightened via a T-piece (Vici Valco Tee, 1/16, 0.5 mm bore, SS) fitting split. The helium carrier gas is controlled by a pneumatic gas controller and set at 1.5 bar to measure in constant pressure mode. The GC method was started with a temperature of 40 °C holding for 10 min, followed by a gradient of 10 °Cmin⁻¹ up to 220 °C held for 3 min.

Data Analysis

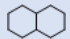
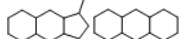
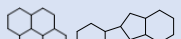
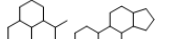
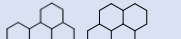
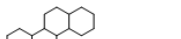

Raw data files of samples and blanks were analyzed using the Software Qual Browser Thermo Xcalibur 4.1.31.9. Measured mass spectra were compared using the NIST Library 2020.

7.3 Results and discussion

The emitted gas phases of ants and brood of *T. nyl.* and *T. lon.* were successfully measured and analyzed. By measuring device blanks directly before sampling ants or brood, measured signals could be clearly assigned to the sample. The overall GC-MS total ion current (TIC) chromatograms have a raised baseline from retention time 19 to 26 min. These increases in baseline are referred to as unresolved complex mixtures (Ventura et al., 2008). They are described as containing a large number of substances that cannot be separated by chromatography. By using target screening and the high-resolution Orbitrap instrument, we were able to obtain certain substances from the emitted gas phase of ant and brood samples, combined with measurements of blanks. The samples included a diverse range of biological substances. Some substances still require further analysis for precise identification. The perhydropyrenes and related substances were identified and determined in all samples and will be discussed here. The similarity of their structure to that of hormones makes them interesting. Additionally, Ventura et al., (2008) reported the presence of perhydropyrenes in

sediments, which may have a biological origin. Most elements in nature exist as a mixture of isotopes. For instance, natural carbon is composed of 98.90 % of the isotope ^{12}C and 1.10 % of the isotope ^{13}C . These isotopes produce peaks in the mass spectrum, which manifest as isotope clusters and are indicative of the element's composition. Here is an explanation: The nonminimal mass fragments $\text{C}_{10}\text{H}_{20}$ and $\text{C}_8\text{H}_{12}\text{O}_2$ produce peaks at mass 141 with 11 % and 8.8 % abundance at mass 140 u, respectively. This is due to the varying statistical probability of ^{13}C isotope presence, allowing for differentiation between the two elemental compositions in mass analysis (E. de Hoffmann & Stroobant, 2007). A summary of the detected molecular masses of the perhydropyrenes and their ^{13}C masses, the proposed structures and the occurrence in ants and brood for both species are summarized in Table 7.1. The percent agreement with the comparison spectra of the NIST library based on the mass spectra of the ant *T. nyl.* is due to the higher signal intensity. In the following

Table 7.1 Structures, mass-to-charge ratio (m/z), ^{13}C mass-to-charge ratio, retention time (RT), and occurrence in ants and brood of the respective perhydropyrene species found.

Compound	m/z (exact mass)	m/z (^{13}C)	RT [min]	Ant <i>T. nyl.</i>	Brood <i>T. nyl.</i>	Ant <i>T. lon.</i>	Brood <i>T. lon.</i>
$\text{C}_{10}\text{H}_{18}$ 	138.1409	139.1442	18.70	X	N.A.	N.A.	N.A.
$\text{C}_{14}\text{H}_{24}$ 	192.1878	193.1912	20.31	X	N.A.	X	N.A.
$\text{C}_{16}\text{H}_{26}$ 	218.2035	219.2068	23.02	X	X	X	X
$\text{C}_{16}\text{H}_{28}$ 	220.2191	221.2225	21.47	X	N.A.	X	N.A.
$\text{C}_{17}\text{H}_{28}$ 	232.2191	233.2225	23.34	X	X	X	X
$\text{C}_{18}\text{H}_{30}$ 	246.2348	247.2381	23.81	X	X	X	X
$\text{C}_{19}\text{H}_{30}$ 	258.2348	259.2381	25.30	X	X	X	X

The mass spectrum of the compound $\text{C}_{10}\text{H}_{18}$ has been confirmed by the NIST library spectrum of decahydronaphthalene. Both mass spectra are displayed in the Appendix in Figure A 9.2. The exact ^{13}C mass-to-charge of $\text{C}_{10}\text{H}_{18}$ (m/z 138.1409) can also be found. Six of the main fragments can be found in the reference spectrum. The fragmentations show that the measured molecule is decahydronaphthalene. However, a percentage match cannot be given as the concentration was too low. The compound was only found in the samples of ants *T. nyl.* The concentration in the other samples was too low.

Based on the fragmentation pattern of the mass spectrum at a retention time of 20.31 min two different structures with the formula $C_{14}H_{24}$ can be considered. One is tetradecahydroanthracene, shown in the appendix in Figure A 9.2. Most of the fragments match the NIST library spectrum, resulting in an overall match of 8 %. The low percentage match could be attributed to the low concentration of the analyte. However, in the measured mass spectrum there is a fragment with the exact mass of 177.1638 which does not appear in the NIST library spectrum. This fragment ion, which is $[M^+-15]$, may indicate the presence of a methyl substituent on the ring system. This leads to the second possible structure of dodecahydro-1-methyl-1H-benz[f]indene and corresponding fragments which are illustrated in the appendix in Figure A 9.3. Suggestions of fragments are also shown. No NIST library spectrum is available for this compound. However, the presence of the $[M^+-15]$ peak renders the second proposed structure more likely.

At the retention time of 23.02, the mass spectra shown in Figure 7.2 and Figure 7.3 were obtained for ants and the brood of both studied species. Suggested structures are hexadecahdropyrene and hexadecahydro-indeno[2,1-a]indene. A comparison with the NIST library spectra of both structures with the measured ones revealed that the hexadecahdropyrene shows a better agreement. Fragments with lower intensities such as m/z 189 and m/z 135 were also found, resulting in an overall match of 64 %. However, there is a possibility that hexadecahydro-indeno[2,1-a]indene is also present. Barlin et al., (1976) investigated fire ant trail pheromones by extracting Dufour's glands from *S. richteri*. They found a mass of 218 by analysis with gas chromatography and predicted the formula of $C_{16}H_{26}$ with a structure of hexadecahydro-indeno[2,1-a]indene. This could possibly correspond to the molecule we found and indicate the perhydropyrene found here and thus establish a connection to mass 218.

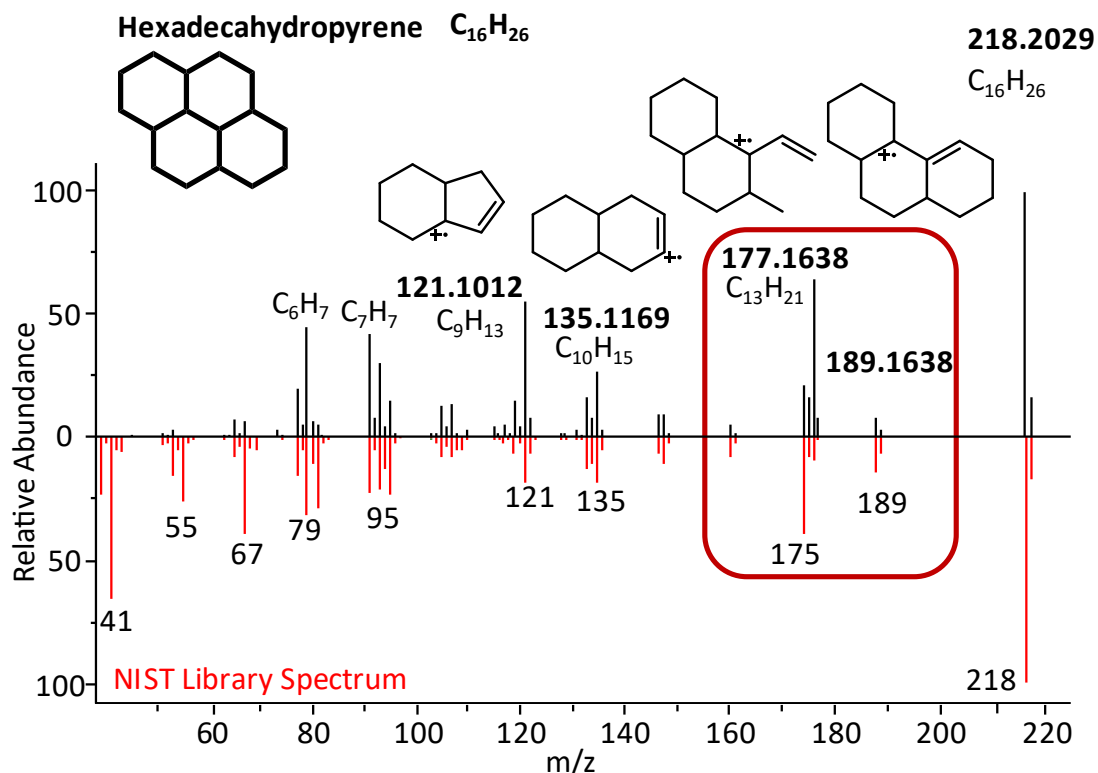


Figure 7.2 The mass spectrum of compound $C_{16}H_{26}$ in comparison to the NIST library spectrum of hexadecahydropyrene (red). Four major fragments of m/z 121.1012, 135.1169, 177.1638, and 189.1638 were identified and their suggested structures were provided. The m/z values of 189 and 177, labelled with a red rectangle, highlight the difference to the mass spectrum of hexadecahydro-indeno[2,1-*a*]indene and thus a higher agreement with the mass spectrum of hexadecahydropyrene, indicating that this structure is more likely to be present.

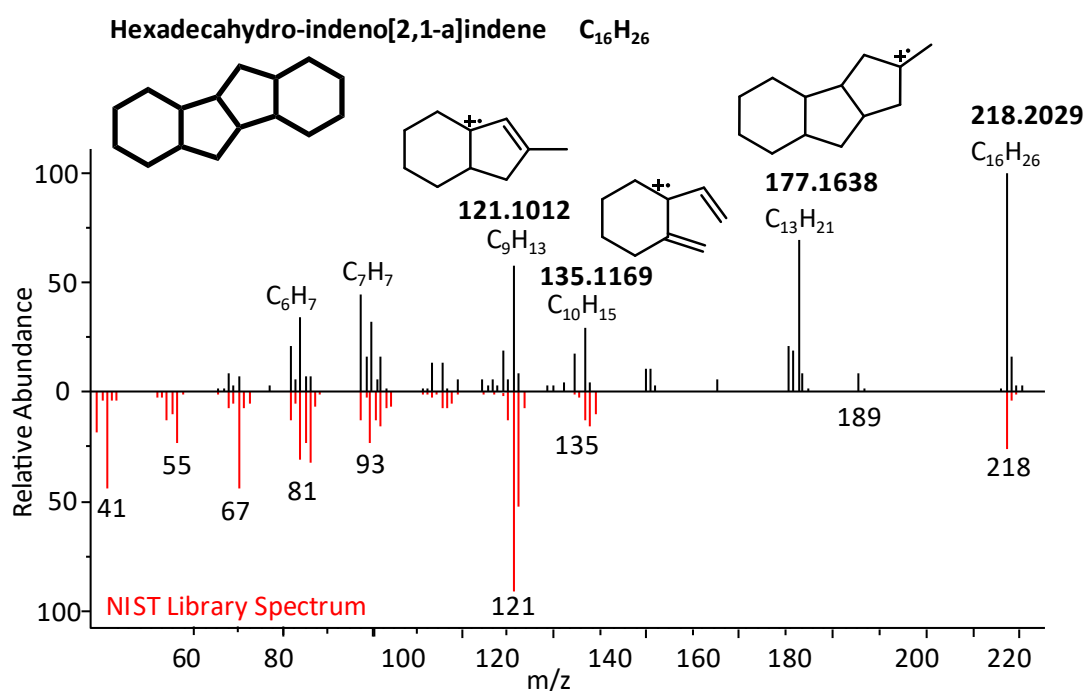


Figure 7.3 The mass spectrum of compound $C_{16}H_{26}$ in comparison to the NIST library spectrum of hexadecahydro-indeno[2,1-a]indene. Three major fragments of m/z 121.1012, 135.1169, 177.1638, and were identified and their suggested structures were provided.

A peak with the sum formula $C_{16}H_{28}$ of m/z 220.2187 was only prominent only in the ant samples. The fragment ion 205.1952 ($[M^+-15]$) suggests the presence of a methyl substituent on the perhydropyrene ring system. A structure and fragments are proposed in Figure 7.4. The structure could not be confirmed by the NIST library due to the lack of a comparative spectrum.

$C_{17}H_{28}$ tetracyclic perhydropyrenes were also detected in ants as well as in the brood. Two possible structures can be predicted based on the fragmentation. One is 4-methyl-hexadecahydropyrene, with an overall match of 33 % with the comparative NIST library Spectrum. The fragment ion with m/z 217.1951 ($[M^+-15]$), through a methyl cleavage, suggests that this or a similar structure with a methyl group is present. On the other hand, hexadecahydro-benzo[de]anthracene is an alternative structure with an overall match of 38 % with the comparative NIST library spectrum. Here, the fragment ions with the m/z ratios 175.1482 and 121.1012 are typical. Ventura et al., 2008 also measured these mass spectra from their samples of extracted sediments from the Late Archean. Comparing the mass spectra, the 4-methyl-hexadecahydropyrene is the more likely structure due to the fragmentation pattern and the occurrence of fragment ion m/z 217.1951.

Another characteristic fragmentation pattern for a perhydropyrene was found at RT 23.81. The m/z ratio 246.2343 and the fragmentation pattern identified that it is a $C_{18}H_{30}$ compound. Figure A 9.5 illustrates the measured mass spectrum and the compared NIST library spectrum. The fragment ions are also displayed, indicating an

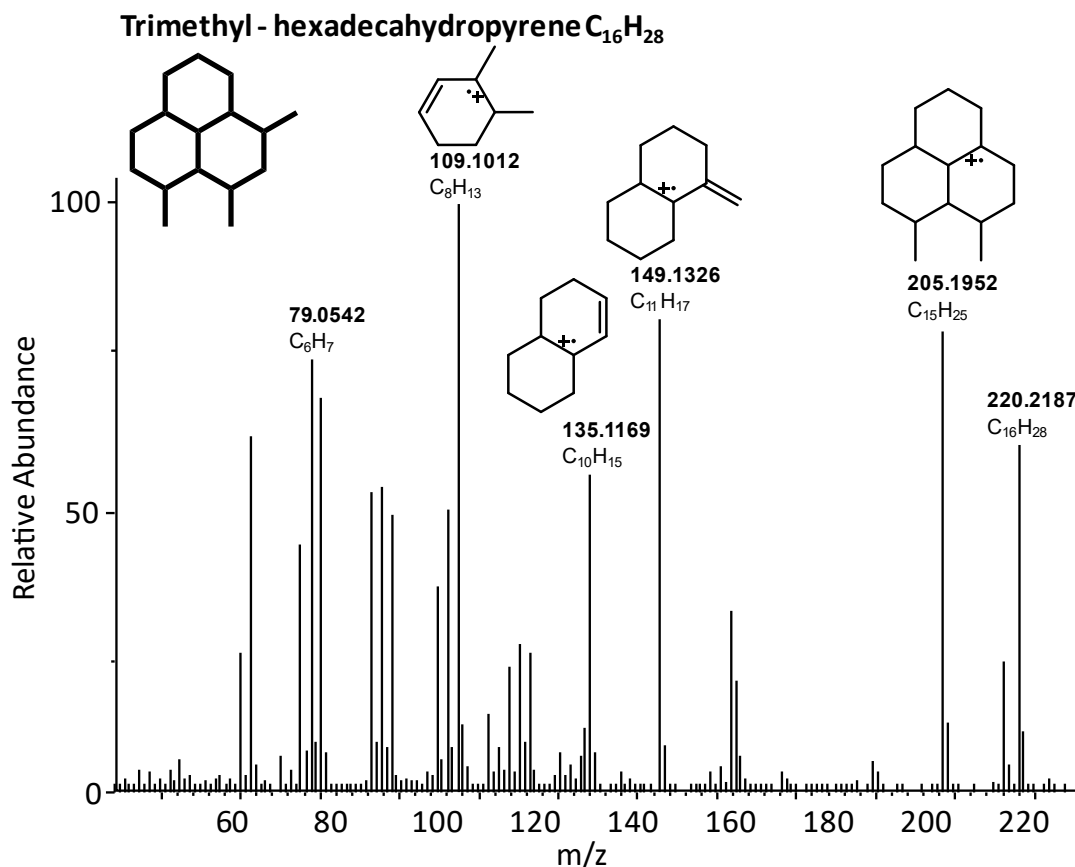


Figure 7.4 The mass spectrum of the molecular formula $C_{16}H_{28}$ and its associated fragment ions were analyzed. Four major fragments were identified with m/z values of 109.1012, 135.1169, 149.1326 and 205.1952. The proposed structures for each fragment were provided.

overall match of 35 % with the comparative NIST library Spectrum. The structure of the suspected octadecahydro-chrysene suggests that this compound could be of hormonal origin. Comparable mass spectra for ants, their brood or insects could not be found in the literature.

For the peak at RT 25.3, a peak with m/z 258.2342 ($C_{19}H_{30}$) was found. Figure A 9.7 illustrates the comparison of the fragment ion peaks with the NIST library spectrum indicating an overall match of 73 %. The measured spectrum matches almost all fragments present in the library spectrum. Furthermore, a comparison of the mass spectrum with Ventura et al., 2008 confirms the proposed assignment.

A semi-quantitative evaluation of the detected perhydroxyrenes was conducted to compare the findings between the different sample types. The used synthetic air contains phenol (m/z 94.0419). By applying the same flow of synthetic air for each experiment the amount of phenol should be roughly the same. The ratio of the area of the m/z of phenol at RT 17.60 min (A) to the m/z of a particular perhydroxyrene (B) was calculated and compared for each measurement. As depicted in Figure 7.5 the gas phase of the Ants *T. nyl.* clearly contained the most perhydroxyrenes. The perhydroxyrene with the highest concentration is the one with the m/z 220.2191. This perhydroxyrene was almost absent in the other samples.

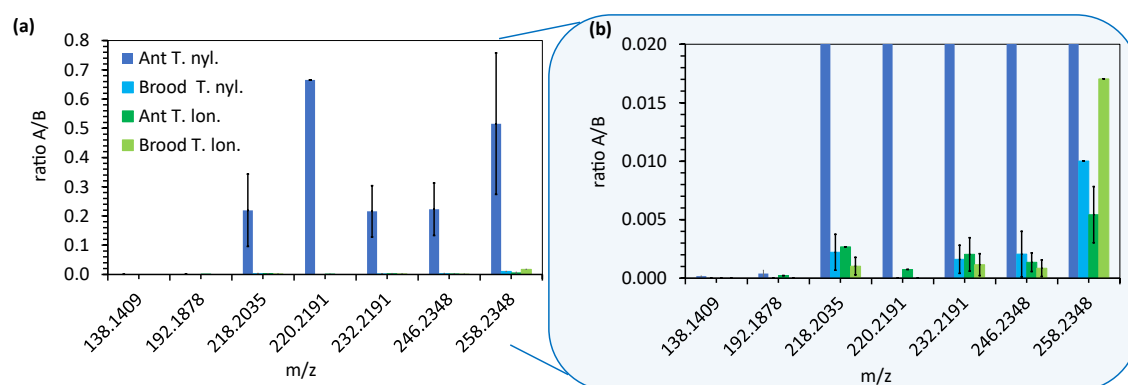


Figure 7.5 Semi-quantitative calculations of perhydroxyrenes by calculation of the ratio of the area of A (m/z 94.0419) and the area of B (m/z of perhydroxyrenes of ants and brood of *T. nyl* and *T. lon.*). The error bars represent the standard deviation resulting from the analysis conducted in triplicate. If no error bar is present, it indicates that the compound was detected fewer than three times.

If we zoom in the graph to smaller ratios, we obtain the graph in Figure 7.5 b) which shows that the perhydroxyrenes with the sum formula $C_{10}H_{18}$ (m/z 138.1409), $C_{14}H_{24}$ (m/z 192.1878), and $C_{16}H_{28}$ (m/z 220.2191), could not be detected in the brood of both species. It is possible that the concentration is either below the limit of detection, or the brood does not emit these substances. On the other hand, the ratios of the perhydroxyrenes with the masses $C_{16}H_{26}$ (m/z 218.2035), $C_{17}H_{28}$ (m/z 232.2191), and $C_{18}H_{30}$ (m/z 246.2348), are in a narrow range of concentrations for the samples of ants *T. lon.* and broods of both species.

In summary, this method can be applied to ants and their brood. The species Ant *T. nyl.* emits the most substances, possibly due to their habitat and other factors. Further investigations, combined with behavioral research, could provide reasons for the quantitative differences in the emitted gas phase. The substances found and their functions could also be determined through additional behavioral research. However, the biologically relevant origin of the identified perhydroxyrenes remains

undetermined. Nevertheless, there are hypothetical predictions about the origin. The most likely for insects is the hypothesis that these compounds are formed from fatty acids during diagenesis (Payzant, Rubinstein, Hogg, & Strausz, 1980; Rubinstein & Strausz, 1979)

Further improvements to the method would be to substitute the brass fittings and glass components with silanized, surface-deactivated fittings, tubes, and glass parts. Additionally, the synthetic air could be purified using liquid nitrogen.

7.4 Conclusions

For the first time, the gas phase emitted by living ants and their brood is measured. The developed method using a glass device enabled us to investigate the molecules emitted and exclude matrix effects. It is probable that these emitted molecules are used by the ants and the brood to communicate with each other. The class of detected perhydropyrenes appears to be biologically relevant. Their basic structures show similarities to hormones, pheromones and other molecules already known for biologically important processes. However, these measurements represent the first identification of these compounds in insects. Previously, they had only been detected in sediments (Ventura et al., 2008). The developed method in combination with the high-resolution TD-GC-MS technique can help to identify further gas phase compounds emitted by insects to better understand their metabolism and communication.

8 Summary and outlook

This work focused on the development of analytical techniques in the field of trace analysis, more precisely in the field of nanometer aerosol particles and volatile molecules in the gas phase of biological samples. The reaction conditions of particles in the nanometer range, in particular the influence of pressure and size growth, were investigated and a model system developed. This will be used to investigate further reactions in aerosol particles. In addition, a self-built TD was further improved, and a versatile TD injector was developed and built. The versatile TD injector was used in this thesis to study chemical ecology. The chemical communication through the gas phase between living ants and their brood was investigated.

In the first part of the work, a new modeling system was developed to carry out size-dependent reactions in nanometer-sized aerosol particles in the laboratory. The Diels-Alder reaction was used, in which a diene and a dienophile undergo a reaction. This reaction was chosen because it preferably takes place under pressure or is thus accelerated. A glass tube and a modified TDMA set-up were developed. A monodisperse aerosol was produced from one of the dienophilic reactants. The aerosol was mixed with the diene in the gas phase in the flow tube. The monodisperse particles were shown to grow as a result of the reaction. Aerosol particles of 30, 60 and 90 nm were selected for the reaction. The 30 nm aerosol particles grew the most. When analyzing the product aerosol of the diene, no reactive dienophile could be detected, but the product of the Diels-Alder reaction could be detected. A comparison of the calculated reaction rates with literature values for Diels-Alder reactions under laboratory conditions and increased pressure showed that the reaction rate in the particle is increased by a factor of up to eight orders of magnitude. These results show that the developed experimental setup and method are suitable for investigating further reactions in aerosol nanometer particles. Further investigations should focus specifically on the effects of the individual parameters. In addition, the system should be modeled to explain the measured parameters. An analysis with the newly developed versatile TD could lower the detection limit and identify possible by-products. Finally, efforts should be made to exclude possible condensation or coagulation of aerosol particles.

The second part of this work focused on the improvement of an in-house TD injector and the development of a new, versatile TD injector. The in-house TD injector was

improved, e.g. the temperature of the focusing trap was increased. In addition, the safety and accuracy of the in-house TD injector was improved by installing a temperature sensor in the heater. However, the in-house TD injector required a new design in terms of hardware, software and user-friendliness. The newly developed, versatile TD injector has a modular and robust design that allows easy assembly and disassembly of all components, ensuring the ease of maintenance, versatility and expandability required in a university research environment. The performance of the system was tested through trials including analysis of volatile and semi-volatile compounds. The results showed successful desorption, minimal carryover and reproducible retention times, demonstrating the reliability of the injector for analytical applications. Although automation could be implemented and possibly improve reproducibility, the manual operation shown in this study already provides satisfactory results. Furthermore, it is possible to make the versatile TD injector more robust against leaks by installing a different split. Overall, the developed versatile TD injector has the potential to improve the analysis of trace substances in different sample matrices.

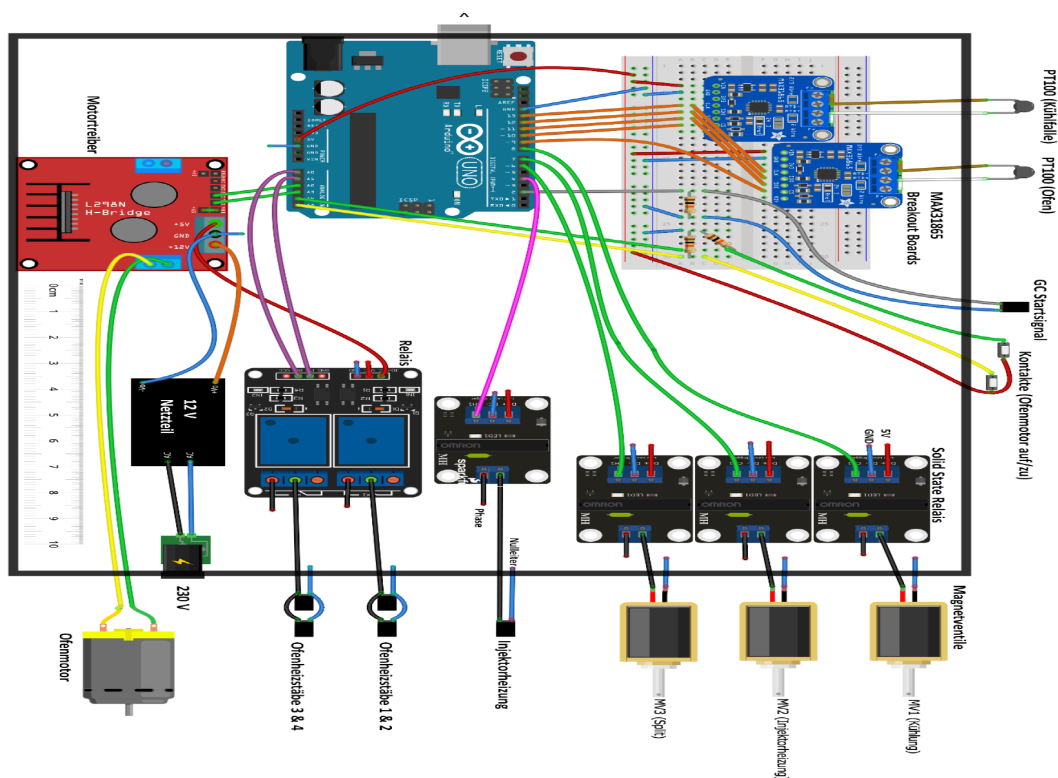
In the third part of this work, a novel method for detecting the volatile gas phase emitted by live ants and their brood was presented. In the non-invasive method, the ants and their brood were placed in a developed glass device. With the help of synthetic air, samples were taken into an adsorption tube. The developed versatile TD injector and the high-resolution GC-Orbitrap-MS were used for the subsequent analysis and enabled the identification and determination of the emitted molecules of the ants and their brood. The ant species *Temnothorax nylanderii* and *Temnothorax longispinosus* were investigated, revealing differences not only between the species but also between ants and brood. The ants of the species *Temnothorax nylanderii* emitted the largest number of substances. Perhydropyrenes were detected in all samples analyzed. These compounds have a structural similarity to hormones, pheromones and other molecules involved in biological processes, making them of potential biological interest. Their volatility suggests that they could serve as a potential communication medium between ants and their brood. The applied method can potentially be used to identify other gas-phase compounds. The use of synthetic air with a purity greater than 5.0 should provide background measurements with fewer signals in the future. This method should also be applied to other insects or microorganisms to extend our understanding of their metabolism and communication. To enhance compound analysis, it is recommended to use chemical ionization in addition to electron ionization.

9 Appendix

9.1 In-house TD - previous state

Hardware

Structure of the control electronics from Simon Probst (Probst, 2018)



frt:

Software

The entire program code of the Arduino from Simon Probst (Probst, 2018)

```
1 #include <Adafruit_MAX31865.h>
2 // Use software SPI: CS, DI, DO, CLK
3 // Adafruit_MAX31865 max = Adafruit_MAX31865(10, 11, 12, 13);
4 // use hardware SPI, just pass in the CS pin
5 Adafruit_MAX31865 max1 = Adafruit_MAX31865(10);
6 Adafruit_MAX31865 max2 = Adafruit_MAX31865(9);
7 // The value of the Ref resistor. Use 430.0 for PT100 and 4300.0 for PT1000
8 #define RREF 430.0
9 // The 'nominal' 0-degrees-C resistance of the sensor
10 // 100.0 for PT100, 1000.0 for PT1000
11 #define RNOMINAL 100.0
```

```
12 /*****
13 This is example LINX firmware for use with the Arduino Uno with the serial interface
14 enabled.
15 **** For more information see: www.LabVIEWmakerhub.com/linx
16 ** For support visit the forums at: www.LabVIEWmakerhub.com/forums/linx
17 **** Written By Sam Kristoff
18 **** BSD2 License.
19 *****/
19 //Include All Peripheral Libraries Used By LINX
20 #include <SPI.h>
21 #include <Wire.h>
22 #include <EEPROM.h>
23 #include <Servo.h>
23 //Include Device Specific Header From Sketch>>Import Library (In This Case
24 LinxChipkitMax32.h)
25 //Also Include Desired LINX Listener From Sketch>>Import Library (In This Case
26 LinxSerialListener.h)
27 #include <LinxArduinoUno.h>
28 #include <LinxSerialListener.h>
29 //Create A Pointer To The LINX Device Object We Instantiate In Setup()
30 LinxArduinoUno* LinxDevice;
31 int temp1;
32 float temp1a;
33 int temp2;
34 float temp2a;
35 int myCustomCommand1();
36 int myCustomCommand2();
37 //Initialize LINX Device And Listener
38 void setup()
39 {
40 //Instantiate The LINX Device
41 LinxDevice = new LinxArduinoUno();
42 //The LINXT Listener Is Pre Instantiated, Call Start And Pass A Pointer To The LINX 43
43 Device And The UART Channel To Listen On
44 LinxSerialConnection.Start(LinxDevice, 0);
45 LinxSerialConnection.AttachCustomCommand(0, myCustomCommand0);
46 LinxSerialConnection.AttachCustomCommand(1, myCustomCommand1);
47 max1.begin(MAX31865_2WIRE);
48 max2.begin(MAX31865_2WIRE);
49 }
50 void loop()
51 {
52 //Listen For New Packets From LabVIEW
53 LinxSerialConnection.CheckForCommands();
54 //Your Code Here, But It will Slow Down The Connection With LabVIEW
55 }
56 int myCustomCommand0(unsigned char numInputBytes, unsigned char* input,
57 unsigned char* numResponseBytes, unsigned char* response)
```

```

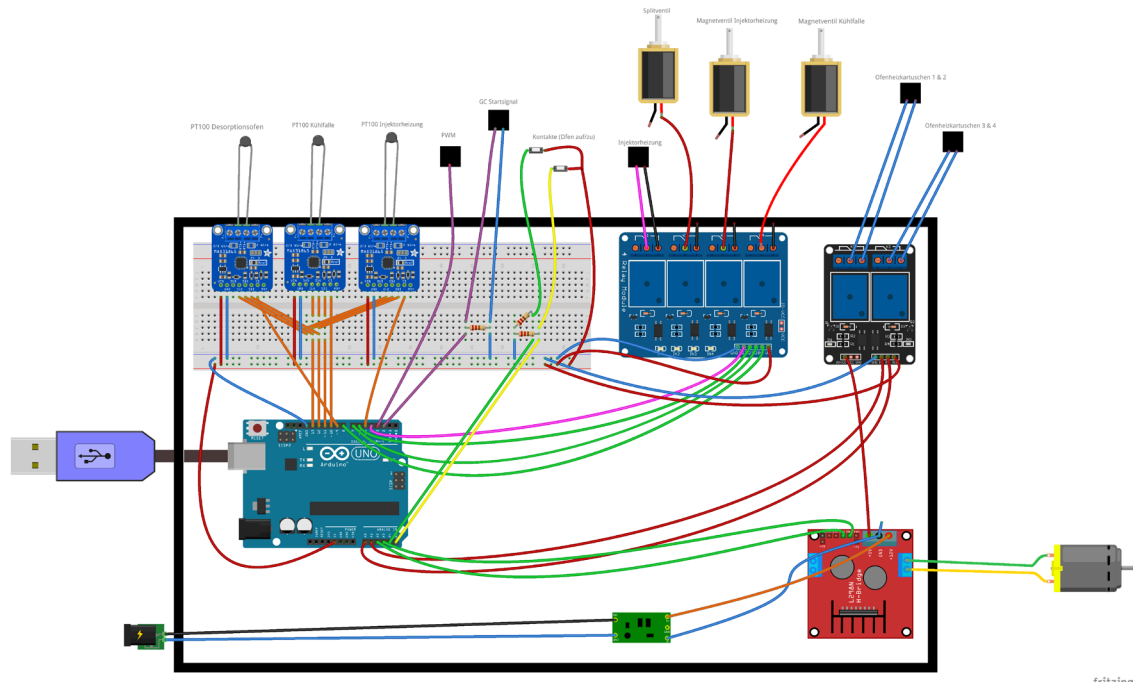
58 {
59 temp1a = max1.temperature(RNOMINAL, RREF);
60 temp1 = (temp1a + 210) * 100;
61 response[0] = (char)(temp1 >> 8);
62 response[1] = (char)(temp1 & 0xFF);
63 *numResponseBytes = 2;
64 return 0;
65 }
66 int myCustomCommand1(unsigned char numInputBytes, unsigned char* input,
67 unsigned char* numResponseBytes, unsigned char* response)
68 {
69 temp2a = max2.temperature(RNOMINAL, RREF);
70 temp2 = (temp2a + 210) * 100;
71 response[0] = (char)(temp2 >> 8);
72 response[1] = (char)(temp2 & 0xFF);
73 *numResponseBytes = 2;
74 return 0;
75 }

```

9.2 In-house TD – implementation

Hardware

Extended design of the control electronics with an additionally installed third temperature sensor for heating the focusing trap and replacement of one of the relays (Schmidt, 2021).



Software

The entire program code of the Arduino from Daniel Schmidt (Schmidt, 2021).

1/*

```
2 * Author: Daniel Schmidt
3 * Last Update: 04.06.2021
4 */
5
6 // Die notwendigen Libraries fuer Linx importieren
7 #include <LinxArduinoUno.h>
8 #include <LinxSerialListener.h>
9
10 // Pointer zu einem LinxDevice-Objekt erstellen, das in setup() initialisiert wird
11 LinxArduinoUno* LinxDevice;
12
13 // Library fuer Adafruit Amplifier importieren
14 #include <Adafruit_MAX31865.h>
15
16 // Software SPI nutzen -> Nur der CS-Pin muss angegeben werden
17 Adafruit_MAX31865 oven = Adafruit_MAX31865(9); //TD-Ofen
18 Adafruit_MAX31865 cooling = Adafruit_MAX31865(10); //KF
19 Adafruit_MAX31865 injector = Adafruit_MAX31865(5); //Injektor
20
21 // Der Wert des RRef-Widerstands: 430.0 fuer PT100
22 #define RREF 430.0
23
24 // Der nominale Widerstand des Sensors bei 0 Grad Celsius: 100.0 fuer P100
25 #define RNOMINAL 100.0
26
27 // Floats fuer die ausgelesenen Werte deklarieren
28 float ovenTemp, coolingTemp, injectorTemp;
29
30 // Funktionen deklarieren
31 int readOvenTemperature();
32 int readCoolingTemperature();
33 int readInjectorTemperature();
34
35 void setup() {
36 // Das LinxDevice initialisieren
37 LinxDevice = new LinxArduinoUno();
38 // Der Linx-listener ist bereits initialisiert und muss nur noch gestartet werden
39 // sowie der UART (serielle) Kanal angegeben werden, ueber den
40 // kommuniziert werden soll
41 LinxSerialConnection.Start(LinxDevice, 0);
42
43 LinxSerialConnection.AttachCustomCommand(0, readOvenTemperature);
44 LinxSerialConnection.AttachCustomCommand(1, readCoolingTemperature);
45 LinxSerialConnection.AttachCustomCommand(2, readInjectorTemperature);
46 // ...
47 oven.begin(MAX31865_2WIRE);
48 cooling.begin(MAX31865_2WIRE);
49 injector.begin(MAX31865_2WIRE);
```

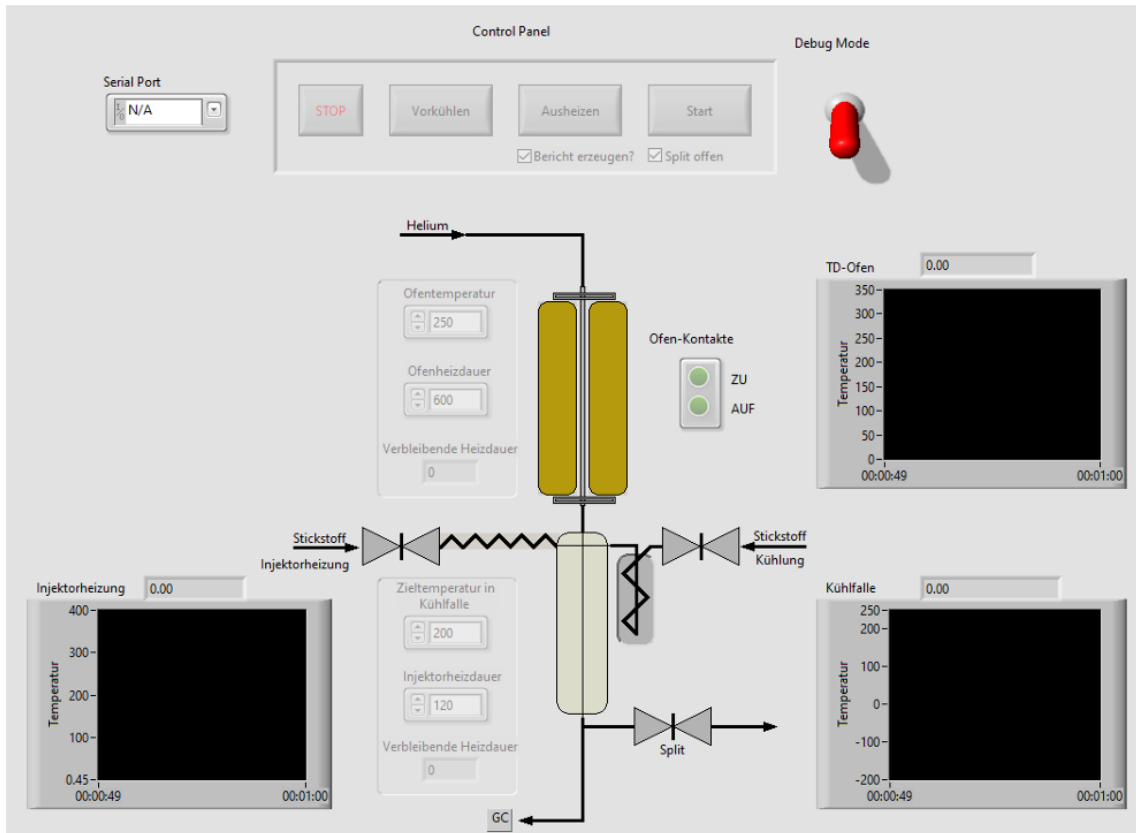
```

50 }
51
52 void loop() {
53 // Listen For New Packets From LabVIEW
54 LinxSerialConnection.CheckForCommands();
55 // Your code here, but it will slow down the connection with LabVIEW
56 }
57
58
59 // Custom Command zum Auslesen der Temperatur am Desorptions-Ofen
60 int readOvenTemperature(
61 unsigned char numInputBytes,
62 unsigned char* input,
63 unsigned char* numResponseBytes,
64 unsigned char* response
65 ) {
66 // Temperatur auslesen
67 ovenTemp = oven.temperature(RNOMINAL, RREF);
68
69 // Speicher fuer Char-Array allozieren
70 char ovenBuffer[RESPONSE_BYTES];
71
72 // Temperatur in Char-Array schreiben
73 dtostrf(ovenTemp, RESPONSE_BYTES-1, DECIMAL_PLACES, ovenBuffer);
74
75 // Jeden Char an entsprechende Stelle in Antwort schreiben
76 for (int i = 0; i < RESPONSE_BYTES; i++) {
77 response[i] = ovenBuffer[i];
78 }
79
80 // So viele Bytes werden zurueckgegeben
81 *numResponseBytes = RESPONSE_BYTES;
82 return 0;
83 }
84
85
86 // Custom Command zum Auslesen der Temperatur an der Kuehlfalle
87 int readCoolingTemperature(
88 unsigned char numInputBytes,
89 unsigned char* input,
90 unsigned char* numResponseBytes,
91 unsigned char* response
92 ) {
93 // Temperatur auslesen
94 coolingTemp = cooling.temperature(RNOMINAL, RREF);
95
96 // Speicher fuer Char-Array allozieren
97 char coolingBuffer[RESPONSE_BYTES];

```

```
98
99 // Temperatur in Char-Array schreiben
100 dtostrf(coolingTemp, RESPONSE_BYTES-1, DECIMAL_PLACES, coolingBuffer);
101
102 // Jeden Char an entsprechende Stelle in Antwort schreiben
103 for (int i = 0; i < RESPONSE_BYTES; i++) {
104 response[i] = coolingBuffer[i];
105 }
106
107 // So viele Bytes werden zurueckgegeben
108 *numResponseBytes = RESPONSE_BYTES;
109 return 0;
110 }
111
112
113 // Custom Command zum Auslesen der Temperatur an der Injektorheizung
114 int readInjectorTemperature(
115 unsigned char numInputBytes,
116 unsigned char* input,
117 unsigned char* numResponseBytes,
118 unsigned char* response
119 ) {
120 // Temperatur auslesen
121 injectorTemp = injector.temperature(RNOMINAL, RREF);
122
123 // Speicher fuer Char-Array allozieren
124 char injectorBuffer[RESPONSE_BYTES];
125
126 // Temperatur in Char-Array schreiben
127 dtostrf(injectorTemp, RESPONSE_BYTES-1, DECIMAL_PLACES, injectorBuffer);
128
129 // Jeden Char an entsprechende Stelle in Antwort schreiben
130 for (int i = 0; i < RESPONSE_BYTES; i++) {
131 response[i] = injectorBuffer[i];
132 }
133
134 // So viele Bytes werden zurueckgegeben
135 *numResponseBytes = RESPONSE_BYTES;
136 return 0;
137 }
```

Front panel of the finished software with now additional display of the temperature of the heating of the focusing trap.



9.3 Versatile TD

Hardware

TD oven	ENDA ET2011PID temperature controller
Transfer line	ENDA ET2011PID temperature controller
Coated metal capillary	SilcoNert 2000 CVD coated, SilcoTek® https://www.silcotek.com/coatings/silconert
Hot air soldering station	Digital SMD rework station- 320 W C-KOM ZD-939L
Focusing trap	Arduino uno Adafruit max 3165
	Flexible sampling tube for LN2, 1,800 mm, Cryoshop, CS - 2899231
	PT100-4-GE, Greisinger, temperature sensor, Nr. 22K1325, buerklin.com
Split	Vici Valco Tee 1/16, .50mm bore, SS, VC-ZT1M

Software

The following Arduino code was used to read the temperature of a PT 100 sensor in the focusing trap of the developed versatile TD injector using an Adafruit max 3165. The Arduino Uno was programmed using the Arduino IDE 2.0.3.

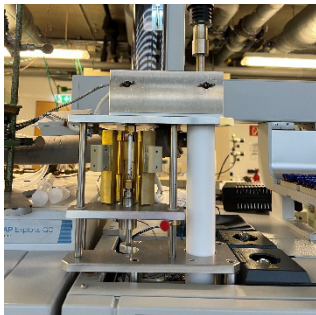
```
1 /*****
2 This is a library for the Adafruit PT100/P1000 RTD Sensor w/MAX31865
3 Designed specifically to work with the Adafruit RTD Sensor
4 ----> https://www.adafruit.com/products/3328
5 This sensor uses SPI to communicate, 4 pins are required to Interface
6 Adafruit invests time and resources providing this open source code,
7 please support Adafruit and open-source hardware by purchasing
8 products from Adafruit!
9 Written by Limor Fried/Ladyada for Adafruit Industries.
10 BSD license, all text above must be included in any redistribution
11 *****/
12 #include <Adafruit_MAX31865.h>
13 // Use software SPI: CS, DI, DO, CLK
14 Adafruit_MAX31865 thermo = Adafruit_MAX31865(10, 11, 12, 13);
15 // use hardware SPI, just pass in the CS pin
16 //Adafruit_MAX31865 thermo = Adafruit_MAX31865(10);
17 // The value of the Rref resistor. Use 430.0 for PT100 and 4300.0 for PT1000
18 #define RREF 4300.0
19 // The 'nominal' 0-degrees-C resistance of the sensor
20 // 100.0 for PT100, 1000.0 for PT1000
21 #define RNOMINAL 1000.0
22 void setup() {
23   Serial.begin(115200);
24   Serial.println("Adafruit MAX31865 PT100 Sensor Test!");
25   thermo.begin(MAX31865_2WIRE); // set to 2WIRE or 4WIRE as necessary
26 }
27 void loop() {
28   uint16_t rtd = thermo.readRTD();
29   Serial.print("RTD value: "); Serial.println(rtd);
30   float ratio = rtd;
31   ratio /= 32768;
32   Serial.print("Ratio = "); Serial.println(ratio,8);
33   Serial.print("Resistance = "); Serial.println(RREF*ratio,8);
34   Serial.print("Temperature = "); Serial.println(thermo.temperature(RNOMINAL,
35   RREF));
36   // Check and print any faults
37   uint8_t fault = thermo.readFault();
38   if (fault) {
39     Serial.print("Fault 0x"); Serial.println(fault, HEX);
40     if (fault & MAX31865_FAULT_HIGHTHRESH) {
41       Serial.println("RTD High Threshold");
42     }
43   }
44 }
```

```

43 if (fault & MAX31865_FAULT_LOWTHRESH) {
44 Serial.println("RTD Low Threshold");
45 }
46 if (fault & MAX31865_FAULT_REFINLOW) {
47 Serial.println("REFIN- > 0.85 x Bias");
48 }
49 if (fault & MAX31865_FAULT_REFINHIGH) {
50 Serial.println("REFIN- < 0.85 x Bias - FORCE- open");
51 }
52 if (fault & MAX31865_FAULT_RTDINLOW) {
53 Serial.println("RTDIN- < 0.85 x Bias - FORCE- open");
54 }
55 if (fault & MAX31865_FAULT_OVUV) {
56 Serial.println("Under/Over voltage");
57 }
58 thermo.clearFault();
59 }
60 Serial.println();
61 delay(1000);
62 }

```

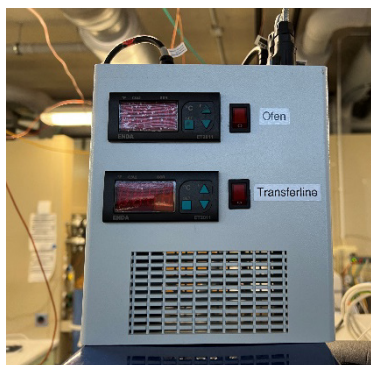
Pictures



Versatile TD injector



Control unit of the hot air soldering station: Front and back



Control unit of the TD oven control and transfer line



Rotameter for monitoring the helium gas flow of the split



Helium pressure control before TD

9.4 Supplements chapter 8

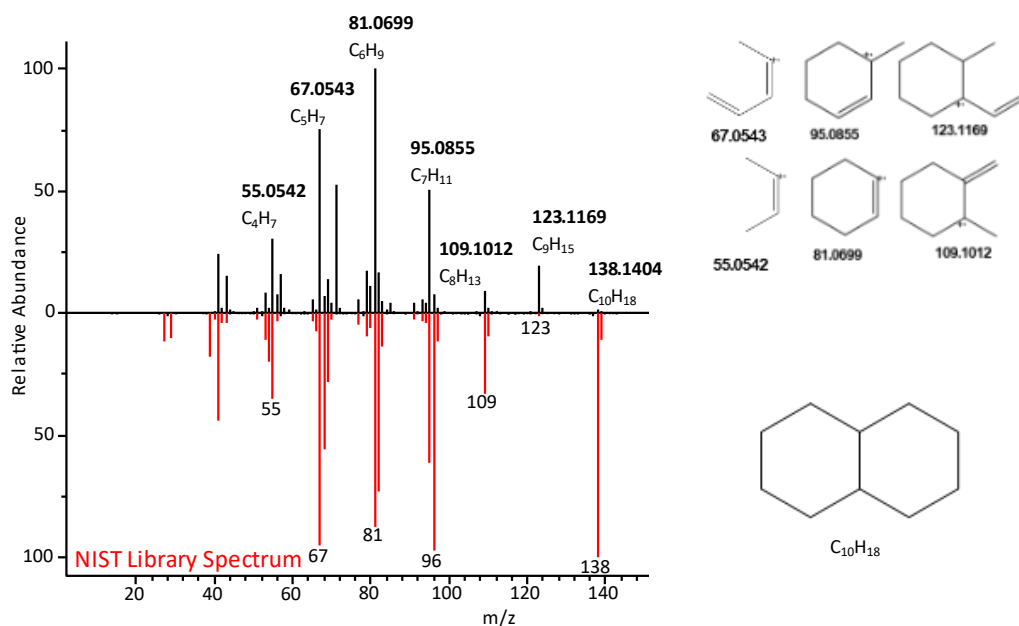


Figure A 9.1 The mass spectrum of compound $C_{10}H_{18}$ (black) in comparison to the NIST library spectrum of decahydronaphthalene (red). Six major fragments were identified with m/z values of 55.0542, 69.0543, 81.0699, 95.0855, 109.1012, and 123.1169. The proposed structures for each fragment were provided.

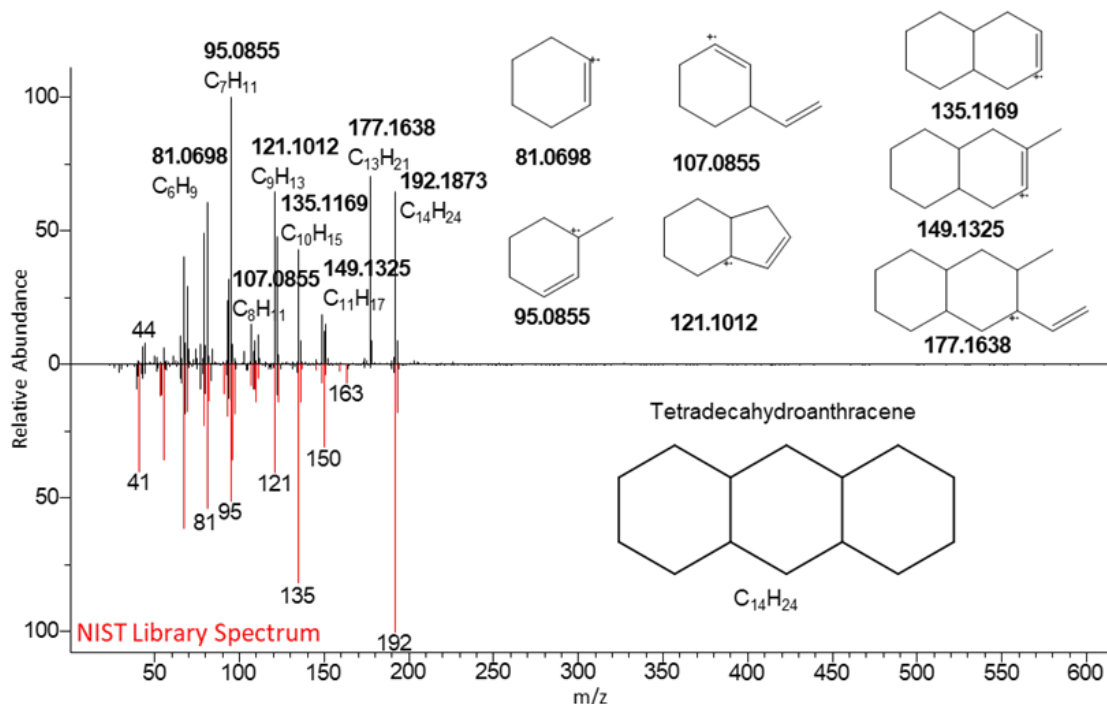


Figure A 9.2 The mass spectrum of compound $C_{14}H_{24}$ (black) in comparison to the NIST library spectrum of tetradecahydroanthracene (red). Seven major fragments were identified with m/z values of 81.0698, 95.0855, 107.0855, 121,1012, 135.1169, 149.1325, and 177.1638. The proposed structures for each fragment were provided.

1H-benz[f]indene, dodecahydro-1-methyl-

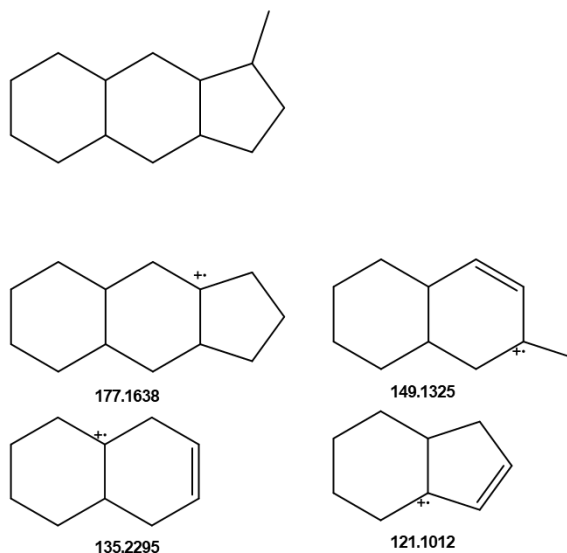


Figure A 9.3 The proposed structures for each of the four major fragments with m/z values of 121.1012, 135.1169, 149.1326, and 177.1638 of dodecahydro-1-methyl-1H-benz[f]indene ($C_{14}H_{24}$) were provided.

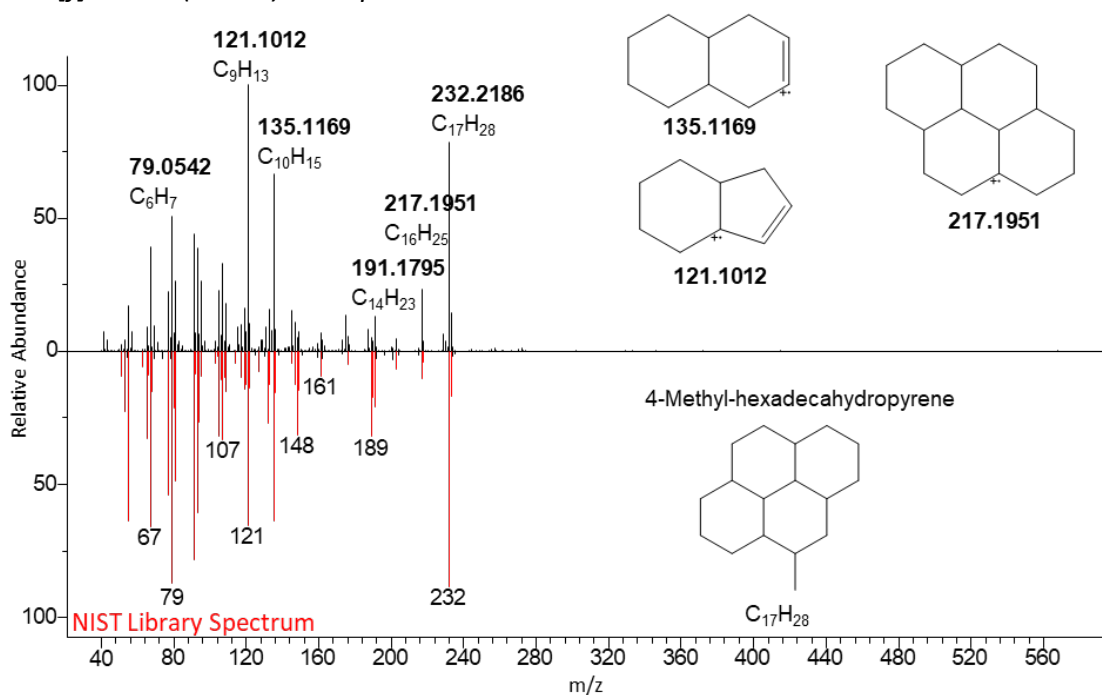


Figure A 9.4 The mass spectrum of compound $C_{17}H_{28}$ (black) in comparison to the NIST library spectrum of 4-methyl-hexadecahydropyrene (red). Three major fragments were identified with m/z values of 121.1012, 135.1169, and 217.1951. The proposed structures for each fragment were provided.

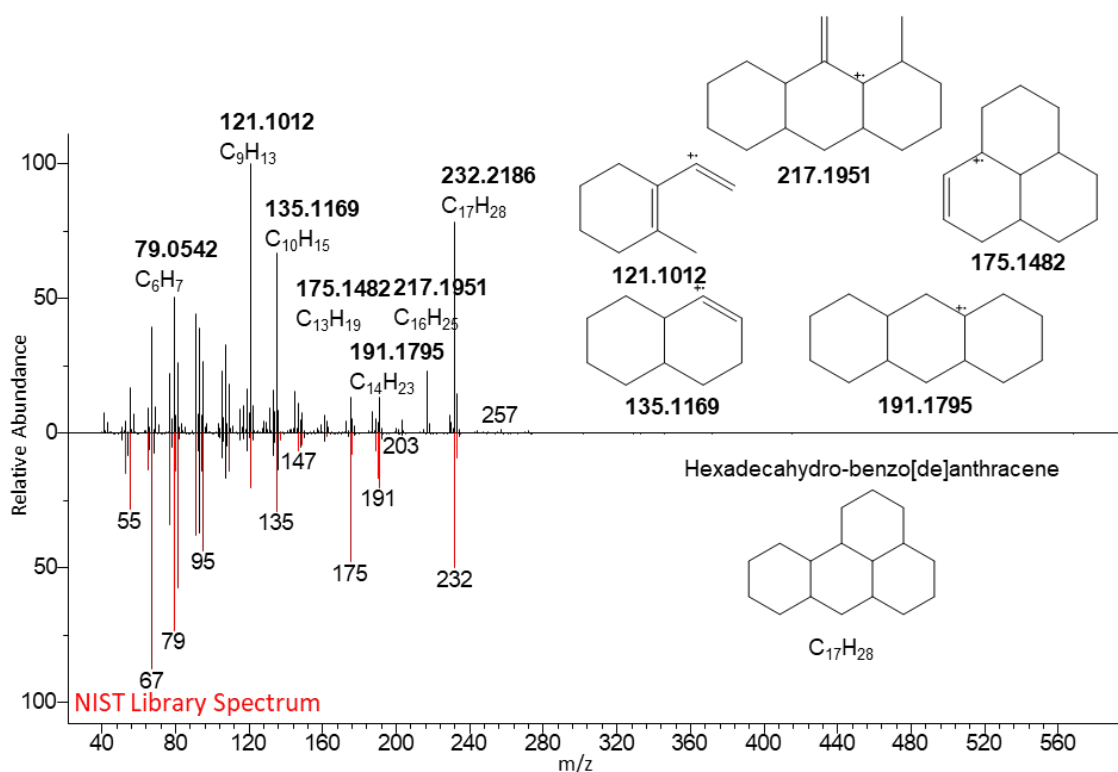


Figure A 9.5 The mass spectrum of compound $C_{17}H_{28}$ (black) in comparison to the NIST library spectrum of hexadecahydro-benzo[de]anthracene (red). The proposed structures for each of the five major fragments with m/z values of 121.1012, 135.1169, 175.1482, 191.1795, and 217.1951 were provided.

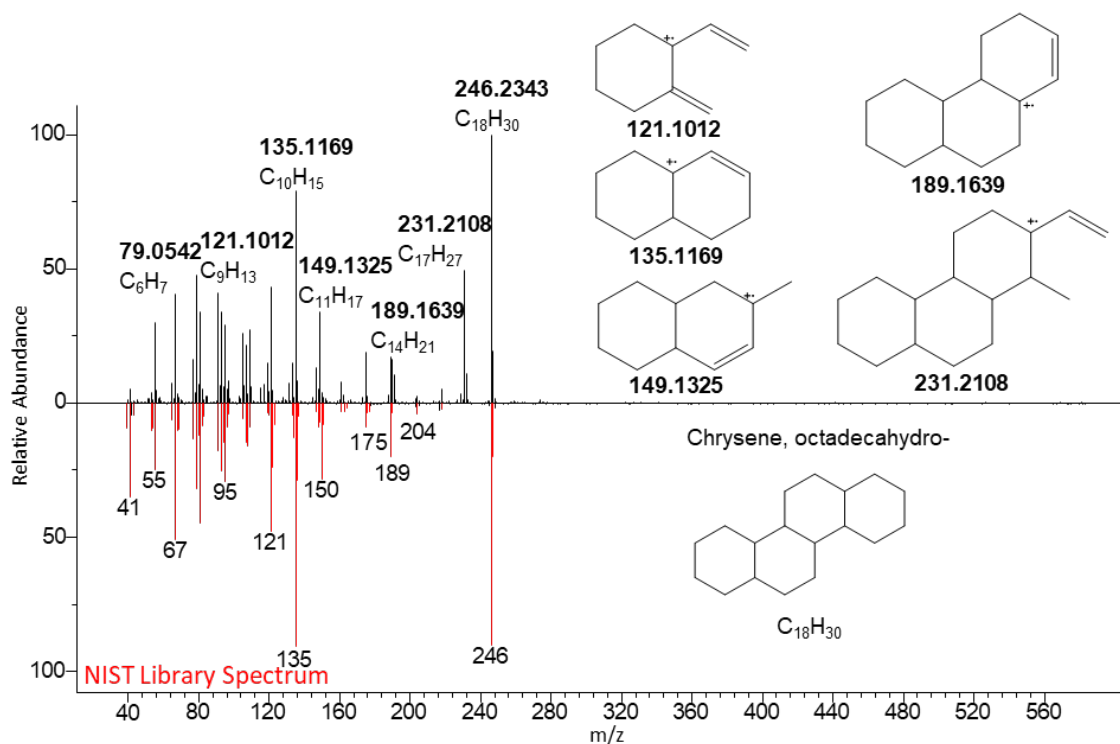


Figure A 9.6 The mass spectrum of compound $C_{18}H_{30}$ (black) in comparison to the NIST library spectrum of octadecahydro-chrysene (red). The proposed structures for each of

the five major fragments with m/z values of 121.1012, 135.1169, 149.1325, 189.1639, and 231.20108 were provided.

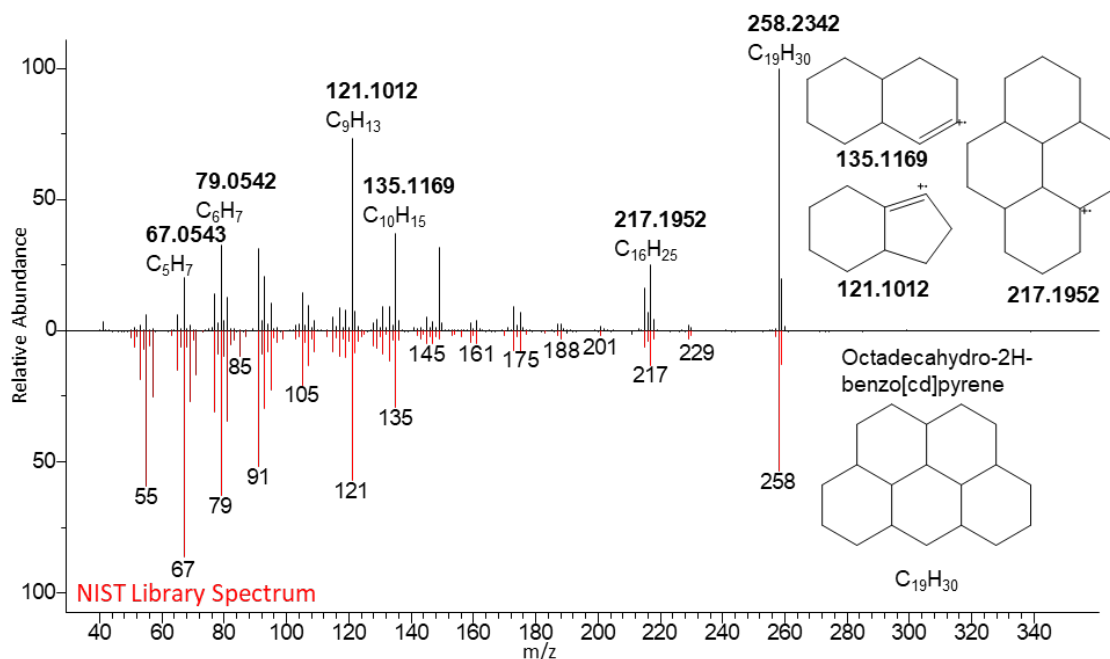


Figure A 9.7 The mass spectrum of compound $C_{19}H_{30}$ (black) in comparison to the NIST library spectrum of octadecahydro-2H-benzo[cd]pyrene (red). The proposed structures for each of the three major fragments with m/z values of 121.1012, 135.1169, and 217.1952 were provided.

10 List of symbols and abbreviations

Abbreviations

Å	Ångström ($1 \text{ Å} = 10^{-10} \text{ m}$)
BVOC	biogenic volatile organic compounds
CCN	cloud condensation nuclei
CHC	cuticular hydrocarbon
CPC	Condensation Particle Counter
C-Trap	curved linear trap
DC	direct current
DMA	Differential Mobility Analyzer
EPA	Environmental Protection Agency
EI	electron ionization
eV	electron volt
EPC	electronic pressure system
FTICR	Fourier-transform ion cyclotron resonance
FWHM	full width at half maximum
GC	gas chromatography
GF	growth factor
HOM	highly oxygenated organic molecules
HOMO	highest occupied molecular orbital
i. d.	inner diameter
IUPAC	International Union of Pure and Applied Chemistry
LUMO	lowest unoccupied molecular orbital
MBq	mega Becquerel
MFCS	material flow control System
min	minutes
MS	mass spectrometry
M	molecular weight
m/z	mass-to-charge ratio
μCi	micro Curie
NIST	National Institute of Standards and Technology
OPC	Optical Particle Counter
PID	proportional–integral–derivative
POC	particle-bound organic compounds
PWM	pulse-width modulation
R	mass resolution
RF	radio frequency
RT	retention time

s	seconds
SMPS	Scanning Mobility Particle Sizer
SOA	secondary organic aerosol
SVOC	semi-volatile organic compound
TD	thermal desorption
TDMA	Tandem Differential Mobility Analyzer
TIC	total ion current
UHRMS	Ultra-high resolution mass spectrometry
VOC	volatile organic compound
VVOC	very volatile organic compound
WCPC	Water-based Condensation Particle Counter
WHO	World Health Organization
Constants	
k_B	Boltzmann constant
R	universal gas constant
Symbols	
A, B	reactants
C	product
γ	surface tension
d^*	Kelvin diameter
ΔH_V	latent heat of evaporation
k	instrumental constant
k_p	reaction rate constant at high pressure p
k_0	reaction rate constant at reference pressure (1 bar)
K_R	Kelvin ratio
k_p/k_0	rate enhancement factor
p_d	partial vapor pressure at droplets surface
p_s	saturation vapor pressure
ρ	density
r	rate of a chemical reaction
r_p	particle radius
r_p^*	Kelvin radius
S_R	saturation ratio
t	reaction time
T	temperature
ν_a, ν_b, ν_c	stoichiometric coefficients of reactants and product
ν_v	molar volumes of vapor
ν_l	molar volumes of liquid
ΔV^\ddagger	activation volume
ΔV	reaction volume

V^\ddagger	volume of transition state
V_R	molar volume of the reactants
V_P	molar volume of the products
ω	frequency of the harmonic oscillation
z	cylindrical coordinate

11 List of tables

Table 1.1 Classification of volatile organic compounds (VOCs) from the World Health Organization (WHO) adapted from Vera et al., 2022b.	13
Table 4.1 Theoretical growth factors were calculated for the educt and product aerosols of 30 nm particles, assuming an ideal spherical shape. The calculations were based on molecular weight, density, mass per particle, molar mass per particle, molecules per particle, radius, and volume of the particle.....	53
Table 5.1 Overview of the initial state, implementations and outlook of the thermal desorption injector.....	65
Table 7.1 Structures, mass-to-charge ratio (m/z), ^{13}C mass-to-charge ratio, retention time (RT), and occurrence in ants and brood of the respective perhydropyrene species found.....	85

12 List of figures

- Figure 1.1 The illustration shows the nucleation and growth of the atmospheric nucleation of H_2SO_4 and H_2O . First, stable water clusters are formed, then low-volatile compounds can participate in the growth. When these reach a certain size, cloud condensation nuclei can evolve to form cloud droplets. In this work, the marked range of approx. 2 to 100 nm was investigated. Drawing adapted from Curtius, 2006.....5
- Figure 1.2 The surface tensions used were 0.080 N m^{-1} for aqueous salts, 0.072 N m^{-1} for water, and 0.030 N m^{-1} for organic compounds. The graph, adapted from Sarah S. Petters, 2022, illustrates the relationship between particle internal pressure and diameters ranging from 3 to 500 nm.....7
- Figure 1.3 Volumes of reaction (ΔV) and activation (ΔV^\ddagger) adapted from Klärner and Wurche, (2000).8
- Figure 1.4 Schematic illustration of the Diels-Alder reaction. Modified from Clayden et al., 2012.9
- Figure 1.5 Drawing of the frontier orbital description of the Diels-Alder reaction adapted from Clayden et al., 2012. It illustrated the energy levels of the HOMOs and LUMOs of a diene and acceptor substituted dienophile.10
- Figure 2.1 Drawing with dimensions of the build flow tube reactor used for the particle growth experiments.17
- Figure 2.2 This is a non-invasive device designed for sampling the gas phase of ants and their brood. The author took the accompanying picture.....18
- Figure 2.3 Operating Principle of TD injection coupled to a GC-MS adapted from Dettmer and Engewald, 2003.....19
- Figure 2.4 Outside and overview of the commercial TD injector UNITY-xr from Markes (Markes International Ltd., 2019b).....20
- Figure 2.5 The drawing, adapted from (Markes international Ltd., 2013), shows the gas flows during (1) Primary (tube) desorption and (2) Secondary (trap) desorption through the injector to the GC.21
- Figure 2.6 An image of the home-built TD injector and the Arduino controller with an illustration of the system components adapted from Münz, (2010) is displayed. .22
- Figure 2.7 overview drawing of the system components and on the right the gas flows during (1) Primary (tube) desorption and (2) Secondary (trap) desorption through the injector to the GC.23

Figure 2.8 The image on the left shows the Versatile TD injector, while the view on the right displays the entire system, including control systems and installation on the GC-MS.....	24
Figure 2.9 The drawing illustrates the system components, and the gas flows during (1) primary (tube) desorption and (2) secondary (trap) desorption through the injector to the GC.....	25
Figure 2.10 Own picture of an inert coated stainless steel and glass adsorption tube from Markes with selected Teflon ferrules and brass nuts and fittings and information about the sorbents Carboxen 1000, Carbograph 1TD and Tenax TA.	26
Figure 2.11 Schematic working principle of an electron ionization source (Hoffmann 2013).....	28
Figure 2.12 Scheme of a three-dimensional ion trap. Own drawing after (E. de Hoffmann & Stroobant, 2007).....	29
Figure 2.13 Scheme of the Orbitrap Exploris GC mass spectrometer ion path. Adapted from the operating manual of the instrument (Fisher Scientific, 2022). Schematic drawing of an Orbitrap analyzer (Scigelova & Makarov, 2006).....	30
Figure 2.14 A CPC for butanol was drawn based on Spielvogel, 2009.	34
Figure 2.15 The WCPC used in this study is illustrated, adapted from the operation manual of the water-based condensation particle counter model 3789 (TSI Incorporated, 2019).	35
Figure 2.16 The illustration of the Nano DMA from TSI has been adapted from the operation and service manual of TSI (TSI Incorporated, 2016).	36
Figure 2.17 This is an exemplary working example of an aerosol neutralizer that is based on an Am ²⁴¹ source. The Am ²⁴¹ is an alpha emitter that ionizes the air molecules. The resulting positive charge changes the particles, allowing them to be classified electrostatically by the DMA. The source uses an intensity of 3.7 MBq, which is approximately 100 µCi. The picture and drawing have been adapted from Spielvogel, 2009.	37
Figure 2.18 Schematic of the TDMA setup. The diagram was created based on TSI Incorporated, (2016) and Joutsensaari et al., (2001).....	38
Figure 4.1 Reaction scheme of the Diels-Alder reaction with proposed transition state. The electron-rich diene cyclopentadiene 1 reacts in a concerted step with the electrophilic dienophile N-methylmaleimide 3 via a transition state to the product N-methyl-5-norbornene-2,3-dicarboximide 5	44
Figure 4.2 Diels-Alder-Reactions of used dienes cyclopentadiene 1 , 1,3-cyclohexadiene 2 , and dienophile N-methylmaleimide 3 with the nonreactive saturated educt N-	

methylsuccinimide 4 and the products N-methyl-5-norbornene-2,3-dicarboximide 5 , 3a,4,7,7a-tetrahydro-2-methyl-4,7-ethano-1H-isoindole-1,3(2H)-dione 6	45
Figure 4.3 Schematic of experimental setup for flow tube reactions and measurement of particle size.....	46
Figure 4.4 Calculated Laplace pressure at different particle diameter according Young-Laplace equation $\Delta p = 2\gamma/r$ assuming a liquid particle with the known surface tension γ for aqueous salts ($0.080 \text{ N}^{-3} \text{ m}^{-1}$), water ($0.072 \text{ N}^{-3} \text{ m}^{-1}$), organic ($0.030 \text{ N}^{-3} \text{ m}^{-1}$) and N-methylmaleimide 3 ($0.047 \text{ N}^{-3} \text{ m}^{-1}$) at 20 °C.	49
Figure 4.5 Measured particle size number concentration distribution aerosol particles initially classified at a diameter of 30 nm without and with the addition of the diene in the gas phase of (a) dienophile (blue curve) and after the reaction with cyclopentadiene 1 (blue dotted curve) compared to the saturated N-methylsuccinimide 4 (black curve) and with the addition of cyclopentadiene 1 (black dotted curve) and (b) of dienophile N-methylmaleimide 3 (orange curve) and after the reaction with 1,3-cyclohexadiene 2 (orange dotted curve) compared to the saturated N-methylsuccinimide 4 (black curve) and with the addition of 1,3-cyclohexadiene 2 (black dotted curve).....	51
Figure 4.6 Experimental particle growth factors (particle diameter change) for the investigated reaction system with the starting diameter of particles of 30, 60 and 90 nm of N-methylmaleimide 3 and N-methylsuccinimide 4 . In addition, the theoretical growth factors for the reactions to N-methyl-5-norbornene-2,3-dicarboximide 5 and 3a,4,7,7a-tetrahydro-2-methyl-4,7-ethano-1H-isoindole-1,3(2H)-dione 6 are shown.	52
Figure 4.7 Experimental reaction rate constants of the investigated reactions N-methyl-5-norbornene-2,3-dicarboximide 5 (blue circle) and 3a,4,7,7a-tetrahydro-2-methyl-4,7-ethano-1H-isoindole-1,3(2H)-dione 6 (orange square) with the starting diameter of particles of 30, 60 and 90 nm. Experimental reaction rate constants were calculated by using equation (4.3) and (4.4).	55
Figure 4.8 Relationship between reaction rate enhancement factor and pressure under particle reaction conditions of investigated reactions with N-methyl-5-norbornene-2,3-dicarboximide 5 (blue) and 3a,4,7,7a-tetrahydro-2-methyl-4,7-ethano-1H-isoindole-1,3(2H)-dione 6 (orange) as products and normal reaction conditions for DA reactions (black).....	56
Figure 5.1 Scheme of the heater cartridge adapted from HS-Heizelemente.	61
Figure 5.2 Wiring of the KEMO M012 and the KEMO M150 for controlling the injector heating using pulse width modulation. Adapted from the KEMO M150 manual (Kemo Electronic GmbH)	61

Figure 5.3 Self designed injector heater for heating the focusing trap. Drawing adapted from JGU's precision engineering workshop.	62
Figure 5.4 These are LabVIEW implementations of equation 5.1 adapted from Schmidt, (2021).	64
Figure 6.1 (1) Overview of the developed TD injector. (2) Flow path scheme of the analyte through the GC. (3) Technical drawing of the TD injector.	71
Figure 6.2 Schematic drawing of the TD injector focusing on the gas flow.	74
Figure 6.3 Graph of increase of temperature during the heating period of the cold trap to inject the focused sample to the GC-MS.	75
Figure 6.4 Extracted ion chromatogram (EIC) of the 1 ppm Standard N-MND solution spiked on an adsorption tube to check for complete desorption and carryover of semi-volatiles. (1) shows the EIC of the first measurement and (2) shows the EIC of the second measurement directly after the first measurement.	76
Figure 6.5 Chromatograms from three different measurements demonstrating the reproducibility of retention time shifts.....	77
Figure 7.1 Developed glass device for the investigation of the emitted gas phase of ants and brood.	82
Figure 7.2 The mass spectrum of compound C ₁₆ H ₂₆ in comparison to the NIST library spectrum of hexadecahydro-pyrene (red). Four major fragments of m/z 121.1012, 135.1169, 177.1638, and 189.1638 were identified and their suggested structures were provided. The m/z values of 189 and 177, labelled with a red rectangle, highlight the difference to the mass spectrum of hexadecahydro-indeno[2,1-a]indene and thus a higher agreement with the mass spectrum of hexadecahydro-pyrene, indicating that this structure is more likely to be present.	87
Figure 7.3 The mass spectrum of compound C ₁₆ H ₂₆ in comparison to the NIST library spectrum of hexadecahydro-indeno[2,1-a]indene. Three major fragments of m/z 121.1012, 135.1169, 177.1638, and were identified and their suggested structures were provided.	88
Figure 7.4 The mass spectrum of the molecular formula C ₁₆ H ₂₈ and its associated fragment ions were analyzed. Four major fragments were identified with m/z values of 109.1012, 135.1169, 149.1326 and 205.1952. The proposed structures for each fragment were provided.	89
Figure 7.5 Semi-quantitative calculations of perhydro-pyrenes by calculation of the ratio of the area of A (m/z 94.0419) and the area of B (m/z of perhydro-pyrenes of ants and brood of T. nyl and T. lon.). The error bars represent the standard deviation	

- resulting from the analysis conducted in triplicate. If no error bar is present, it indicates that the compound was detected fewer than three times.90
- Figure A 9.1 The mass spectrum of compound $C_{10}H_{18}$ (black) in comparison to the NIST library spectrum of decahydronaphthalene (red). Six major fragments were identified with m/z values of 55.0542, 69.0543, 81.0699, 95.0855, 109.1012, and 123.1169. The proposed structures for each fragment were provided.....104
- Figure A 9.2 The mass spectrum of compound $C_{14}H_{24}$ (black) in comparison to the NIST library spectrum of tetradecahydroanthracene (red). Seven major fragments were identified with m/z values of 81.0698, 95.0855, 107.0855, 121.1012, 135.1169, 149.1325, and 177.1638. The proposed structures for each fragment were provided.....104
- Figure A 9.3 The proposed structures for each of the four major fragments with m/z values of 121.1012, 135.1169, 149.1326, and 177.1638 of dodecahydro-1-methyl-1H-benz[f]indene ($C_{14}H_{24}$) were provided.105
- Figure A 9.4 The mass spectrum of compound $C_{17}H_{28}$ (black) in comparison to the NIST library spectrum of 4-methyl-hexadecahydropyrene (red). Three major fragments were identified with m/z values of 121.1012, 135.1169, and 217.1951. The proposed structures for each fragment were provided.....105
- Figure A 9.5 The mass spectrum of compound $C_{17}H_{28}$ (black) in comparison to the NIST library spectrum of hexadecahydro-benzo[de]anthracene (red). The proposed structures for each of the five major fragments with m/z values of 121.1012, 135.1169, 175.1482, 191.1795, and 217.1951 were provided.106
- Figure A 9.6 The mass spectrum of compound $C_{18}H_{30}$ (black) in comparison to the NIST library spectrum of octadecahydro-chrysene (red). The proposed structures for each of the five major fragments with m/z values of 121.1012, 135.1169, 149.1325, 189.1639, and 231.20108 were provided.106
- Figure A 9.7 The mass spectrum of compound $C_{19}H_{30}$ (black) in comparison to the NIST library spectrum of octadecahydro-2H-benzo[cd]pyrene (red). The proposed structures for each of the three major fragments with m/z values of 121.1012, 135.1169, and 217.1952 were provided.107

13 Bibliography

- Abernathy, S. M., Berry, M. O., & Anderson, A. J. (2023). Calculating the Enthalpy of Vaporization of Ethanol, *n*-Heptane, Isooctane, and a Binary Mixture of Isooctane + *n*-Heptane from Their Vapor Pressure Data. *Accounts of Chemical Research*, 56(11), 1287–1294. doi: 10.1021/acs.accounts.2c00633
- Adams, R. M. M., Wells, R. L., Yanoviak, S. P., Frost, C. J., & Fox, E. G. P. (2020, March 13). Interspecific Eavesdropping on Ant Chemical Communication. *Frontiers in Ecology and Evolution*, Vol. 8. Frontiers Media S.A. doi: 10.3389/fevo.2020.00024
- Adamson, A. W., & Gast, A. P. (1997). *Physical Chemistry of Surfaces* (Vol. 6). Wiley.
- Agarwal, J., Rani, R., & Peddinti, R. (2017). Mechanochemical Grinding Diels–Alder Reaction: Highly Efficient and Rapid Access to Bi-, Tri-, and Tetracyclic Systems. *Synlett*, 28(11), 1336–1340. doi: 10.1055/s-0036-1558970
- Apsokardu, M. J., & Johnston, M. V. (2018). Nanoparticle growth by particle-phase chemistry. *Atmospheric Chemistry and Physics*, 18(3), 1895–1907. doi: 10.5194/acp-18-1895-2018
- Attygalle, A. B., & Morgan, E. D. (1984). Chemicals from the glands of ants. *The Royal Society of Chemistry London*, Vol. 13, pp. 245–278. doi: 10.1039/CS9841300245
- Barlin, M. R., Blum, M. S., & Brand, M. M. (1976). Fire ant trail pheromones: Analysis of species specificity after gas chromatographic fractionation. *Journal of Insect Physiology*, 22(6), 839–844. doi: 10.1016/0022-1910(76)90253-5
- Baron, P. A., Mazumder, M. K., Cheng, Y.-C., Peters, T. M., & Willeke, K. (2011). Real-Time Techniques for Aerodynamic Size Measurement. In K Willeke, P. A. Baron, & P. Kulkarni (Eds.), *Aerosol measurement: Principles, Techniques, and Applications* (3. ed., pp. 313–338). Hoboken, New Jersey: John Wiley & Sons, Inc.
- Bar-On, Y. M., Phillips, R., & Milo, R. (2018). The biomass distribution on Earth. *Proceedings of the National Academy of Sciences*, 115(25), 6506–6511. doi: 10.1073/pnas.1711842115
- Barsanti, K. C., McMurry, P. H., & Smith, J. N. (2009). The potential contribution of organic salts to new particle growth. *Atmospheric Chemistry and Physics*, 9(9), 2949–2957. doi: 10.5194/acp-9-2949-2009
- Becker, H. G. O. (2015). *Organikum: Organisch-chemisches Grundpraktikum* (24.). Weinheim: Wiley-VCH.

- Beros, S., Foitzik, S., & Menzel, F. (2017). What are the Mechanisms Behind a Parasite-Induced Decline in Nestmate Recognition in Ants? *Journal of Chemical Ecology*, 43(9), 869–880. doi: 10.1007/s10886-017-0880-6
- Böckmann, M. (2021). *Chemistry in aerosol particles UHPLC-HRMS studies on particle size-dependent chemical reactions in aerosol particles*.
- Boulay, R., Hefetz, A., Soroker, V., & Lenoir, A. (2000). Camponotus fellah colony integration: Worker individuality necessitates frequent hydrocarbon exchanges. *Animal Behaviour*, 59(6), 1127–1133. doi: 10.1006/anbe.2000.1408
- Brückner, R. (2002). *Advanced Organic Chemistry* (1st ed.). Elsevier. doi: 10.1016/B978-0-12-138110-3.X5000-4
- Butt, H.-J., Graf, K., & Kappl, M. (2006). *Physics and Chemistry of Interfaces*. Wiley-VCH.
- Cheng, Y., Su, H., Koop, T., Mikhailov, E., & Pöschl, U. (2015). Size dependence of phase transitions in aerosol nanoparticles. *Nature Communications*, 6. doi: 10.1038/NCOMMS6923
- Cheng, Y.-S. (2011). Condensation Particle Counters. In Klaus Willeke, P. Kulkarni, & P. A. Baron (Eds.), *Aerosol measurement: Principles, Techniques, and Applications: Vol. 3. ed.* (3. ed, pp. 381–392). Hoboken, New Jersey: Wiley.
- Clayden, J., Greeves, N., & Warren, S. (2012). *Organic Chemistry* (2nd ed.). Oxford University Press.
- Copernicus. (2023, November 8). Copernicus: October 2023 - Exceptional temperature anomalies; 2023 virtually certain to be warmest year on record. Retrieved March 4, 2024, from OCTOBER CLIMATE BULLETINS | NEWSFLASH website: <https://climate.copernicus.eu/copernicus-october-2023-exceptional-temperature-anomalies-2023-virtually-certain-be-warmest-year>
- Cremer, S., Sledge, M. F., & Heinze, J. (2002). Chemical mimicry: Male ants disguised by the queen's bouquet. *Nature*, 419(6910), 897–897. doi: 10.1038/419897a
- Curtius, J. (2006). Nucleation of atmospheric aerosol particles. *Comptes Rendus Physique*, 7(9–10), 1027–1045. doi: 10.1016/j.crhy.2006.10.018
- Dada, L., Lehtipalo, K., Kontkanen, J., Nieminen, T., Baalbaki, R., Ahonen, L., ... Kangasluoma, J. (2020). Formation and growth of sub-3-nm aerosol particles in experimental chambers. *Nature Protocols*, 15(3), 1013–1040. doi: 10.1038/s41596-019-0274-z
- David Morgan, E. (2009). Trail pheromones of ants. *Physiological Entomology*, 34(1), 1–17. doi: 10.1111/j.1365-3032.2008.00658.x

-
- de Gennes, P.-G., Brochard-Wyart, F., & Quéré, D. (2004). Capillarity and Wetting Phenomena. In *Capillarity and Wetting Phenomena*. New York, NY: Springer New York. doi: 10.1007/978-0-387-21656-0
- Dettmer, K., & Engewald, W. (2003). Ambient air analysis of volatile organic compounds using adsorptive enrichment. *Chromatographia*, 57(S1), S339–S347. doi: 10.1007/BF02492126
- Diels, O., & Alder, K. (1928). Synthesen in der hydroaromatischen Reihe. *Justus Liebigs Annalen Der Chemie*, 460(1), 98–122. doi: 10.1002/jlac.19284600106
- Diels, O., & Alder, K. (1929a). Synthesen in der hydroaromatischen Reihe. III. Mitteilung: Synthese von Terpenen, Camphern, hydroaromatischen und heterocyclischen Systemen. Mitbearbeitet von den Herren Wolfgang Lübbert, Erich Naujoks, Franz Querberitz, Karl Röhl, Harro Segeberg. *Justus Liebigs Annalen Der Chemie*, 470(1), 62–103. doi: 10.1002/jlac.19294700106
- Diels, O., & Alder, K. (1929b). Synthesen in der hydroaromatischen Reihe, IV. Mitteilung: Über die Anlagerung von Maleinsäure-anhydrid an arylierte Diene, Triene und Fulvene (Mitbearbeitet von Paul Pries). *Berichte Der Deutschen Chemischen Gesellschaft (A and B Series)*, 62(8), 2081–2087. doi: 10.1002/cber.19290620829
- DIN EN 13649:2002-05. (2020, May). *Stationary source emissions - Determination of the mass concentration of individual gaseous organic compounds - Activated carbon and solvent desorption method; German version EN 13649:2001*. Berlin: Beuth Verlag GmbH.
- Ding, L. C., Ke, F., Wang, D. K. W., Dann, T., & Austin, C. C. (2009). A new direct thermal desorption-GC/MS method: Organic speciation of ambient particulate matter collected in Golden, BC. *Atmospheric Environment*, 43(32), 4894–4902. doi: 10.1016/j.atmosenv.2009.07.016
- Donaldson, K., Li, X. Y., & MacNee, W. (1998). Ultrafine (nanometre) particle mediated lung injury. *Journal of Aerosol Science*, 29(5–6), 553–560. doi: 10.1016/S0021-8502(97)00464-3
- Dospinescu, V. M., Tiele, A., & Covington, J. A. (2020, July 1). Sniffing out urinary tract infection-diagnosis based on volatile organic compounds and smell profile. *Biosensors*, Vol. 10. MDPI. doi: 10.3390/BIOS10080083
- Drijfhout, F. P., Van Beek, T. A., Visser, J. H., & De Groot, A. (2000). On-line Thermal Desorption–Gas Chromatography of Intact Insects for Pheromone Analysis. *Journal of Chemical Ecology*, 26(6), 1383–1392. doi: 10.1023/A:1005427507048

- Drljaca, A., Hubbard, C. D., van Eldik, R., Asano, T., Basilevsky, M. V., & le Noble, W. J. (1998). Activation and Reaction Volumes in Solution. 3. *Chemical Reviews*, 98(6), 2167–2290. doi: 10.1021/cr970461b
- Duarte, R. M. B. O., Gomes, J. F. P., Querol, X., Cattaneo, A., Bergmans, B., Saraga, D., ... Villanueva, F. (2022). Advanced instrumental approaches for chemical characterization of indoor particulate matter. *Applied Spectroscopy Reviews*, 57(8), 705–745. doi: 10.1080/05704928.2021.2018596
- Dunn, J. D., Hodapp, D., Menzel, F., & Kohlmeier, P. (2024). Larval chemical cues induce rapid changes in foraging preferences of ant workers (Hymenoptera: Formicidae). *In Revision*.
- Dunne, E. M., Gordon, H., Kürten, A., Almeida, J., Duplissy, J., Williamson, C., ... Carslaw, K. S. (2016). Global atmospheric particle formation from CERN CLOUD measurements. *Science*, 354(6316), 1119–1124. doi: 10.1126/science.aaf2649
- Ehn, M., Thornton, J. A., Kleist, E., Sipilä, M., Junninen, H., Pullinen, I., ... Mentel, T. F. (2014). A large source of low-volatility secondary organic aerosol. *Nature*, 506(7489), 476–479. doi: 10.1038/nature13032
- Eldik, Rudi van., & Klärner, F.-Gerrit. (2002). *High Pressure Chemistry* (Rudi van Eldik & F. Klärner, Eds.). Wiley. doi: 10.1002/9783527612628
- Elorduy, I., Elcoroaristizabal, S., Durana, N., García, J. A., & Alonso, L. (2016). Diurnal variation of particle-bound PAHs in an urban area of Spain using TD-GC/MS: Influence of meteorological parameters and emission sources. *Atmospheric Environment*, 138, 87–98. doi: 10.1016/j.atmosenv.2016.05.012
- Ervens, B., Turpin, B. J., & Weber, R. J. (2011). Secondary organic aerosol formation in cloud droplets and aqueous particles (aqSOA): A review of laboratory, field and model studies. *Atmospheric Chemistry and Physics*, 11(21), 11069–11102. doi: 10.5194/ACP-11-11069-2011
- Even, M., Juritsch, E., & Richter, M. (2021). Measurement of very volatile organic compounds (VVOCs) in indoor air by sorbent-based active sampling: Identifying the gaps towards standardisation. *TrAC Trends in Analytical Chemistry*, 140, 116265. doi: 10.1016/j.trac.2021.116265
- Filipiak, W., Sponring, A., Filipiak, A., Ager, C., Schubert, J., Miekisch, W., ... Troppmair, J. (2010). TD-GC-MS Analysis of Volatile Metabolites of Human Lung Cancer and Normal Cells *In vitro*. *Cancer Epidemiology, Biomarkers & Prevention*, 19(1), 182–195. doi: 10.1158/1055-9965.EPI-09-0162

-
- Fisher Scientific, T. (2022). *Orbitrap Exploris GC and Orbitrap Exploris GC 240 Mass Spectrometers Operating Manual*.
- Flagan, R. C. (2011). Electrical Mobility Methods for Submicrometer Particle Characterization. In Klaus Willeke, P. Kulkarni, & P. A. Baron (Eds.), *Aerosol measurement: Principles, Techniques, and Applications* (3. ed., pp. 339–364). Hoboken, New Jersey: John Wiley & Sons, Inc.
- Flores, R. M., & Mertoglu, E. (2020). Optimization of a thermal desorption-gas chromatography/mass spectrometry method for characterization of semi-volatile organic compounds in high time resolved PM_{2.5}. *Atmospheric Pollution Research*, *11*(3), 619–629. doi: 10.1016/j.apr.2019.12.016
- Fuchs, N. A. (1963). On the stationary charge distribution on aerosol particles in a bipolar ionic atmosphere. *Geofisica Pura e Applicata*, *56*(1), 185–193. doi: 10.1007/BF01993343/METRICS
- Fuentes, J. D., Lerdau, M., Atkinson, R., Baldocchi, D., Bottenheim, J. W., Ciccioli, P., ... Stockwell, W. (2000). Biogenic Hydrocarbons in the Atmospheric Boundary Layer: A Review. *Bulletin of the American Meteorological Society*, Vol. 81, pp. 1537–1575. American Meteorological Society. doi: 10.1175/1520-0477(2000)081<1537:BHITAB>2.3.CO;2
- Funel, J., & Abele, S. (2013). Industrial Applications of the Diels–Alder Reaction. *Angewandte Chemie International Edition*, *52*(14), 3822–3863. doi: 10.1002/anie.201201636
- Gallego, E., Roca, F. J., Perales, J. F., & Guardino, X. (2011). Evaluation of the effect of different sampling time periods and ambient air pollutant concentrations on the performance of the Radiello® diffusive sampler for the analysis of VOCs by TD-GC/MS. *Journal of Environmental Monitoring*, *13*(9), 2612. doi: 10.1039/c1em10075k
- Gallego, Eva, Roca, F. J., Perales, J. F., & Guardino, X. (2011). Assessment of Chemical Hazards in Sick Building Syndrome Situations: Determination of Concentrations and Origin of VOCs in Indoor Air Environments by Dynamic Sampling and TD-GC/MS Analysis. In *Sick Building Syndrome* (pp. 289–333). Berlin, Heidelberg: Springer Berlin Heidelberg. doi: 10.1007/978-3-642-17919-8_16
- García-Lacuna, J., Domínguez, G., & Pérez-Castells, J. (2020). Flow Chemistry for Cycloaddition Reactions. *ChemSusChem*, *13*(19), 5138–5163. doi: 10.1002/cssc.202001372

- George, I. J., & Abbatt, J. P. D. (2010). Heterogeneous oxidation of atmospheric aerosol particles by gas-phase radicals. *Nature Chemistry*, 2(9), 713–722. doi: 10.1038/nchem.806
- Glaser, S. M., & Grüter, C. (2018). Ants (*Temnothorax nylanderi*) adjust tandem running when food source distance exposes them to greater risks. *Behavioral Ecology and Sociobiology*, 72(3). doi: 10.1007/s00265-018-2453-2
- Greene, M. J., & Gordon, D. M. (2003). Cuticular hydrocarbons inform task decisions. *Nature*, 423(6935), 32–32. doi: 10.1038/423032a
- Grosch, B., Orlebar, C. N., Herdtweck, E., Kaneda, M., Wada, T., Inoue, Y., & Bach, T. (2004a). Enantioselective [4+2]-Cycloaddition Reaction of a Photochemically Generated o-Quinodimethane: Mechanistic Details, Association Studies, and Pressure Effects. *Chemistry – A European Journal*, 10(9), 2179–2189. doi: 10.1002/CHEM.200306049
- Grosch, B., Orlebar, C. N., Herdtweck, E., Kaneda, M., Wada, T., Inoue, Y., & Bach, T. (2004b). Enantioselective [4+2]-Cycloaddition Reaction of a Photochemically Generated o-Quinodimethane: Mechanistic Details, Association Studies, and Pressure Effects. *Chemistry - A European Journal*, 10(9), 2179–2189. doi: 10.1002/chem.200306049
- Gross, J. H. (2013). Massenspektrometrie. In *Massenspektrometrie*. Berlin, Heidelberg: Springer Berlin Heidelberg. doi: 10.1007/978-3-8274-2981-0
- Grote, A. A., & Kennedy, E. R. (2002). Workplace monitoring for volatile organic compounds using thermal desorption-gas chromatography-mass spectrometry. *J. Environ. Monit.*, 4(5), 679–684. doi: 10.1039/B203000B
- Guarda, C., & Lutinski, J. A. (2020). Glandular Secretions of Ants (Hymenoptera: Formicidae): A Review on Extraction, Chemical Characterization and Antibiotic Potential. *Sociobiology*, 67(1), 13. doi: 10.13102/sociobiology.v67i1.4277
- Guenther, A. (2002). The contribution of reactive carbon emissions from vegetation to the carbon balance of terrestrial ecosystems. *Chemosphere*, 49(8), 837–844. doi: 10.1016/S0045-6535(02)00384-3
- Guenther, A., Hewitt, C. N., Erickson, D., Fall, R., Geron, C., Graedel, T., ... Zimmerman, P. (1995). A global model of natural volatile organic compound emissions. *Journal of Geophysical Research: Atmospheres*, 100(D5), 8873–8892. doi: 10.1029/94JD02950
- Guiffard, I., Geny, T., Veyrand, B., Marchand, P., Pellouin-Grouhel, A., Bizec, B. Le, & Bichon, E. (2020). Quantification of light polycyclic aromatic hydrocarbons in

-
- seafood samples using on-line dynamic headspace extraction, thermodesorption, gas chromatography tandem mass spectrometry, based on an isotope dilution approach. *Journal of Chromatography A*, 1619, 460906. doi: 10.1016/j.chroma.2020.460906
- Hallquist, M., Wenger, J. C., Baltensperger, U., Rudich, Y., Simpson, D., Claeys, M., ... Wildt, J. (2009). The formation, properties and impact of secondary organic aerosol: current and emerging issues. *Atmos. Chem. Phys*, 9, 5155–5236. Retrieved from www.atmos-chem-phys.net/9/5155/2009/
- Hämeri, K., Väkevä, M., Hansson, H. C., & Laaksonen, A. (2000). Hygroscopic growth of ultrafine ammonium sulphate aerosol measured using an ultrafine tandem differential mobility analyzer. *Journal of Geophysical Research Atmospheres*, 105(D17), 22231–22242. doi: 10.1029/2000JD900220
- Harris, D. C. (2014). *Lehrbuch der Quantitativen Analyse* (8th ed.; G. Werner & T. Werner, Eds.). Berlin, Heidelberg: Springer Berlin Heidelberg. doi: 10.1007/978-3-642-37788-4
- Hartmann, T. (2007). From waste products to ecochemicals: Fifty years research of plant secondary metabolism. *Phytochemistry*, 68(22–24), 2831–2846. doi: 10.1016/j.phytochem.2007.09.017
- Hart-Smith, G., & Blanksby, S. J. (2011). Mass Analysis. In *Mass Spectrometry in Polymer Chemistry* (pp. 5–32). Wiley. doi: 10.1002/9783527641826.ch1
- Hays, M. D., Smith, N. D., Kinsey, J., Dong, Y., & Kariher, P. (2003). Polycyclic aromatic hydrocarbon size distributions in aerosols from appliances of residential wood combustion as determined by direct thermal desorption—GC/MS. *Journal of Aerosol Science*, 34(8), 1061–1084. doi: 10.1016/S0021-8502(03)00080-6
- Hinds, W. C. (1999). *Aerosol Technology: Properties, Behavior, and Measurement of Airborne Particles* (2nd ed.). New York: John Wiley & Sons. Inc.
- Hoffmann, E. de, & Stroobant, V. (2007). Mass Spectrometry Principles and Applications. In <http://wr.vr.v.cem.msu.edu/~reusch/VirtualText/Spectrpy/MassS> p. (3 ed.). Chichester: Wiley.
- Hoffmann, T. (1992). *Entwicklung eines Verfahrens zur Messung luftgetragener biogener Kohlenwasserstoffe und seiner Anwendung zur Untersuchung von Emissionen und Abbau von Terpenen in Waldbeständen* (Dissertation). Universität Dortmund, Dortmund.
- Hoffmann, T. (2018). *Proposal for a Reinhart Koselleck Project: Chemistry in Nanometer Particles: Unique breeding sites for oligomers ?* (Vol. 49). Mainz.

- Hoffmann, T., Zetzsch, C., & Rossi, M. J. (2007). Chemie von Aerosolen. *Chemie in Unserer Zeit*, 41(3), 232–246. doi: 10.1002/ciuz.200700417
- Holmes, N. S. (2007). A review of particle formation events and growth in the atmosphere in the various environments and discussion of mechanistic implications. *Atmospheric Environment*, 41(10), 2183–2201. doi: 10.1016/j.atmosenv.2006.10.058
- Howard, R. W., & Blomquist, G. J. (2005). Ecological, behavioral, and biochemical aspects of insect hydrocarbons. *Annual Review of Entomology*, Vol. 50, pp. 371–393. doi: 10.1146/annurev.ento.50.071803.130359
- Hritz, A. D., Raymond, T. M., & Dutcher, D. D. (2016). A method for the direct measurement of surface tension of collected atmospherically relevant aerosol particles using atomic force microscopy. *Atmospheric Chemistry and Physics*, 16(15), 9761–9769. doi: 10.5194/acp-16-9761-2016
- Hu, Q., Noll, R. J., Li, H., Makarov, A., Hardman, M., & Cooks, R. G. (2005, April). The Orbitrap: A new mass spectrometer. *Journal of Mass Spectrometry*, Vol. 40, pp. 430–443. doi: 10.1002/jms.856
- Huang, R.-J., Hoffmann, T., Ovadnevaite, J., Laaksonen, A., Kokkola, H., Xu, W., ... O'Dowd, C. (2022). Heterogeneous iodine-organic chemistry fast-tracks marine new particle formation. *Proceedings of the National Academy of Sciences*, 119(32), e2201729119. doi: 10.1073/PNAS.2201729119
- Jang, M., Czoschke, N. M., Lee, S., & Kamens, R. M. (2002). Heterogeneous Atmospheric Aerosol Production by Acid-Catalyzed Particle-Phase Reactions. *Science*, 298(5594), 814–817. doi: 10.1126/science.1075798
- Jang, M., Ghio, A. J., & Cao, G. (2006). Exposure of BEAS-2B cells to secondary organic aerosol coated on magnetic nanoparticles. *Chemical Research in Toxicology*, 19(8), 1044–1050. doi: 10.1021/tx0503597
- Jenner, G. (1975). Hochdruck-kinetische Untersuchungen in der Organischen und Makromolekularen Chemie. *Angewandte Chemie*, 87(6), 186–194. doi: 10.1002/ange.19750870603
- John, W. (2011). Size Distribution Characteristics of Aerosols. In *Aerosol Measurement* (pp. 41–54). Wiley. doi: 10.1002/9781118001684.ch4
- Joutsensaari, J., Vaattovaara, P., Vestervinen, M., Hämeri, K., & Laaksonen, A. (2001). A novel tandem differential mobility analyzer with organic vapor treatment of aerosol particles. *Atmospheric Chemistry and Physics*, 1(1), 51–60. doi: 10.5194/acp-1-51-2001

-
- Juhl, M., & Tanner, D. (2009). Recent applications of intramolecular Diels-Alder reactions to natural product synthesis. *Chemical Society Reviews*, 38(11), 2983–2992. doi: 10.1039/b816703f
- Juillet, Y., Dubois, C., Bintein, F., Dissard, J., & Bossée, A. (2014). Development and validation of a sensitive thermal desorption-gas chromatography-mass spectrometry (TD-GC-MS) method for the determination of phosgene in air samples. *Analytical and Bioanalytical Chemistry*, 406(21), 5137–5145. doi: 10.1007/s00216-014-7809-5
- Kanakidou, M., Seinfeld, J. H., Pandis, S. N., Barnes, I., Dentener, F. J., Facchini, M. C., ... Wilson, J. (2005). Organic aerosol and global climate modelling: a review. *Atmospheric Chemistry and Physics*, 5(4), 1053–1123. doi: 10.5194/acp-5-1053-2005
- Kather, R., & Martin, S. J. (2015). Evolution of Cuticular Hydrocarbons in the Hymenoptera: a Meta-Analysis. *Journal of Chemical Ecology*, 41(10), 871–883. doi: 10.1007/s10886-015-0631-5
- Kemo Electronic GmbH. (n.d.). Manual circuit description M150 - DC + Puls Converter. *Description*. Geestland. Retrieved from www.kemo-electronic.de
- Kerminen, V. M., Chen, X., Vakkari, V., Petäjä, T., Kulmala, M., & Bianchi, F. (2018, September 27). Atmospheric new particle formation and growth: Review of field observations. *Environmental Research Letters*, Vol. 13. Institute of Physics Publishing. doi: 10.1088/1748-9326/aadf3c
- Kesselmeier, J., & Staudt, M. (1999). Biogenic Volatile Organic Compounds (VOC): An Overview on Emission, Physiology and Ecology. *Journal of Atmospheric Chemistry*, 33, 23–88. doi: <https://doi.org/10.1023/A:1006127516791>
- Kesselmeier, Jürgen, Ciccioli, P., Kuhn, U., Stefani, P., Biesenthal, T., Rottenberger, S., ... Andreae, M. O. (2002). Volatile organic compound emissions in relation to plant carbon fixation and the terrestrial carbon budget. *Global Biogeochemical Cycles*, 16(4), 73-1-73–79. doi: 10.1029/2001GB001813
- Kessler, A., & Baldwin, I. T. (2001). Defensive Function of Herbivore-Induced Plant Volatile Emissions in Nature. *Science*, 291(5511), 2141–2144. doi: 10.1126/science.291.5511.2141
- Kirkby, J., Duplissy, J., Sengupta, K., Frege, C., Gordon, H., Williamson, C., ... Curtius, J. (2016). Ion-induced nucleation of pure biogenic particles. *Nature*, 533(7604), 521–526. doi: 10.1038/nature17953

- Kiselev, V. D., Kashaeva, E. A., Shihab, M. S., Potapova, L. N., & Iskhakova, G. G. (2004). Diffusion control of the Diels–Alder reaction rate at elevated pressures. *Russian Chemical Bulletin*, 53(1), 45–50. doi: 10.1023/B:RUCB.0000024827.64458.0f
- Kiselev, Vladimir D., Konovalov, A. I., Asano, T., Kashaeva, E. A., Iskhakova, G. G., Shihab, M. S., & Medvedeva, M. D. (2001). Solvent effect on the volume of activation and volume of the Diels–Alder reaction. *Journal of Physical Organic Chemistry*, 14(9), 636–643. doi: 10.1002/POC.398
- Klärner, F.-G., & Wurche, F. (2000). The Effect of Pressure on Organic Reactions. *Journal Für Praktische Chemie*, 342(7), 609–636. doi: 10.1002/1521-3897(200009)342:7<609::AID-PRAC609>3.0.CO;2-Z
- Köhler, H. (1936). The nucleus in and the growth of hygroscopic droplets. *Trans. Faraday Soc.*, 32(0), 1152–1161. doi: 10.1039/TF9363201152
- Kolb, B. (1999). Headspace sampling with capillary columns. *Journal of Chromatography A*, 842(1–2), 163–205. doi: 10.1016/S0021-9673(99)00073-4
- Kolb, C. E., & Worsnop, D. R. (2012). Chemistry and Composition of Atmospheric Aerosol Particles. *Annual Review of Physical Chemistry*, 63(1), 471–491. doi: 10.1146/annurev-physchem-032511-143706
- Koppmann, Ralf. (2007). *Volatile Organic Compounds in the Atmosphere* (R. Koppmann, Ed.). Wiley. doi: 10.1002/9780470988657
- Korosi, G., & Kováts, E. S. (1981). Density and Surface Tension of 83 Organic Liquids. *Journal of Chemical and Engineering Data*, 26(3), 323–332. doi: 10.1021/JE00025A032/ASSET/JE00025A032.FP.PNG_V03
- Kousaka, Y., Niida, T., Okuyama, K., & Tanaka, H. (1982). Development of a mixing type condensation nucleus counter. *Journal of Aerosol Science*, 13(3), 231–240. doi: 10.1016/0021-8502(82)90064-7
- Krieger, J., & Breer, H. (1999). Olfactory Reception in Invertebrates. *Science*, 286(5440), 720–723. doi: 10.1126/science.286.5440.720
- Kulkarni, P., Baron, P. A. (Paul A., & Willeke, Klaus. (2011). *Aerosol Measurement* (P. Kulkarni, P. A. Baron, & K. Willeke, Eds.). Wiley. doi: 10.1002/9781118001684
- Kulmala, M., Petäjä, T., Ehn, M., Thornton, J., Sipilä, M., Worsnop, D. R., & Kerminen, V.-M. (2014). Chemistry of Atmospheric Nucleation: On the Recent Advances on Precursor Characterization and Atmospheric Cluster Composition in Connection with Atmospheric New Particle Formation. *Annual Review of Physical Chemistry*, 65(1), 21–37. doi: 10.1146/annurev-physchem-040412-110014

-
- Kulmala, M., Vehkamäki, H., Petäjä, T., Dal Maso, M., Lauri, A., Kerminen, V.-M., ... McMurry, P. H. (2004). Formation and growth rates of ultrafine atmospheric particles: a review of observations. *Journal of Aerosol Science*, *35*(2), 143–176. doi: 10.1016/j.jaerosci.2003.10.003
- Kulmala, Markku. (2003). How Particles Nucleate and Grow. *Science*, *302*(5647), 1000–1001. doi: 10.1126/science.1090848
- Laplace, P. S. marquis de. (1829). *Mécanique céleste* (Vol. 4). Boston, Hilard, Gray, Little, and Wilkins.
- Leonhardt, S. D., Menzel, F., Nehring, V., & Schmitt, T. (2016). Ecology and Evolution of Communication in Social Insects. *Cell*, *164*(6), 1277–1287. doi: 10.1016/J.CELL.2016.01.035
- Lewis, E. R. (2006). The effect of surface tension (Kelvin effect) on the equilibrium radius of a hygroscopic aqueous aerosol particle. *Journal of Aerosol Science*, *37*(11), 1605–1617. doi: 10.1016/J.JAEROSCI.2006.04.001
- Li, J., Peng, Y., & Duan, Y. (2013, July). Diagnosis of breast cancer based on breath analysis: An emerging method. *Critical Reviews in Oncology/Hematology*, Vol. 87, pp. 28–40. doi: 10.1016/j.critrevonc.2012.11.007
- Liu, H., & Cao, G. (2016). Effectiveness of the Young-Laplace equation at nanoscale. *Scientific Reports*, *6*. doi: 10.1038/SREP23936
- Marcolli, C. (2020). Technical note: Fundamental aspects of ice nucleation via pore condensation and freezing including Laplace pressure and growth into macroscopic ice. *Atmos. Chem. Phys*, *20*, 3209–3230. doi: 10.5194/acp-20-3209-2020
- Markes international Ltd. (2013). *Application Note 022: Selection of gas flows and split ratios during thermal desorption*. doi: AN022_5_261016
- Markes International Ltd. (2019a). *Application Note 021, Developing and optimising tube-based thermal desorption methods*.
- Markes International Ltd. (2019b). *User manual UNITY-xr: QUI-1119 Version 3.0, October 2019*. Retrieved from www.markes.com
- Maskill, H. (2006). The Investigation of Organic Reactions and Their Mechanisms. In H. Maskill (Ed.), *The Investigation of Organic Reactions and Their Mechanisms*. Wiley. doi: 10.1002/9780470988671
- Mcalary, T. A. (2014). *Demonstration and Validation of the Use of Passive Samplers for Monitoring Soil Vapor Intrusion to Indoor Air*. Retrieved from <http://hdl.handle.net/10012/8643>

- McCabe, J. R., & Eckert, C. A. (1974). Role of high-pressure kinetics in studies of the transition states of Diels-Alder reactions. *Accounts of Chemical Research*, 7(8), 251–257. doi: 10.1021/ar50080a003
- Meijer, A., Otto, S., & Engberts, J. B. F. N. (1998). Effects of the hydrophobicity of the reactants on Diels-Alder reactions in water. *Journal of Organic Chemistry*, 63(24), 8989–8994. doi: 10.1021/jo981359x
- Menzel, F., Blaimer, B. B., & Schmitt, T. (2017). How do cuticular hydrocarbons evolve? Physiological constraints and climatic and biotic selection pressures act on a complex functional trait. *Proceedings of the Royal Society B: Biological Sciences*, 284(1850). doi: 10.1098/rspb.2016.1727
- Menzel, F., Morsbach, S., Martens, J. H., Räder, P., Hadjaje, S., Poizat, M., & Abou, B. (2019). Communication vs. waterproofing: the physics of insect cuticular hydrocarbons. *Journal of Experimental Biology*, 222(Pt 23). doi: 10.1242/jeb.210807
- Meyer, E. F., & Hotz, R. D. (1973). High-Precision Vapor-Pressure Data for Eight Organic Compounds. *Journal of Chemical and Engineering Data*, 18(4), 359–362. doi: 10.1021/JE60059A008/ASSET/JE60059A008.FP.PNG_V03
- Modey, W. K., & Doskey, P. V. (2006). Evaluation of a valveless thermal desorption system for organic aerosols and vapors. *Journal of Chromatography A*, 1121(1), 16–22. doi: 10.1016/j.chroma.2006.04.028
- Moyano, L., Serratos, M. P., Marquez, A., & Zea, L. (2019). Optimization and validation of a DHS-TD-GC-MS method to wineomics studies. *Talanta*, 192, 301–307. doi: 10.1016/j.talanta.2018.09.032
- Münz, J. (2010). *Entwicklung einer Thermodesorptionseinheit für die GC/MS zur Bestimmung hochreaktiver, biogener Kohlenwasserstoffe und deren Anwendung im Rahmen von Labor- und Feldstudien* (Doctoral thesis). Johannes Gutenberg-University, Mainz.
- National Instruments. (n.d.). National Instruments: What Is NI LabVIEW? Retrieved February 14, 2024, from <https://www.ni.com/en/shop/labview.html>
- Nguyen, T. B., Coggon, M. M., Bates, K. H., Zhang, X., Schwantes, R. H., Schilling, K. A., ... Seinfeld, J. H. (2014). Organic aerosol formation from the reactive uptake of isoprene epoxydiols (IEPOX) onto non-acidified inorganic seeds. *Atmospheric Chemistry and Physics*, 14(7), 3497–3510. doi: 10.5194/ACP-14-3497-2014

-
- Pamminger, T., Foitzik, S., Kaufmann, K. C., Schützler, N., & Menzel, F. (2014a). Worker Personality and Its Association with Spatially Structured Division of Labor. *PLoS ONE*, *9*(1), e79616. doi: 10.1371/journal.pone.0079616
- Pamminger, T., Foitzik, S., Kaufmann, K. C., Schützler, N., & Menzel, F. (2014b). Worker Personality and Its Association with Spatially Structured Division of Labor. *PLoS ONE*, *9*(1), e79616. doi: 10.1371/journal.pone.0079616
- Payzant, J. D., Rubinstein, I., Hogg, A. M., & Strausz, O. P. (1980). Analysis of Cold Lake bitumen hydrocarbons by combined GLC-field ionization mass spectrometry and GLC-electron impact mass spectrometry. *Chemical Geology*, *29*(1–4), 73–88. doi: 10.1016/0009-2541(80)90006-6
- Petrosko, S. H., Johnson, R., White, H., & Mirkin, C. A. (2016). Nanoreactors: Small Spaces, Big Implications in Chemistry. *Journal of the American Chemical Society*, *138*(24), 7443–7445. doi: 10.1021/jacs.6b05393
- Petters, M. D., & Kreidenweis, S. M. (2007). A single parameter representation of hygroscopic growth and cloud condensation nucleus activity. *Atmospheric Chemistry and Physics*, *7*(8), 1961–1971. doi: 10.5194/acp-7-1961-2007
- Petters, M., & Kasparoglu, S. (2020). Predicting the influence of particle size on the glass transition temperature and viscosity of secondary organic material. *Scientific Reports*, *10*(1). doi: 10.1038/S41598-020-71490-0
- Petters, Sarah S. (2022). Constraints on the Role of Laplace Pressure in Multiphase Reactions and Viscosity of Organic Aerosols. *Geophysical Research Letters*, *49*(12). doi: 10.1029/2022GL098959
- Petters, Sarah Suda, & Petters, M. D. (2016). Surfactant effect on cloud condensation nuclei for two-component internally mixed aerosols. *Journal of Geophysical Research*, *121*(4), 1878–1895. doi: 10.1002/2015JD024090
- Pöschl, U. (2005). Atmospheric Aerosols: Composition, Transformation, Climate and Health Effects. *Angewandte Chemie International Edition*, *44*(46), 7520–7540. doi: 10.1002/anie.200501122
- Pöschl, U., & Shiraiwa, M. (2015). Multiphase Chemistry at the Atmosphere–Biosphere Interface Influencing Climate and Public Health in the Anthropocene. *Chemical Reviews*, *115*(10), 4440–4475. doi: 10.1021/cr500487s
- Probst, S. (2018). *Entwicklung und Anfertigung einer Steuerungselektronik für ein Thermodesorption-GC-MS-System* (Diploma thesis). Johannes Gutenberg-University, Mainz.

- Pye, H. O. T., Nenes, A., Alexander, B., Ault, A. P., Barth, M. C., Clegg, S. L., ... Zuend, A. (2020, April 24). The acidity of atmospheric particles and clouds. *Atmospheric Chemistry and Physics*, Vol. 20, pp. 4809–4888. Copernicus GmbH. doi: 10.5194/acp-20-4809-2020
- Raepfel, C., Fabritius, M., Nief, M., Appenzeller, B. M. R., Briand, O., Tuduri, L., & Millet, M. (2015). Analysis of airborne pesticides from different chemical classes adsorbed on Radiello® Tenax® passive tubes by thermal-desorption-GC/MS. *Environmental Science and Pollution Research*, 22(4), 2726–2734. doi: 10.1007/s11356-014-3534-z
- Raes, F., Dingenen, R. Van, Vignati, E., Wilson, J., Putaud, J.-P., Seinfeld, J. H., & Adams, P. (2000). Formation and cycling of aerosols in the global troposphere. *Atmospheric Environment*, 34(25), 4215–4240. doi: 10.1016/S1352-2310(00)00239-9
- Riipinen, I., Yli-Juuti, T., Pierce, J. R., Petäjä, T., Worsnop, D. R., Kulmala, M., & Donahue, N. M. (2012). The contribution of organics to atmospheric nanoparticle growth. *Nature Geoscience*, 5(7), 453–458. doi: 10.1038/ngeo1499
- Rissman, T. A., Varutbangkul, V., Surratt, J. D., Topping, D. O., McFiggans, G., Flagan, R. C., & Seinfeld, J. H. (2007). Cloud condensation nucleus (CCN) behavior of organic aerosol particles generated by atomization of water and methanol solutions. *Atmospheric Chemistry and Physics*, 7(11), 2949–2971. doi: 10.5194/acp-7-2949-2007
- Riva, M., Sun, J., McNeill, V. F., Ragon, C., Perrier, S., Rudich, Y., ... George, C. (2021). High Pressure Inside Nanometer-Sized Particles Influences the Rate and Products of Chemical Reactions. *Environmental Science & Technology*, 55(12), 7786–7793. doi: 10.1021/acs.est.0c07386
- Roghani, M., Jacobs, O. P., Miller, A., Willett, E. J., Jacobs, J. A., Viteri, C. R., ... Pennell, K. G. (2018). Occurrence of chlorinated volatile organic compounds (VOCs) in a sanitary sewer system: Implications for assessing vapor intrusion alternative pathways. *Science of the Total Environment*, 616–617, 1149–1162. doi: 10.1016/j.scitotenv.2017.10.205
- Rourke, B. C., & Gibbs, A. G. (1999). Effects of lipid phase transitions on cuticular permeability: model membrane and *in situ* studies. *Journal of Experimental Biology*, 202(22), 3255–3262. doi: 10.1242/jeb.202.22.3255
- Rubinstein, I., & Strausz, O. P. (1979). Thermal treatment of the Athabasca oil sand bitumen and its component parts. *Geochimica et Cosmochimica Acta*, 43(12), 1887–1893. doi: 10.1016/0016-7037(79)90002-4

-
- Russo, M. V., Avino, P., Perugini, L., & Notardonato, I. (2015). Extraction and GC-MS analysis of phthalate esters in food matrices: a review. *RSC Advances*, 5(46), 37023–37043. doi: 10.1039/C5RA01916H
- Ruther, J., Sieben, S., & Schricker, B. (2002). Nestmate recognition in social wasps: manipulation of hydrocarbon profiles induces aggression in the European hornet. *Naturwissenschaften*, 89(3), 111–114. doi: 10.1007/s00114-001-0292-9
- Sakai, T., Morita, Y., Roh, J., Kim, H., & Kim, Y. (2005). Improvement in the GC-MS method for determining urinary toluene-diamine and its application to the biological monitoring of workers exposed to toluene-diisocyanate. *International Archives of Occupational and Environmental Health*, 78(6), 459–466. doi: 10.1007/s00420-004-0571-9
- Sales, C., Portolés, T., Johnsen, L. G., Danielsen, M., & Beltran, J. (2019). Olive oil quality classification and measurement of its organoleptic attributes by untargeted GC-MS and multivariate statistical-based approach. *Food Chemistry*, 271, 488–496. doi: 10.1016/j.foodchem.2018.07.200
- Sanderson, B. M. (2023). Estimating vanishing allowable emissions for 1.5 °C. *Nature Climate Change*, 13(12), 1284–1285. doi: 10.1038/s41558-023-01846-7
- Schmidt, D. (2021). *Konzeption einer Regelungssoftware für ein Thermodesorptions-GC-MS-System* (Bachelor thesis). Johannes Gutenberg University, Mainz.
- Schultheiss, P., Nooten, S. S., Wang, R., Wong, M. K. L., Brassard, F., & Gu Enard, B. (2022). *The abundance, biomass, and distribution of ants on Earth*. doi: 10.1073/pnas
- Schurman, M. I., Kim, J. Y., Cheung, H. H. Y., & Chan, C. K. (2017). Atmospheric particle composition-hygroscopic growth measurements using an in-series hybrid tandem differential mobility analyzer and aerosol mass spectrometer. *Aerosol Science and Technology*, 51(6), 694–703. doi: 10.1080/02786826.2017.1309350
- Scigelova, M., & Makarov, A. (2006). Orbitrap mass analyzer - Overview and applications in proteomics. *Proteomics*, 1(1-2 SUPPL.), 16–21. doi: 10.1002/PMIC.200600528
- Seguchi, K., Sera, A., Otsuki, Y., & Maruyama, K. (1975). An Investigation of the endo Product Selectivity in the Diels-Alder Reaction. *Bulletin of the Chemical Society of Japan*, 48(12), 3641–3644. doi: 10.1246/bcsj.48.3641
- Seinfeld, J. H., & Pandis, S. N. (2006). *Atmospheric Chemistry and Physics: From Air Pollution to Climate Change*. (2nd ed.). John Wiley & Sons, inc.
- Seinfeld, J. H., & Pandis, S. N. (2016). *Atmospheric Chemistry and Physics: From Air Pollution to Climate Change* (3rd ed.). John Wiley and Sons.

- Sellegrì, K., & Boulon, J. (2017). Aerosol Nucleation in the Terrestrial Atmosphere. In *Atmospheric Aerosols* (pp. 87–114). Wiley. doi: 10.1002/9783527336449.ch2
- Shiraiwa, M., Zuend, A., Bertram, A. K., & Seinfeld, J. H. (2013). Gas–particle partitioning of atmospheric aerosols: interplay of physical state, non-ideal mixing and morphology. *Physical Chemistry Chemical Physics*, *15*(27), 11441–11453. doi: 10.1039/C3CP51595H
- Śmiełowska, M., Ligor, T., Kupczyk, W., Szeliga, J., Jackowski, M., & Buszewski, B. (2023). Screening for volatile biomarkers of colorectal cancer by analyzing breath and fecal samples using thermal desorption combined with GC-MS (TD-GC-MS). *Journal of Breath Research*, *17*(4), 047102. doi: 10.1088/1752-7163/ace46e
- Smith, J. N., Dunn, M. J., VanReken, T. M., Iida, K., Stolzenburg, M. R., McMurry, P. H., & Huey, L. G. (2008). Chemical composition of atmospheric nanoparticles formed from nucleation in Tecamac, Mexico: Evidence for an important role for organic species in nanoparticle growth. *Geophysical Research Letters*, *35*(4), L04808. doi: 10.1029/2007GL032523
- Smith, James N., Barsanti, K. C., Friedli, H. R., Ehn, M., Kulmala, M., Collins, D. R., ... McMurry, P. H. (2010). Observations of ammonium salts in atmospheric nanoparticles and possible climatic implications. *Proceedings of the National Academy of Sciences*, *107*(15), 6634–6639. doi: 10.1073/pnas.0912127107
- Smith, M. E., Westbrook, E., Stastny, A. L., Streicher, R. P., & Elliott, M. G. (2022). Method development for on-site monitoring of volatile organic compounds via portable TD-GC-MS: evaluation of the analytical performances of HAPSITE® ER instrumentation and thermal desorption sampling media. *International Journal of Environmental Analytical Chemistry*, 1–18. doi: 10.1080/03067319.2022.2121163
- Song, H., & Liu, J. (2018, December 1). GC-O-MS technique and its applications in food flavor analysis. *Food Research International*, Vol. 114, pp. 187–198. Elsevier Ltd. doi: 10.1016/j.foodres.2018.07.037
- Sorensen, C. M., Gebhart, J., O’Hern, T. J., & Rader, D. J. (2011). Optical Measurement Techniques: Fundamentals and Applications. In *Aerosol Measurement* (3. ed., pp. 269–312). Wiley. doi: 10.1002/9781118001684.ch13
- Soroker, V., Hefetz, A., Cojocar, M., Billen, J., Franken, S., & Francke, W. (1995). Structural and chemical ontogeny of the postpharyngeal gland in the desert ant *Cataglyphis niger*. *Physiological Entomology*, *20*(4), 323–329. doi: 10.1111/j.1365-3032.1995.tb00822.x

-
- Soroker, V., Vienne, C., Hefetz, A., & Nowbahari, E. (1994). The postpharyngeal gland as a “Gestalt” organ for nestmate recognition in the ant *Cataglyphis niger*. *Naturwissenschaften*, *81*(11), 510–513. doi: 10.1007/BF01132686
- Soroker, Victoria, Vienne, C., & Hefetz, A. (1995). Hydrocarbon dynamics within and between nestmates in *Cataglyphis niger* (Hymenoptera: Formicidae). *Journal of Chemical Ecology*, *21*(3), 365–378. doi: 10.1007/BF02036724
- Spielvogel, J. (2009, September 2). *Informative Overview about Nano Instrumentation from GRIMM*. Zürich: Grimm. Retrieved from https://www.analyticjournal.de/fachreports/grimm_nano_tubln_07_09/grimm_nano_spielvogel.pdf
- Spracklen, D. V., Carslaw, K. S., Kulmala, M., Kerminen, V.-M., Mann, G. W., & Sihto, S.-L. (2006). The contribution of boundary layer nucleation events to total particle concentrations on regional and global scales. *Atmospheric Chemistry and Physics*, *6*(12), 5631–5648. doi: 10.5194/acp-6-5631-2006
- Su, H., Cheng, Y., & Pöschl, U. (2020). New Multiphase Chemical Processes Influencing Atmospheric Aerosols, Air Quality, and Climate in the Anthropocene. *Accounts of Chemical Research*, *53*(10), 2034–2043. doi: 10.1021/acs.accounts.0c00246
- Swiss, K. A., & Firestone, R. A. (2000). Phantom Activation Volumes. *The Journal of Physical Chemistry A*, *104*(13), 3057–3063. doi: 10.1021/jp9935900
- Tang, S.-Y., Shi, J., & Guo, Q.-X. (2012). Accurate prediction of rate constants of Diels–Alder reactions and application to design of Diels–Alder ligation. *Organic & Biomolecular Chemistry*, *10*(13), 2673. doi: 10.1039/c2ob07079k
- Tomasi, C., Fuzzi, S., & Kokhanovsky, A. (2017). *Atmospheric Aerosols* (C. Tomasi, S. Fuzzi, & A. Kokhanovsky, Eds.). Wiley. doi: 10.1002/9783527336449
- Topping, D. O., McFiggans, G. B., Kiss, G., Varga, Z., Facchini, M. C., Decesari, S., & Mircea, M. (2007). Surface tensions of multi-component mixed inorganic/organic aqueous systems of atmospheric significance: measurements, model predictions and importance for cloud activation predictions. *Atmospheric Chemistry and Physics*, *7*(9), 2371–2398. doi: 10.5194/acp-7-2371-2007
- Traniello, J. F. A. (1989). Chemical Trail Systems, Orientation, and Territorial Interactions in the Ant *Lasius neoniger*. In *Journal of Insect Behavior* (Vol. 2).
- Traniello, J. F. A., & Hölldobler, B. (1984). Chemical communication during tandem running in *Pachycondyla obscuricornis* (Hymenoptera: Formicidae). *Journal of Chemical Ecology*, *10*(5), 783–794. doi: 10.1007/BF00988543

- TSI Incorporated. (2016). *Electrostatic Classifier Model 3082 Scanning Mobility Particle Sizer™ (SMPS™) Spectrometer Model 3938 Operation and Service Manual P/N 6006760, Revision C*.
- TSI Incorporated. (2019). *Water-Based Condensation Particle Counter Model 3789: Operational Manual*.
- Tu, C., Yin, Z., Lin, J., & Bao, F. (2017). A Review of Experimental Techniques for Measuring Micro- to Nano-Particle-Laden Gas Flows. *Applied Sciences*, 7(2), 120. doi: 10.3390/app7020120
- Vallecillos, L., Borrull, F., & Pocurull, E. (2015). Recent approaches for the determination of synthetic musk fragrances in environmental samples. *TrAC Trends in Analytical Chemistry*, 72, 80–92. doi: 10.1016/j.trac.2015.03.022
- van der Valk, J. P. M., & in 't Veen, J. C. C. M. (2021). SARS-Cov-2: The Relevance and Prevention of Aerosol Transmission. *Journal of Occupational & Environmental Medicine*, 63(6), e395–e401. doi: 10.1097/JOM.0000000000002193
- van Drooge, B. L., Nikolova, I., & Ballesta, P. P. (2009). Thermal desorption gas chromatography-mass spectrometry as an enhanced method for the quantification of polycyclic aromatic hydrocarbons from ambient air particulate matter. *Journal of Chromatography A*, 1216(18), 4030–4039. doi: 10.1016/j.chroma.2009.02.043
- Van Eldik, R., Asano, T., & Le Noble, W. J. (1989). Activation and reaction volumes in solution. 2. *Chemical Reviews*, 89(3), 549–688. doi: 10.1021/cr00093a005
- van Zweden, J. S., Dreier, S., & d’Ettorre, P. (2009). Disentangling environmental and heritable nestmate recognition cues in a carpenter ant. *Journal of Insect Physiology*, 55(2), 159–164. doi: 10.1016/j.jinsphys.2008.11.001
- Vehkamäki, H., & Riipinen, I. (2012). Thermodynamics and kinetics of atmospheric aerosol particle formation and growth. *Chemical Society Reviews*, 41(15), 5160–5173. doi: 10.1039/c2cs00002d
- Ventura, G. T., Kenig, F., Reddy, C. M., Frysinger, G. S., Nelson, R. K., Mooy, B. Van, & Gaines, R. B. (2008). Analysis of unresolved complex mixtures of hydrocarbons extracted from Late Archean sediments by comprehensive two-dimensional gas chromatography (GC×GC). *Organic Geochemistry*, 39(7), 846–867. doi: 10.1016/j.orggeochem.2008.03.006
- Vera, T., Villanueva, F., Wimmerová, L., & Tolis, E. I. (2022a). An overview of methodologies for the determination of volatile organic compounds in indoor air. *Applied Spectroscopy Reviews*, 57(8), 625–674. doi: 10.1080/05704928.2022.2085735

-
- Vera, T., Villanueva, F., Wimmerová, L., & Tolis, E. I. (2022b). An overview of methodologies for the determination of volatile organic compounds in indoor air. *Applied Spectroscopy Reviews*, Vol. 57, pp. 625–674. Taylor and Francis Ltd. doi: 10.1080/05704928.2022.2085735
- von Frisch. (1967). *The Dance Language and Orientation of Bees*. Cambridge: Harvard University Press.
- Wang, L., Khalizov, A. F., Zheng, J., Xu, W., Ma, Y., Lal, V., & Zhang, R. (2010). Atmospheric nanoparticles formed from heterogeneous reactions of organics. *Nature Geoscience*, 3(4), 238–242. doi: 10.1038/ngeo778
- Westphal, K., Dudzik, D., Waszczuk-Jankowska, M., Graff, B., Narkiewicz, K., & Markuszewski, M. J. (2022). Common Strategies and Factors Affecting Off-Line Breath Sampling and Volatile Organic Compounds Analysis Using Thermal Desorption-Gas Chromatography-Mass Spectrometry (TD-GC-MS). *Metabolites*, 13(1), 8. doi: 10.3390/metabo13010008
- Wiedensohler, A. (1988). An approximation of the bipolar charge distribution for particles in the submicron size range. *Journal of Aerosol Science*, 19(3), 387–389. doi: 10.1016/0021-8502(88)90278-9
- Winklmayr, W., Reischl, G. P., Lindner, A. O., & Berner, A. (1991). A new electromobility spectrometer for the measurement of aerosol size distributions in the size range from 1 to 1000 nm. *Journal of Aerosol Science*, 22(3), 289–296. doi: 10.1016/S0021-8502(05)80007-2
- Wittke, M., Baumgart, L., & Menzel, F. (2022). Acclimation in ants: Interference of communication and waterproofing through cuticular hydrocarbons in a multifunctional trait. *Functional Ecology*, 36(8), 1973–1985. doi: 10.1111/1365-2435.14104
- Woolfenden, E. (2010a). Sorbent-based sampling methods for volatile and semi-volatile organic compounds in air: Part 1: Sorbent-based air monitoring options. *Journal of Chromatography A*, 1217(16), 2674–2684. doi: 10.1016/J.CHROMA.2009.12.042
- Woolfenden, E. (2010b). Sorbent-based sampling methods for volatile and semi-volatile organic compounds in air. Part 2. Sorbent selection and other aspects of optimizing air monitoring methods. *Journal of Chromatography A*, 1217(16), 2685–2694. doi: 10.1016/J.CHROMA.2010.01.015
- World Health Org. (2006). *Health risks of particulate matter from long-range transboundary air pollution*. Retrieved from <http://www.euro.who.int/pubrequest>.

- Wu, C.-H., Feng, C.-T., Lo, Y.-S., Lin, T.-Y., & Lo, J.-G. (2004). Determination of volatile organic compounds in workplace air by multisorbent adsorption/thermal desorption-GC/MS. *Chemosphere*, 56(1), 71–80. doi: 10.1016/j.chemosphere.2004.02.003
- Wyatt, T. D. (2014). Pheromones and Animal Behavior. In *Pheromones and Animal Behaviour*. Cambridge University Press. doi: 10.1017/CBO9780511615061.002
- Xu, M. L., Gao, Y., Wang, X., Han, X. X., & Zhao, B. (2021, October 1). Comprehensive strategy for sample preparation for the analysis of food contaminants and residues by gc–ms/ms: A review of recent research trends. *Foods*, Vol. 10. MDPI. doi: 10.3390/foods10102473
- Yadav, S., Tandon, A., & Attri, A. K. (2013). Characterization of aerosol associated non-polar organic compounds using TD-GC-MS: A four year study from Delhi, India. *Journal of Hazardous Materials*, 252–253, 29–44. doi: 10.1016/j.jhazmat.2013.02.024
- Young, T., Peacock, G., & Leitch, J. (1855). *Miscellaneous Works of the Late Thomas Young* (Vol 1). J. Murray.
- Yu, F., Luo, G., Bates, T. S., Anderson, B., Clarke, A., Kapustin, V., ... Wu, S. (2010). Spatial distributions of particle number concentrations in the global troposphere: Simulations, observations, and implications for nucleation mechanisms. *Journal of Geophysical Research: Atmospheres*, 115(D17). doi: 10.1029/2009JD013473
- Zhang, K. M., & Wexler, A. S. (2002). A hypothesis for growth of fresh atmospheric nuclei. *Journal of Geophysical Research: Atmospheres*, 107(D21). doi: 10.1029/2002JD002180

14 List of related publications and presentations

14.1 Oral presentations

01/2023

D. Kleinsimlinghaus, L. Brill, A. Stenglein, F. Menzel, T. Hoffmann: Development of a versatile thermal desorption system to improve the identification and quantification of very low to high volatility organic analytes by GC-Orbitrap-MS *33rd doctoral seminar of the GDCh AK Separation Science*, Hohenroda, Germany.

05/2022

D. Kleinsimlinghaus, T. Hoffmann: Diels-Alder-Reactions in nanometer aerosol particles *EGU General Assembly 2022*, Vienna, Austria. <https://doi.org/10.5194/egusphere-egu22-7474>

14.2 Poster presentations

09/2023 – *Best Poster Award*

D. Kleinsimlinghaus, T. Hoffmann: Pressure-induced Diels-Alder-Reactions in nanometer aerosol particles: Experimental method and instrument development *European Aerosol Conference 2023*, Malaga, Spain.

09/2022

D. Kleinsimlinghaus, T. Hoffmann: Chemistry in nanometer aerosol particles: Flow tube experiments with pressure-dependent Diels-Alder reactions. *International Aerosol Conference 2022*, Athens, Greece.

Curriculum Vitae

Personal Information

Name: Daniela Kleinsimlinghaus

Date of birth: 03.01.1993

Place of birth: Mainz

Citizenship: German

Education

11/2019 – 05/2024 Doctorate (Dr. rer. nat.) in Chemistry
Department of Chemistry
Johannes Gutenberg University Mainz, Germany
1st Supervisor: Prof. Dr. Thorsten Hoffmann,
2nd Supervisor Prof. Dr. Nicolas H. Bings

09/2016 – 11/2019 Master thesis
Department of Chemistry
Johannes Gutenberg University Mainz, Germany

10/2012 – 09/2016 Bachelor thesis
Department of Chemistry
Johannes Gutenberg University Mainz, Germany
Workgroup of Prof. Dr. Thorsten Hoffmann

08/2003 – 06/2012 Abitur
Immanuel-Kant-Gymnasium
Rüsselsheim, Germany

Mainz, March, 2024